Reviews of Geophysics

REVIEW ARTICLE
10.1029/2020RG000714

Key Points:

- *Wind* has made seminal advances to the fields of astrophysics, turbulence, kinetic physics, magnetic reconnection, and the radiation belts
- *Wind* pioneered the study of the source and evolution of solar radio emissions below 15 MHz
- *Wind* revolutionized our understanding of coronal mass ejections, their internal magnetic structure, and evolution

Correspondence to:
L. B. Wilson III,
lynn.b.wilsoniii@gmail.com

Citation:
Wilson, L. B., Brosius, A. L., Gopalswamy, N., Nieves-Chinchilla, T., Szabo, A., Hurley, K., et al. (2021). A quarter century of *wind* spacecraft discoveries. *Reviews of Geophysics*, *59*, e2020RG000714. https://doi.org/10.1029/2020RG000714

Received 14 SEP 2020
Accepted 5 MAR 2021

A Quarter Century of *Wind* Spacecraft Discoveries

Lynn B. Wilson III[1], Alexandra L. Brosius[1,2], Natchimuthuk Gopalswamy[1], Teresa Nieves-Chinchilla[1], Adam Szabo[1], Kevin Hurley[3], Tai Phan[3], Justin C. Kasper[4], Noé Lugaz[5,6], Ian G. Richardson[1,7], Christopher H. K. Chen[8], Daniel Verscharen[5,9], Robert T. Wicks[10], and Jason M. TenBarge[11,12]

[1]NASA Goddard Space Flight Center, Heliophysics Science Division, Greenbelt, MD, USA, [2]Department of Meteorology and Atmospheric Science, The Pennsylvania State University, University Park, PA, USA, [3]Space Sciences Laboratory, University of California, Berkeley, CA, USA, [4]School of Climate and Space Sciences and Engineering, University of Michigan, Ann Arbor, Ann Arbor, MI, USA, [5]Space Science Center, Institute for the Study of Earth, Oceans, and Space, University of New Hampshire, Durham, NH, USA, [6]Department of Physics, University of New Hampshire, Durham, NH, USA, [7]Department of Astronomy, University of Maryland, College Park, MD, USA, [8]School of Physics and Astronomy, Queen Mary University of London, London, UK, [9]Mullard Space Science Laboratory, University College London, Surrey, UK, [10]Department of Mathematics, Physics and Electrical Engineering, Northumbria University: Newcastle upon Tyne, Tyne and Wear, UK, [11]University of Maryland, College Park, MD, USA, [12]Department of Astrophysical Sciences, Princeton University, Princeton, NJ, USA

Abstract The *Wind* spacecraft, launched on November 1, 1994, is a critical element in NASA's Heliophysics System Observatory (HSO)—a fleet of spacecraft created to understand the dynamics of the Sun-Earth system. The combination of its longevity (>25 years in service), its diverse complement of instrumentation, and high resolution and accurate measurements has led to it becoming the "standard candle" of solar wind measurements. *Wind* has over 55 selectable public data products with over ~1,100 total data variables (including OMNI data products) on SPDF/CDAWeb alone. These data have led to paradigm shifting results in studies of statistical solar wind trends, magnetic reconnection, large-scale solar wind structures, kinetic physics, electromagnetic turbulence, the Van Allen radiation belts, coronal mass ejection topology, interplanetary and interstellar dust, the lunar wake, solar radio bursts, solar energetic particles, and extreme astrophysical phenomena such as gamma-ray bursts. This review introduces the mission and instrument suites then discusses examples of the contributions by *Wind* to these scientific topics that emphasize its importance to both the fields of heliophysics and astrophysics.

Plain Language Summary The *Wind* spacecraft is a south ecliptic pointed spinning spacecraft that was launched on November 1, 1994. It is equipped with an array of instrument suites that measure electric and magnetic fields, electrons from thermal to relativistic energies, protons and alpha-particles from thermal to suprathermal energies, and energetic ions from hydrogen to trans-iron elements. *Wind* can also observe remote sources of electromagnetic radiation in the radio and gamma-ray frequency ranges. This diverse array of instrumentation and numerous near-Earth environments explored has allowed researchers to examine such a broad range of research topics including astrophysics, turbulence, kinetic physics, magnetic reconnection, interplanetary and interstellar dust, transient solar phenomena, and the radiation belts. Examples of the contributions of *Wind* to the fields of heliophysics and astrophysics are reviewed.

1. The *Wind* Mission

NASA launched the *Wind* spacecraft on November 1, 1994. *Wind* and *Polar* (Harten & Clark, 1995) were part of the stand-alone Global Geospace Science (GGS) Program (Acuña et al., 1995), a subset of the International Solar Terrestrial Physics (ISTP) Program (Whipple & Lancaster, 1995). The ISTP Program included the additional missions *Geotail* (Nishida, 1994), the SOlar and Heliospheric Observatory or *SoHO* (Domingo et al., 1995), and *Cluster* (Escoubet et al., 1997). The objective of the ISTP program was to study the origin of solar variability and activity, the transport of manifestations of that activity to the Earth via plasma processes, and the cause-and-effect relationships between that time varying energy transport and the near-earth environment.

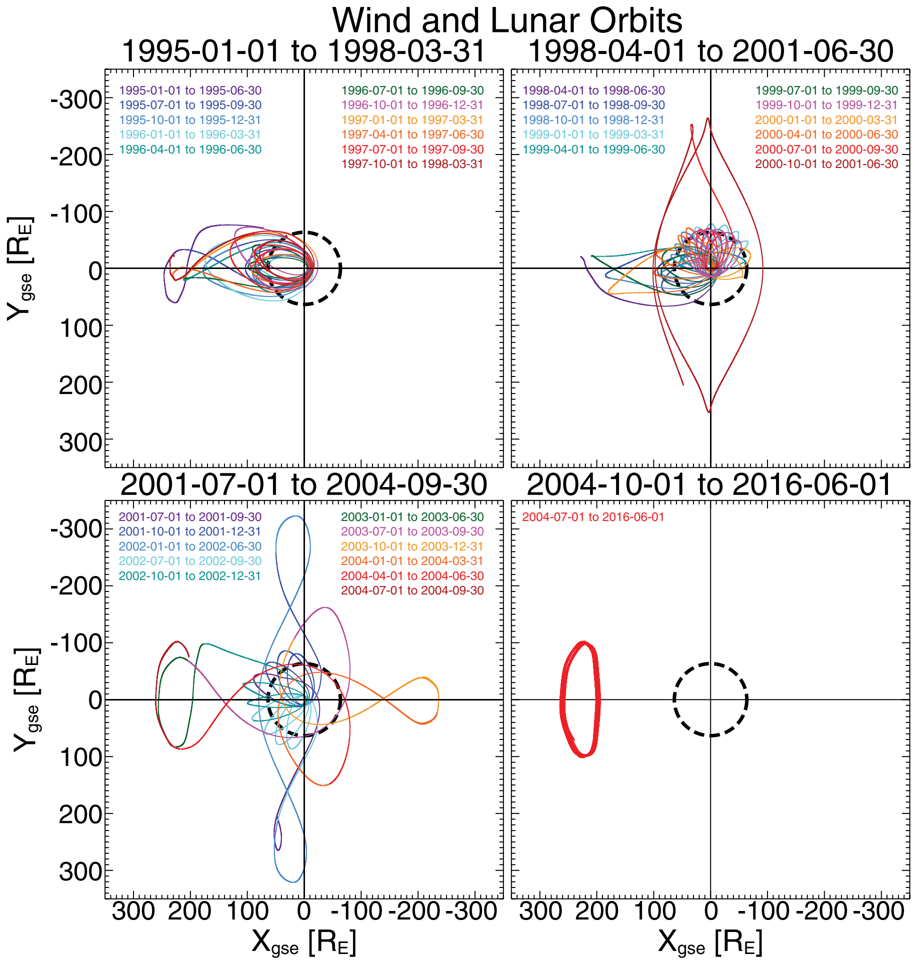

Figure 1. Orbital trajectories of the *Wind* spacecraft in the GSE XY plane from November 1, 1994 to June 1, 2016. Colors denote time ranges as indicated. The dashed black circle indicates the Moon's orbit (Adapted from Figure 1 in Malaspina & Wilson, 2016). Note that the orbit has not noticeably changed since June 1, 2016.

Wind is a spin stabilized spacecraft—spin axis aligned with ecliptic south—with a spin period of ~3 s. Prior to May 2004, *Wind* performed a series of orbital maneuvers (H. Franz et al., 1998), as shown in Figure 1, that led to the spacecraft visiting numerous regions of the near-Earth enviroment. For instance, between launch and late 2002 *Wind* completed ~67 petal orbits through the magnetosphere and two lunar rolls out of the ecliptic in April and May of 1999. Between August 2000 and June 2002 *Wind* completed four east-west prograde 1:3–Lissajous orbits reaching $\gtrsim$300 R_E along the ±Y-GSE direction (Fränz & Harper, 2002). From November 2003 to February 2004 *Wind* performed an excursion to the second Earth-Sun libration point, or Lagrange point, called L2. Note that L2 is located ~233–235 R_E downstream of Earth and ~500 R_E downstream of the Advanced Composition Explorer (ACE) (Stone et al., 1998). For reference, ACE launched in 1997 and was designed to study energetic particles and their composition. Unlike *Wind*, ACE was not designed to study kinetic physics or remote solar and astrophysical phenomena using electric fields.

In May 2004, *Wind* made its final major orbital maneuver using a lunar gravitational assist to insert it into a Lissajous orbit about the first Earth-Sun libration point, labeled L1 by late June 2004. Note that *Wind*'s L1 orbit has a ±Y-GSE(±X-GSE) displacement about the sun-Earth line of ~100 R_E(~35 R_E), much larger than the other NASA mission at L1, ACE. The ±Z-GSE displacement from the ecliptic plane is $\lesssim$ 30 R_E for both ACE and *Wind* (For more details, see the *Wind* Senior Review reports provided at: https://wind.nasa.gov.). On June 26, 2020, the *Wind* flight operations team (FOT) successfully completed the first halo orbit insertion maneuver and the second was successfully completed on August 31, 2020. The third maneuver was successfully completed on November 9, 2020. This orbital change was necessary to prevent the spacecraft trajectory from entering the solar exclusion zone—area around the solar disk where solar radio emissions cause sufficient interference with spacecraft communications to prevent telemetry signal locks. The projection of the orbit in the ecliptic plane will not noticeably change, however, the out-of-ecliptic projection will now be a stationary ellipse centered on the solar disk. The difference between a halo and Lissajous orbit in this context is the out of ecliptic position, or z-component. In the latter, the z-component oscillation/orbital period is decoupled from the in-plane components. The halo orbit forces all three components to couple so the orbit becomes an ellipse tilted relative to the ecliptic plane.

The mission has amassed >5810 refereed publications using *Wind* data between launch and December 31, 2020 with a NASA ADS h-index of 148, an i10-index of 3,198, >156,880 citations, and >1,046,210 reads as of March 19, 2021. Despite being 25+ years old, the *Wind* mission still remains active and *Wind* data continue to be relevant as evidenced by the >1,490 refereed publications between January 1, 2017 and December 31, 2020. Furthermore, *Wind* data access requests were >10,291,900 between January 1, 2017 and December 31, 2019 on NASA's SPDF/CDAWeb or ~9,400 per day. The only NASA run heliophysics mission currently operating that is older is the *Voyager* mission at >43 years, but both spacecraft have significantly reduced capabilities from their original design. Some other missions have been operating >19 years and are still active but operating at limited/reduced capacity. *Wind* is still fully functional and yielding new data products due to hardware redundancy and large fuel supplies. Thus, *Wind* is one of the longest running and most productive missions in the Heliophysics System Observatory (HSO).

The article is organized as follows:

- Section 2 reviews the instrument suites, their capabilities, current status, and provides some long-term statistics as an illustration of *Wind*'s capabilities;
- Section 3 provides background information and context for the following subsections that review *Wind*'s scientific advances;
  - — Section 3.1 reviews *Wind*'s contribution to gamma ray and solar x-ray astronomy;
  - — Section 3.2 reviews *Wind*'s contribution to interstellar and interplanetary dust;
  - — Section 3.3 reviews *Wind*'s contribution to our understanding of the lunar wake;
  - — Section 3.4 reviews *Wind*'s contribution to magnetic reconnection in Earth's magnetotail;
  - — Section 3.5 reviews *Wind*'s contribution to our understanding of the Earth's radiation belts;
  - — Section 3.6 reviews *Wind*'s contribution to our understanding of the terrestrial foreshock;
  - — Section 3.7 includes multiple subsections focused on work in the solar wind;
    - * Section 3.7.1 reviews *Wind*'s contribution to our understanding of large scale structures and magnetic reconnection in the solar wind;
    - * Section 3.7.2 reviews *Wind*'s contribution to our understanding of kinetic instabilities and waves in the solar wind;
    - * Section 3.7.3 reviews *Wind*'s contribution to our understanding of turbulence in the solar wind; and
    - * Section 3.7.4 reviews some long-term statistical studies performed by *Wind* in the solar wind;
  - — Section 3.8 includes multiple subsections focused on transient, large-scale, magnetic phenomena;
    - * Section 3.8.1 reviews *Wind*'s contribution to our understanding of interplanetary shocks;
    - * Section 3.8.2 reviews *Wind*'s contribution to our understanding of interplanetary coronal mass ejections; and
    - * Section 3.8.3 reviews *Wind*'s contribution to our understanding of stream interaction regions and corotating interaction regions;
  - — Section 3.9 reviews *Wind*'s contribution to our understanding of solar energetic particles;
  - — Section 3.10 starts by introducing solar radio bursts and how *Wind* has made major advances then goes into several subsections including;
    - * Section 3.10.1 reviews *Wind*'s contribution to our understanding of type II radio bursts;
    - * Section 3.10.2 reviews *Wind*'s contribution to our understanding of type III radio bursts;
    - * Section 3.10.3 reviews *Wind*'s contribution to our understanding of type III storms; and
    - * Section 3.10.4 reviews *Wind*'s contribution to our understanding of type VI radio bursts;
  - — Section 3.11 discusses *Wind*'s relationship to the HSO with a focus on *Parker Solar Probe* and *Solar Orbiter*;

Table 1
Wind Instrument Names

Abbreviations	Instrument name	Reference
TGRS	Transient Gamma-Ray Spectrometer	A. Owens et al. (1995)
KONUS	Gamma-Ray Spectrometer	Aptekar et al. (1995)
EPACT	Energetic Particles: Acceleration, Composition, and Transport	von Rosenvinge et al. (1995)
SMS	Solar Wind and Suprathermal Ion Composition Experiment	Gloeckler et al. (1995)
MFI	Magnetic Field Investigation	Lepping et al. (1995)
WAVES	The Radio and Plasma Wave Investigation	Bougeret et al. (1995)
3DP	Three-Dimensional Plasma and Energetic Particle Investigation	Lin et al. (1995)
SWE	Solar Wind Experiment	Ogilvie et al. (1995)

- Section 4 provides a summary and review of the highlights contained within this review article.
- Appendix A provides definitions of symbols/parameters used in the text;
- Appendix B provides a review of several plasma instabilities and their properties, all of which *Wind* data has been used to investigate;
- Appendix C lists some of the databases relying upon or created by *Wind* data; and
- Finally we provide Appendix C for the reader to help with the jargon and acronyms/initialisms used herein.

2. *Wind* Instrument Suites and Long-Term Statistics

The *Wind* instruments can be divided into two categories: field and particle suites. The field instruments measure γ-rays, radio waves, electric fields, and magnetic fields. The particle instruments measure thermal protons, alpha-particles, and electrons in addition to suprathermal and heavy ions (e.g., carbon-nitrogen-oxygen, iron, trans-iron). All of the thermal particle instruments (and some of the suprathermal) measure particles as functions of energy and solid angle which allows researchers to construct velocity distribution functions (VDFs)—particle probability density functions in velocity space. The full 3D VDF measurements also allow researchers to calculate velocity moments of the distribution such as number density, bulk flow velocity, thermal pressure/temperature, and heat flux. The *Wind* instrument names and acronyms are listed below in Table 1.

It is important to note that unlike most other missions, *Wind* was designed with significant redundancy in its measurements. For instance, there are at least five possible measurements of the solar wind number density (two from 3DP, two from SWE, one from WAVES, and one from SMS under certain conditions) and prior to 2000 there were two different gamma ray instruments. The MFI comprises of two fluxgate magnetometers at different locations on a 12 m boom (one closer at ~8 m, the other at 12 m) which improves spacecraft noise/artifact removal. There are three separate measurements of protons with energies >50 keV (one from 3DP, one from SMS, and one from EPACT). Finally, there are at least three separate measurements of heavy ions (i.e., ions more massive than alpha-particles). The instrument capabilities and current status are shown in Table 3 (see the Glossary and Acronyms Appendices for definitions).

Most of the instruments continue to be fully functional, aside from temporary data losses due to a command and attitude processor (CAP) and tape unit anomaly (both issues were resolved or mitigated). The dates of significant spacecraft and instrumental issues are listed in Table 2 for reference.

In this review, we present *Wind* results for a variety of environments in an effort to highlight a reasonable fraction of *Wind*'s publications. For a broad overview of *Wind* particles and field observations, Figure 2 shows 25+ years of observations from MFI and SWE instruments across more than two solar cycles (late cycle 22–cycle 24) indicated by the background color. The temporal resolutions for MFI and SWE are ~1 min (averages) and ~92 s, respectively. A 2D histogram was constructed from one week bins on the horizontal axis while the vertical axis is split up into 300 bins for each panel. The data were artificially clipped when creating the 2D histogram to reduce low statistics bins. The range of values used to construct the histograms

Table 2
Wind Instrument and Spacecraft Anomalies

Date	Part affected	Impact
January 19, 1995	GTM1[a]	Failure
October 1995	APE-A/APE-B/IT HVPS[b]	Suffered a loss of gain
April 30, 1997	CAP1[c]	Reed-Solomon encoder failure
December 13, 1997	DTR2[d]	Power supply failure
January 2000	TGRS	γ-ray instrument turned off (planned coolant outage)
May 2000	SMS-SWICS	Solar wind composition sensor turned off
June 2001	SWE-VEIS	Thermal electron detectors HVPS failure
August 2002	SWE-Strahl	Reconfigured to recover VEIS functionality
June 2009	SMS DPU	Experienced a latch-up reset—MASS acceleration/ deceleration power supply in fixed voltage mode
2010	SMS-MASS	Experienced a small degradation in the acceleration/ deceleration power supply
May 19, 2014	3DP-PESA Low	Suffered an anomaly that affected only the telemetry HK[e] data
October 27, 2014	CAP1	Anomaly at ~21:59:38 GMT
November 7, 2014	CAP2	Set to primary while recovery starts on CAP1
November 26, 2014	SWE	Full reset due to CAP1 anomaly
January 30, 2015	CAP1	Fully recovered
April 11, 2016	DTR1 TUA	Began experiencing read/write errors (~1% bit errors)
May 6, 2016	DTR1 TUB	FOT sets as primary recorder

[a] Two GGS telemetry modules, GTM1 and GTM2. [b] High voltage power supply. [c] Two command and attitude processors, CAP1 and CAP2. [d] Two digital tape recorders, DTR1 and DTR2, each with independent tape units, TUA and TUB. [e] House keeping.

are $0 \leq B_o \leq 300\ nT$, $0 \leq n_i \leq 300\ \mathrm{cm}^{-3}$, and $200 \leq V_i \leq 1{,}400\ \mathrm{km\ s}^{-1}$. The range of values shown on the vertical axis are further restricted to focus on the values most commonly observed over the total interval. The color bars show the number of counts in each bin where white space represents no counts and red (represents) saturation. These calculations include solar wind and magnetospheric intervals. The fluxgate magnetometer had few data gaps during magnetospheric passes. The SWE Faraday cups could not track the bulk ion population within the magnetosphere and exhibit sparser coverage than MFI prior to May 2004. Table 4 provides some one-variable statistics of the data shown in Figure 2 for reference.

These specific data products were chosen primarily for ease of use and that they are some of the most commonly utilized data from *Wind*. Figure 2 shows data taken from every region that *Wind* has visited in its 25+ years of observations from the magnetosphere, radiation belts, lunar environment, bow shock and foreshock regions, and solar wind. However, as noted above, the SWE Faraday cups cannot track the bulk of the thermal ion population while inside the magnetosphere because it is designed to measure a cold, fast beam. Thus, there are multi-hour data gaps in the SWE Faraday cup data during the >60 perigee passes through the magnetosphere. However, again the magnetometer data is perfectly valid. In fact, most of the large B_o values seen prior to 2004 are from magnetospheric passes. While these data products are not comprehensive of *Wind*'s capabilities, they are useful and illustrative of the longevity and diversity of environments that *Wind* has sampled.

3. Selected Science Results From *Wind*

This section starts by providing the reader with some background and contextual information that will be assumed in the subsequent subsections. The following subsections go on to summarize *Wind*'s contributions to numerous subfields within space plasma physics and astrophysics. The purpose is to illustrate both the breadth and importance of *Wind* in advancing our understanding of these fields. This section will also illustrate one of *Wind*'s greatest assets; the redundancies of some of its instruments which greatly improve the calibration and accuracy of the data products. Note that throughout this review, we intentionally prior-

Table 3
Operational Instruments on Wind

Name	Type	Cadence	Range	Status & notes
MFI				Nominal
	3 $B_{o,j}$[a]	~11–22 sps[b]	±4 to ±65,536 nT	±0.001 to ±16 nT
WAVES				**Nominal**
TDS Fast	2 δE_j	1.8–120 ksps	~0.1–300 mV/m	~80 μV rms
TDS Slow	1 or 3 δE_j	0.1–7.5 ksps	~0.5–300 mV/m	~300 μV rms
	1 or 3 δB_j	0.1–7.5 ksps	~0.25 to $\gtrsim$30 nT	~10^{-9} nT^2 Hz^{-1} @ 100 Hz
TNR	1 δE_j	~1 min	~4–256 kHz	~7 nV Hz$^{-1/2}$
RAD1	2 δE_j	~1 min	~20–1,040 kHz	~7 nV Hz$^{-1/2}$
RAD2	2 δE_j	~1 min	~1.1–14 MHz	~7 nV Hz$^{-1/2}$
3DP				**Nominal**
EESA	e^-	~3–22 s	~0.003–30 keV	~20% $\Delta E/E$[c], ~5.6–22.5°
PESA	H^+, He^{2+}	~3–75 s	~0.003–30 keV	~20% $\Delta E/E$, ~5.6–22.5°
SST Foil	e^-	~12 s	~25–400 keV	~30% $\Delta E/E$, $\gtrsim$ 22.5°
SST Open	H^+	~12 s	~25–6,000 keV	~30% $\Delta E/E$, $\gtrsim$ 22.5°
SWE				**VEIS Off,**
				Strahl Reconf.
FCs	H^+, He^{2+}	~92 s	~0.15–8 keV	~6.5% $\Delta E/E$
Strahl	e^-	~12 s	~0.005–5 keV	~3% $\Delta E/E$
				~3 ° × 30 °
SMS				**SWICS Off,**
				MASS Reduced
STICS	H–Fe	$\gtrsim$3 min	~8–226 keV/e	~5% $\Delta E/E$, ~4 ° × 150 °
			1–60 amu/e	~12% $\Delta M/M$[d]
EPACT				**IT off,**
				APE Reduced
LEMT	He–Fe	$\gtrsim$5–60 min	~2–12 MeV/n	$\gtrsim$20% $\Delta E/E$
			~2–90 Z	$\gtrsim$2% $\Delta Q/Q$[e]
STEP	H–Fe	$\gtrsim$10 min	~0.02–2.56 MeV/n	$\gtrsim$30% $\Delta E/E$
				~17 ° × 44 °
				Nominal
KONUS	photons	$\gtrsim$2 ms	~0.02–15 MeV	$\gtrsim$5% $\Delta E/E$
		$\gtrsim$3 s	~0.02–1.5 MeV	Background Mode
				Off (out of coolant)
TGRS	photons	$\gtrsim$62 μs	~0.025–8.2 MeV	~3 keV @ 1 MeV
			eff. ~43% @ 511 keV	

[a]Three magnetic field vector components. [b]Samples per second. [c]Normalized energy resolution. [d]Normalized mass resolution. [e]Normalized charge resolution.

itize *Wind*-centric references when available to help further illustrate the capabilities and diversity of *Wind*'s accomplishments. These citations are not meant to imply the reference was the first or seminal work on any given topic but to keep the focus on accomplishments by the *Wind* mission. We add notes/discussion, where appropriate, to help the reader distinguish between a *Wind*-centric and original/discovery paper.

Wind was designed to examine space plasmas. A plasma is an ionized gas exhibiting a collective behavior that is found in nearly all regions of space. Plasmas are mediated by long-range forces (i.e., electromagnetic) as well.

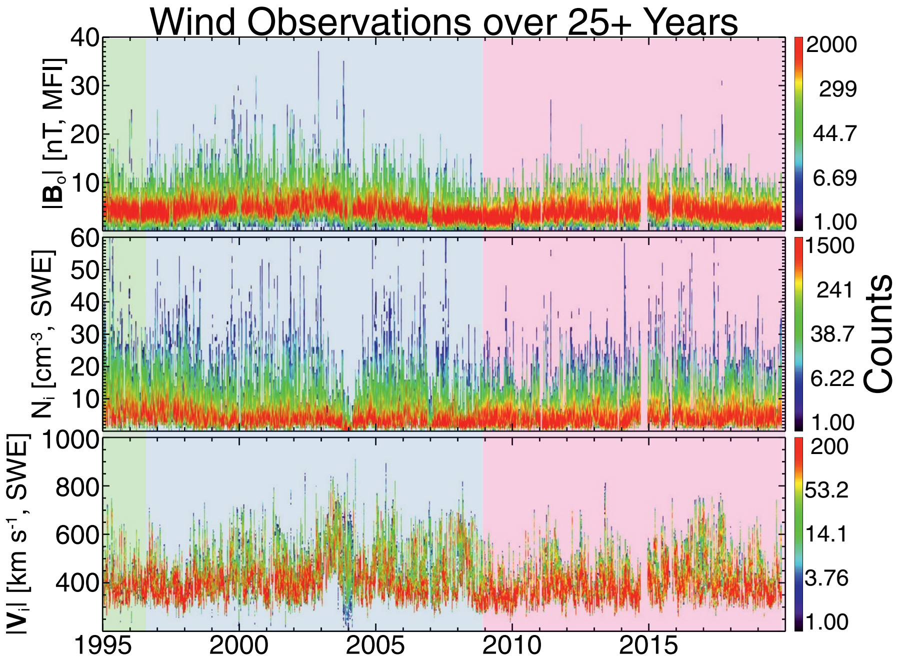

Figure 2. A 2D histogram representation of 25+ years of *Wind* observations. The panels are as follows from top to bottom: quasi-static magnetic field magnitude [nT], total ion number density [cm^{-3}], and total ion bulk flow speed [km/s]. The shading corresponds to solar cycles 22 (green), 23 (blue), and 24 (magenta). The color bars indicate the counts in each bin (see text for details).

The near-Earth environment (see cartoon in Figure 3) is comprised of a neutral atmosphere surrounded by a plasma (e.g., see review by Borovsky et al., 2020). The transition between the two is not abrupt. The neutral atmosphere consists of the troposphere, the stratosphere, the mesosphere, and a portion of the thermosphere. In the thermosphere, temperature increases as a function of altitude and as a function of extreme ultraviolet radiation. The ultraviolet radiation ionizes neutral constituents and gives rise to the ionosphere, a collisionally mediated, weakly ionized plasma. Above the ionosphere is the plasmasphere surrounded by the magnetosphere which is bounded by the magnetopause. Within the magnetosphere are the Van Allen radiation belts, magnetotail, and several other regions. The magnetosheath separates the magnetopause from the bow shock, one of the largest features of the near-Earth environment. The bow shock is the outermost boundary between the magnetosphere and the interplanetary medium (IPM) and solar wind. The magnetopause forms due to the Earth's magnetic field acting as an obstacle to the supersonic flow of the solar wind. The plasma compresses on the sunward side, piling up leading to a nonlinearly steepening fast/magnetosonic wave. Eventually this steepening wave reaches a balance between nonlinear steepening and energy dissipation, at which point the bow shock forms.

Table 4
Solar Wind Statistics

Solar cycle	n_i [cm^{-3}][a]	V_i [km s^{-1}]	B_o [nT]
Overall[b]	1.70–16.8, ~5.24	304–633, ~405	2.42–12.0, ~5.04
22 End	2.65–20.2, ~7.42	310–637, ~398	2.45–11.3, ~5.01
23 All	1.57–17.0, ~5.11	309–652, ~418	2.55–13.7, ~5.46
24 All	1.75–15.5, ~5.11	299–605, ~392	2.30–10.2, ~4.62

[a] $X_{5\%}$–$X_{95\%}$, $\tilde{X}$ (where $X_{y\%}$ is the yth percentile and $\tilde{X}$ is the median).
[b] Magnetospheric data are not included in the particle stats as SWE cannot measure magnetospheric ions.

Plasmas are ordered as collisionless, weakly collisional, collisional, and strongly collisional. A weakly collisional system is one in which the collision rate is small but not completely negligible compared to other relevant time scales (e.g., cyclotron frequency). The solar wind is an example of a weakly collisional, magnetized plasma that is constantly emitted from the Sun with variable speeds from ~280 km/s to >800 km/s (e.g., see Figure 2) and comprised of ~95% protons, ≳4% alpha-particles, and electrons (e.g., see review by Verscharen, Klein, & Maruca, 2019). In the solar wind near Earth, one Debye length is ~9 m while the scattering cross-sectional radius for neutral particles can be roughly six orders of magnitude smaller. Further, the transit time from the sun to the Earth for a typical solar wind parcel is ~3–4 days while the Coulomb collision period between particles is typically ≳0.5–1.0 days (e.g., see discussion in

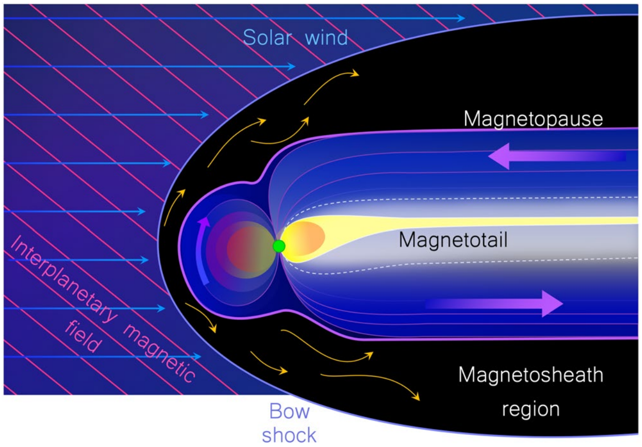

Figure 3. Cartoon of the Earth's global geospace environment (not to scale) shown in the plane orthogonal to the ecliptic.

Wilson et al., 2018, and references therein). Many plasmas, like that of the solar wind, are not in thermodynamic or even thermal equilibrium. That is, the temperatures of species s' and s are not equal or $\left(T_{s'} / T_{s}\right)_{tot} \neq 1$ for $s' \neq s$ (see Appendix A for symbol definitions) and there is an ubiquitous presence of finite heat fluxes, that is, nonequilibrium particle distributions. The former negates thermal equilibrium and both the former and latter negate thermodynamic equilibrium.

The collisionless limit is obviously that which ignores all Coulomb collisions on the time scales of interest. Shock waves in most space plasma environments are considered collisionless because the gradient scale length of the ramp tends to fall between the electron and ion inertial lengths (i.e., ~1–100 km near Earth) while the Coulomb collision mean free path of protons can be ~1 AU near-Earth (e.g., Wilson et al., 2018). Thus, they are called collisionless shocks.

A shock is a sudden transition between supersonic and subsonic flows and is characterized by an abrupt change in pressure, temperature, and density in the medium (e.g., see discussion in Krasnoselskikh et al., 2002; Shu, 1992; Wilson, 2016; Wilson et al., 2017, and references therein). Shock waves can arise from the nonlinear steepening of compressional waves when the steepening is balanced by some form of irreversible energy dissipation (e.g., see discussion in Shu, 1992). Despite their collisionless nature, shock waves can and do form in the solar wind. This can result either from some magnetic disturbance propagating faster than the supersonic solar wind (e.g., solar transient eruptions) or said disturbance standing against the incident solar wind (e.g., planetary bow shocks). A shock will arise if the difference in speed exceeds the fast magnetosonic speed (see Appendix A for definitions), that is, the relevant speed of communication in the medium.

Collisionless shock waves are distinguished by their Mach number (M_f), shock normal angle – the angle between the upstream average magnetic field vector and shock normal unit vector, θ_{Bn} (e.g., quasi-perpendicular shocks satisfy $\theta_{Bn} \geq 45°$), and upstream averaged plasma beta $\langle \beta_{tot} \rangle_{up}$. The asymmetric ram pressure/forces due to the supersonic solar wind combined with plasma coupling to the fields causes the Earth's magnetic dipole field to be "dragged out" into a tail with the appearance of something akin to a wind sock. On the sunward (upstream) side of the bow shock, this region of the quasi-parallel portion of the bow shock is called the ion foreshock (see Section 3.6 and Figure 7) and is filled with multiple backstreaming ion populations and energetic electrons (e.g., see discussion in Wilson, 2016; Wilson et al., 2016, and references therein). The interplanetary magnetic field (IMF) can be visualized as open solar magnetic field lines approaching Earth at ~45° to the Earth-Sun direction. The radial Sun-Earth line is along the horizontal in Figure 3 and the plane shown is orthogonal to the ecliptic.

A unique attribute of *Wind* for solar wind studies is that it is the only near-Earth spacecraft that consistently measures the "plasma line" (also known as the upper hybrid line) in the solar wind, which is primarily dependent upon the total electron density. The upper hybrid line is a thermal emission that occurs at the upper hybrid frequency, f_{uh} (see Appendix A for symbol definitions), and can be measured because the WAVES antennae are longer than the local Debye length, λ_{De} (see Table 6). The plasma frequency is so much larger than the cyclotron frequency in the solar wind, that is, $f_{pe} \gg f_{ce}$, that the following is almost always satisfied $f_{uh} \sim f_{pe}$. Even without this approximation, the spacecraft accurately measures the magnetic field so one can invert the observed upper hybrid line frequency to solve for the total electron density. This gives the only unambiguous measurement of the total electron density from any instrument and is used to calibrate the thermal particle detectors not just on *Wind*, but other spacecraft as well (e.g., THEMIS plasma instruments McFadden, Carlson, et al., 2008; McFadden, Phan, et al., 2008).

To understand charged particle motion, free energy, and instabilities we first introduce the concepts of particle VDFs. A VDF is a seven dimensional function of three spatial components, three velocity (or momentum) components, and one temporal component. Generally, spacecraft measure a VDF at a given time and location, so the VDF reduces to a three dimensional function of the 3-vector velocity (or momentum).

Generically speaking, the VDF is a probability density function of velocity for a particle ensemble. An example VDF is the well-known Maxwell-Boltzmann distribution, or Maxwellian (for more examples see Wilson et al., 2019b, and references therein).

Free energy in the context of space plasmas refers to non-Maxwellian features in a VDF such as temperature anisotropies, secondary beams, excess skewness (i.e., heat flux), etc. In general, any deviation from an isotropic Maxwellian is a form of free energy but the magnitude of the deviation is critical for determining whether or how that energy will be transformed. This definition of free energy derives from the assumption that an isotropic Maxwellian is the global, maximum entropy distribution.

A plasma instability is the mechanism through which a plasma converts some particle free energy source into electromagnetic fluctuations. Note that the use of both kinetic and plasma instability will occur throughout. The former specifically refers to features in the VDFs while the latter also encompasses fluid-like instabilities. All thermal plasmas contain pre-existing thermal fluctuations at the natural frequencies of the system, often called normal modes (e.g., see discussion in Gary, 1993; Stix, 1992). The properties of these normal modes depend on the background plasma parameters (e.g., magnetic field strength, density, temperature, etc.). The normal modes determine which possible thermal fluctuations can absorb the free energy from the particle populations, if present, and grow over time above the thermal amplitude level. In some ways, an instability is like a “walkie talkie” between the source (particle free energy) and receiver (electromagnetic fluctuations). In this analogy, the transmitting walkie talkie channel frequency is analogous to the pre-existing normal modes of the system while the receiving walkie talkie is analogous to the electromagnetic modes. For more details and specific examples of instabilities, see Appendix B.

Another topic of considerable interest in plasma physics is magnetic reconnection. Magnetic reconnection is a universal plasma process by which a change in the magnetic field topology results in the destruction of magnetic flux and the conversion of electromagnetic energy to particle kinetic energy (see Hesse & Cassak, 2020, for a detailed review). Magnetic reconnection has been known to be an important particle energization mechanism in astrophysical plasmas for decades. It occurs in response to the compression of regions with oppositely directed magnetic fields. As the oppositely directed magnetic fields slowly converge, a current sheet begins to form creating a spatially thin region called the diffusion region (Sonnerup, 1979). Traditionally this is associated with a so called “X-line” or place where the magnetic field lines trace out an X (e.g., see the gray boxes in the cartoon in Figure 6). The diffusion region is where magnetic flux is destroyed and electromagnetic energy starts to convert to particle kinetic energy forming two oppositely directed, outflowing jets, called “reconnection exhausts.”

When the magnetic field changes on shorter spatial scales than the particles can respond (i.e., they can no longer follow a single magnetic field line), they are said to be demagnetized. The magnetic reconnection process starts in the diffusion region, which is characterized by the presence of dissipative electric fields on small length scales (i.e., smaller than the particle gyroradii and/or inertial length). There are in fact two diffusion regions, one for the electrons and one for the ions. When inside of the ion diffusion region, thermal ions become demagnetized but electrons can still remain magnetized. However, inside the electron diffusion region, both particle populations become demagnetized. The presence of dissipative fields allows changes in magnetic field topology by redistributing energy between fields and particles resulting in large scale (much larger than ion gyroradii and/or inertial lengths) consequences.

In the following subsections we highlight selected scientific discoveries and/or advances made using *Wind* observations.

3.1. Remote Astrophysics

3.1.1. Gamma Ray Bursts

Cosmic gamma ray bursts (GRBs) are the brightest electromagnetic events known to occur in the universe and are triggered by the collapse of massive stars (long GRBs) or the coalescence of compact objects (short GRBs). Even though the call for proposals to the ISTP program had already taken place, the discovery of gamma ray bursts in the 1970s by Klebesadel et al. (1973) prompted the addition of two gamma ray detectors

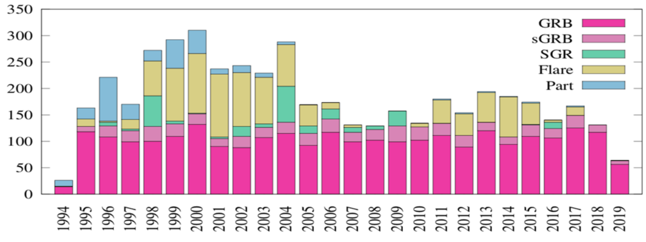

Statistic of ~4700 KW triggers from November 1994 to mid-2019.

Figure 4. KONUS statistics of various astrophysical events emitting gamma rays. The vertical axis is number of events. The color code corresponds to the type of burst trigger for the instrument, which are defined as: GRB is gamma ray burst (≳2740, magenta); sGRB is short gamma ray burst (~500, purple); SGR is soft gamma repeater (~270, green); Flare is solar flare (≳1040, yellow); and Part is particle event-induced (taken from Figure 1 in D. Frederiks et al., 2019).

to the *Wind* instrument payload, the KONUS (Aptekar et al., 1995) and TGRS (A. Owens et al., 1995) experiments. The KONUS instrument, also called KONUS-W, is the first Russian instrument to fly on a US spacecraft. KONUS is the most prolific detector in the Interplanetary Network (IPN, http://ssl.berkeley.edu/ipn3/index.html), which contains gamma-ray detectors from a variety of telescopes, including *Swift* and *Fermi* (Cline et al., 2001; Hurley, Cline, et al., 2003; Hurley, Atteia, et al., 2003; Hurley et al., 2011), maintained by Dr. Kevin Hurley at UC Berkeley. KONUS is also a member of the Gamma-ray Burst Coordinates Network or GCN (https://gcn.gsfc.nasa.gov), maintained by Dr. Scott Barthelmy at NASA's Goddard Space Flight Center.

By studying GRBs, we can learn about the formation of large-scale structures in the early universe and present-day processes (Fishman, 1995; Fishman & Meegan, 1995). GRBs consist of an initial flash of gamma-rays lasting from tens of milliseconds to minutes followed by a longer duration afterglow at radio and optical wavelengths. KONUS's combination of broad energy range, longevity, and all-sky coverage make it a unique resource for many studies (e.g., Tsvetkova et al., 2017). For a particularly bright short event, Guiriec et al. (2017) find unique evidence of a photospheric jet by comparing simultaneous KONUS and *Fermi* observations. In 2019, the gravitational wave facilities Advanced LIGO and Virgo provided evidence of short GRBs associated with both binary neutron star mergers and the emission of gravitational radiation (Abbott et al., 2019). The authors also cite *Wind* data from the Interplanetary Network in their study. As of 2020, 300 bursts per year are detected by KONUS (roughly 6000 to date). Figure 4 shows the number of GRBs detected by KONUS between 1994 and 2019 (D. Frederiks et al., 2019).

3.1.2. Soft Gamma Repeaters (Magnetars)

Soft gamma repeaters (SGRs), also called magnetars, are strongly magnetized Galactic neutron stars with surface magnetic fields up to 10^{14} G. Magnetars emit large bursts of X-rays and gamma-rays at irregular intervals (Aptekar et al., 2002; Kouveliotou et al., 1999). Approximately 30 magnetars have been identified. When these sources become active, they emit several up to several hundreds of bursts within a timeframe of days to months.

Magnetar giant flares (GFs) are of greater apparent intensity than GRBs with an average occurrence rate of once per decade (Frederiks et al., 2007; Hurley et al., 2010). Only a handful of GFs have been detected. The intensity of a single event is sufficient to create ionospheric disturbances. KONUS has detected extragalactic GFs from the Andromeda and the M81 group (Frederiks et al., 2007; Mazets et al., 2008) and more recently identified a GF from the Sculptor galaxy (Roberts et al., 2021; Svinkin et al., 2021).

Fast radio bursts (FRBs) are bright, millisecond-scale radio flashes whose origins are a subject of debate (e.g., see review by Petroff et al., 2019). Magnetars have been suggested as the most promising candidates for fast radio burst progenitors owing to their energetics and high X-ray flaring activity, but proof of this association has been elusive. KONUS detected a burst of X- and gamma-rays on April 28, 2020 (Bochenek et al., 2020; CHIME/FRB Collaboration et al., 2020; Ridnaia et al., 2020) which was temporally coincident with a bright, two-peak fast radio burst; the light curves of the radio and X-ray bursts were remarkably similar. The source was the Galactic magnetar SGR 1935+2154, which had recently entered an active state. This was the first simultaneous detection of a fast radio burst from a Galactic magnetar and its high-energy counterpart, and it provides the long-sought evidence of a magnetar origin for at least some FRBs.

3.1.3. Solar Flares

During its more than 25-year-long history, the KONUS instrument onboard *Wind* has accumulated an unique volume of solar flare observations in the hard X-ray and gamma ray range. Data on solar flares recorded by KONUS in the triggered mode are published online (http://www.ioffe.ru/LEA/kwsun/) from 1994 to the present along with their GOES classification (Pal'shin et al., 2014). This database (see Table C1 in Appendix C) provides light curves with high temporal resolution (up to 16 ms) and energy spectra over a wide energy range (now ~20 keV to ~15 MeV). The high time resolution of KONUS allows for the study of fine temporal structure in solar flares (e.g., Lysenko et al., 2018). The KONUS energy band covers the region of nonthermal emission due to accelerated electrons and ions in solar flares, which allows probing the source of their acceleration (e.g., Glesener & Fleishman, 2018). Thus, the *Wind* KONUS solar flare database offers a new, unique set of data for solar researchers.

3.2. Interstellar and Interplanetary Dust

The interplanetary and interstellar media are full of small debris ranging in size from millimeters to nanometers called dust. Dust is important as it can readily transport mass, momentum, and energy throughout the heliosphere but the sources, sinks, and transport are not well understood. Most of this dust is moving at large speeds relative to spacecraft, resulting in hypervelocity impacts when dust grains collide with spacecraft. Such collisions convert enough kinetic energy to ablate and ionize small portions of the spacecraft causing a plasma plume to form. This abrupt ionization may be detected with high time resolution electric field instruments, as the plasma plume and ejected material affects the electric fields near the spacecraft (e.g., see review by Sterken et al., 2019). Although the original *Wind* mission objectives did not include the detection of dust, the *Wind*/WAVES TDS receiver has accumulated >100,000 identified dust impacts (Malaspina & Wilson, 2016).

Researchers determined that the signals corresponded to micron-sized (i.e., dust grains ~1 μm in size) interplanetary dust (IPD) and interstellar dust (ISD) (Malaspina et al., 2014; Sterken et al., 2019). Wood et al. (2015) then determined the longitudinal direction of ISD using spectroscopic measurements from *Ulysses*, which was orbiting the solar poles. Although dust had been detected previously using the same method on other spacecraft (Malaspina et al., 2015; Mann et al., 2019; Sterken et al., 2019), Wood et al. (2015) presented the first antenna triangulations of ISD with the *Wind* and *Ulysses* spacecraft across an entire solar cycle. They utilized the yearly modulation of dust count rates to separate ISD from IPD. The authors show an unexplained source of variability in 2005 on a timescale of less than a year. This temporal variability is interesting because it deviates from the expected temporal variability of the dust count rates and remains unexplained.

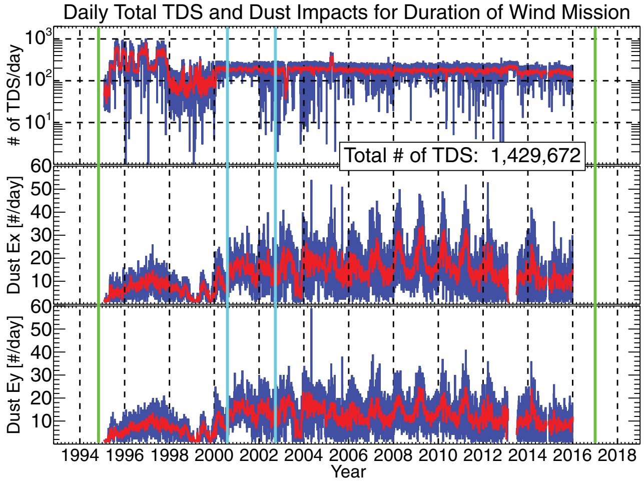

Figure 5. Plot of the entire *Wind* mission showing the daily totals. In each panel the dark blue and red lines represent the actual and 10-day smoothed counts, respectively. The panels shown are the following (in order from top-to-bottom): daily total number of TDS events; number of dust impacts observed on the x-antenna; and number of dust impacts observed on the y-antenna. The two vertical green lines define the duration of the Wind mission at the time of creation of this figure (i.e., January 2017). The two vertical cyan lines define the times when the x-antenna was cut apparently by dust impacts (Adapted from Figures 5 and 6 in Malaspina & Wilson, 2016).

Subsequent work led to the creation of a *Wind* dust impact database (Malaspina & Wilson, 2016), comprised of >107,000 impacts, which is publicly available through SPDF CDAWeb (see Table C1 in Appendix C). The large statistics allowed researchers to determine that *Wind* does not respond to dust grains with sizes ≪0.1 μm, the so called nanodust (Kellogg, 2017; Kellogg et al., 2016, 2018; Malaspina et al., 2014; Malaspina & Wilson, 2016; Sterken et al., 2019).

Figure 5 shows the counting statistics for TDS events and dust impacts observed by the *Wind* TDS receiver. The obvious annual variation in dust impacts seen in the bottom two panels is primarily due to ISD. The reason is that for half of the year, *Wind* is moving approximately anti-parallel to the flow of ISD through the solar system. The difference in flow speed of the ISD in *Wind*'s reference frame varies from ~4–56 km/s, thus leading to an annual variation in the counting rates (i.e., higher impact speeds produces larger electric field amplitudes and thus more dust observations). This annual variation has been reported in multiple studies (Kellogg et al., 2016; Malaspina et al., 2014; Malaspina & Wilson, 2016; Wood et al., 2015).

The *Wind* dust impact database presents exciting opportunities for investigating heliospheric dust dynamics (Sterken et al., 2019) and statistical studies of the dependence on large-scale, transient magnetic phenomena (see Sections 3.8.2 and 3.8.3). The relevance of dust has increased in recent years with the recognition that it plays an important role in numerous ways from mass, momentum, and energy transport to physical damage to spacecraft (e.g., cutting of wire antenna). For instance, one of the wire antennas, that form the electric field probes for *Wind*/WAVES, was cut twice by what is suspected to be dust impacts. The first occurrence happened on August 3, 2000 and the second time on September 24, 2002.

Finally, a more recent development arose when researchers using an Earth-observing spacecraft, Aeronomy of Ice in the Mesosphere (AIM) (Russell et al., 2009), found some variations in meteoric smoke—the product of meteoroid ablation (at ∼75–110 km altitude) in Earth's mesosphere. These observations were made by the Solar Occultation For Ice Experiment (SOFIE) (Gordley et al., 2009). Although the mission is cloud-focused, cloud science overlaps with studies of dust, geomagnetic activity, and solar cycles (Hervig et al., 2017, 2019; Liu et al., 2018). Interestingly, the temporal variations in meteoric smoke are consistent with the dust count rates observed by *Wind*, providing a new avenue of research and future collaborations.

Table 5
Optical Lunar Wake Transits by Wind

Start time [UTC]	End time [UTC]
1994-12-01/15:04:07	1994-12-01/15:29:10
1994-12-27/14:36:30	1994-12-27/15:22:36
1996-03-24/05:19:43	1996-03-24/06:24:50
1996-11-13/01:43:16	1996-11-13/03:07:25
1999-04-01/20:38:02	1999-04-01/20:53:04
1999-05-12/20:52:12	1999-05-12/21:04:14
2000-08-19/15:35:45	2000-08-19/16:51:53
2001-12-05/16:48:53	2001-12-05/17:54:00
2002-07-18/17:46:39	2002-07-18/18:42:45
2002-11-30/11:30:28	2002-11-30/12:16:33

3.3. Lunar Wake Studies

Because the moon is relatively nonconducting, the interplanetary magnetic field passes through the obstacle while solar wind ions and electrons only interact with the lunar surface. *Wind* offered the first modern glimpses into the lunar wake in 1994 - The first lunar wake observations by the *Explorer 35* and *Apollo* missions occurred at around 2 lunar radii from the lunar surface (Ness, 1972) - giving inspiration to new simulation efforts focusing on kinetic phenomena (e.g., see historical discussion in review by Halekas et al., 2015). *Wind* completed 10 wake crossings before entering a Lissajous orbit at L1 in 2004. Table 5 lists all crossings of the lunar optical wake (Ogilvie & Desch, 1997).

The lunar environment is an exciting laboratory for plasma physics (Halekas, Angelopoulos, et al., 2011; Halekas, Saito, et al., 2011; Halekas et al., 2015), comparative planetology, solar system formation, and astrochemistry. As a result, the near-moon plasma environment has a low-density downstream cavity called a wake. *Wind* contributed the first wake measurements more than two lunar radii or R_L from the surface (Bosqued et al., 1996; Farrell et al., 1998; Owen et al., 1996). Ogilvie et al. (1996) presented wake field and particle observations which contradicted the previously accepted theory of a magnetohydrodynamic (MHD) wake flow. The spatial scale of magnetic field perturbations near the wake should be much larger than an electron orbit while the ions are on a ballistic trajectory interacting with an unmagnetized body. Therefore, the ions and electrons could be treated like a fluid around such an obstacle. This is why some of the original work suggested an MHD model approach (Farrell et al., 1997; Ogilvie et al., 1996).

This MHD model predicted that the lunar wake would extend to no more than four lunar radii or ∼4 R_L (Bosqued et al., 1996; Farrell et al., 1998; Owen et al., 1996). However, *Wind* still observed a wake at ∼6 R_L (Bosqued et al., 1996; Farrell et al., 1996; Kellogg, Goetz, et al., 1996; Ogilvie et al., 1996; Owen et al., 1996). The alignment of the lunar wake with optical shadow helps us understand the complex ion and electron flow patterns which act to replenish the low-density cavity (Clack et al., 2004). In the lunar wake, *Wind* observed oppositely directed ion beam distributions (Farrell et al., 1997; Ogilvie et al., 1996). These beams are a response to asymmetric ambipolar diffusion. Thus, *Wind* provided paradigm shifting observations showing us that the plasma-moon interaction is kinetic, not fluid, in nature.

3.4. Reconnection in the Magnetotail

Magnetic reconnection has been known to be an important particle energization mechanism in astrophysical plasmas for decades (see Hesse & Cassak, 2020, for a detailed review). This section describes magnetic reconnection discoveries made using *Wind* data in the magnetotail – the region anti-sunward of Earth where Earth's magnetic dipole field lines are stretched and compressed due to the solar wind.

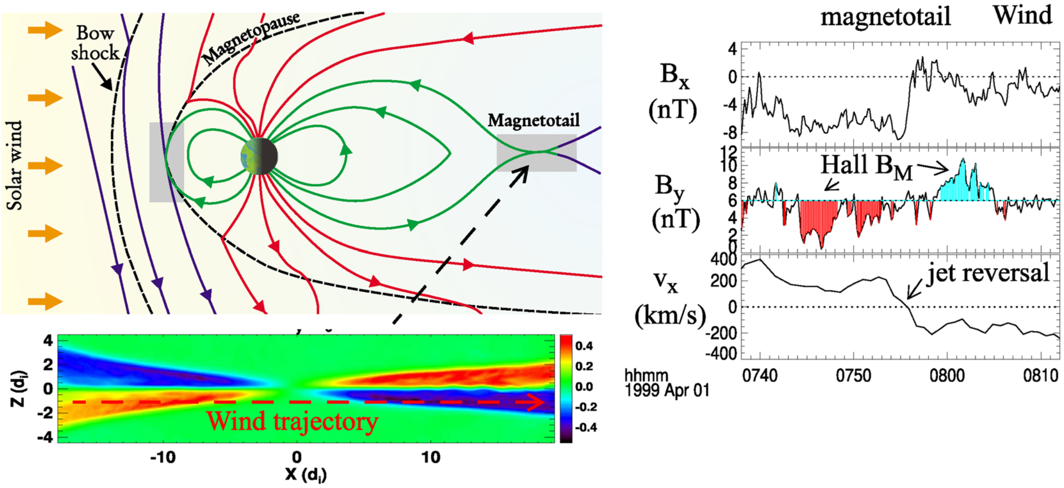

Figure 6. *Wind* encounter with the magnetic reconnection ion diffusion region in Earth's magnetotail, showing (right) the out-of-plane Hall magnetic field B_y and the reversal of the reconnection reconnection outflow jets across the reconnection region. The simulation panel shows the normalized Hall B_y with *Wind*'s trajectory overlaid (red dashed line). Note that the polarity in the simulation is different from the which is a consequence of the coordinate basis (Modified from Figures 1 and 2 in Øieroset et al., 2001).

Although early observations associated with reconnection in space provided evidence of the reconnection process through downstream outflows identified as exhausts, the diffusion region was not observed directly (e.g., Paschmann et al., 1979). The observational discovery of the magnetic reconnection (ion) diffusion region was made in Earth's magnetotail at ~60 R_E by *Wind* (Øieroset et al., 2001). The primary evidence of reconnection presented in this study was the quadrupolar (Hall) magnetic field around an X-line crossing (see Figure 6), which caused the ions to become demagnetized as they enter the diffusion region. In the same reconnection event, *Wind* found direct evidence that reconnection can accelerate electrons to suprathermal energies, up to 300 keV (Øieroset et al., 2002). The *Wind* findings led to new ideas of particle energization in magnetic reconnection which were developed to explain the observed suprathermal electron energization. In particular, Drake et al. (2006) suggested that electrons could gain kinetic energy by reflecting from the ends of the contracting "magnetic islands" that form in the current sheet as reconnection proceeds. The mechanism is analogous to the increase of energy of a ball reflecting between two converging walls – the ball gains energy with each bounce. The repetitive interaction of electrons with many magnetic islands allows a large number of electrons to be efficiently accelerated to high energy.

Raj et al. (2002) found a clear dawn-dusk asymmetry in the occurrence of magnetic reconnection in *Wind* observations in Earth's magnetotail. Reconnection occurred preferentially on the dusk side, which links tail reconnection to nightside auroral intensifications (these are known to be strongly skewed toward the dusk/pre-midnight sector). The *Wind* discovery led to a number of studies trying to explain the source of the asymmetry, including ionospheric control of tail reconnection Lotko et al. (2014).

3.5. The Radiation Belts

Wind studies of large amplitude whistler waves in the terrestrial radiation belts (Kellogg et al., 2011; Kersten et al., 2011; Wilson III et al., 2011) have led to a series of new theoretical analyses based upon the new, much larger wave amplitude estimates (note these were originally discovered by Cattell et al., 2008, using STEREO observations). A comprehensive review of large amplitude whistler mode waves in the radiation belts can be found in the review by Cattell et al. (2012). Whistler mode waves are right-hand polarized (with respect to quasi-static magnetic field), electromagnetic emissions that are found in virtually all regions of space (e.g., see discussions in Cattell et al., 2012; Wilson, 2016; Wilson, Koval, Szabo, et al., 2013, and references therein). In the context of the radiation belts, the words *whistler mode wave* includes both chorus-like and hiss-like emissions. See the Glossary and Appendix B for more details.

The peak-to-peak electric and magnetic field amplitudes of whistler mode waves can exceed 200 mV/m and 8 nT, respectively (Kellogg et al., 2011; Wilson et al., 2011). These values are >10 times the magnitude of previous observations and call into question the assumptions required in quasi-linear diffusion models that are based upon much smaller wave amplitudes (e.g., see review by Cattell et al., 2012). For each magnetospheric pass examined that traversed the radiation belts, Wilson et al. (2011) found that large amplitude waves were present in the radiation belts. Kellogg et al. (2011) used *Wind* to provide some of the first evidence that these waves were being excited by electrons with energies below ~30 keV – previous work suggested that energies of at least 100 keV were necessary to excite whistler mode waves in the radiation belts. Kellogg et al. (2011) also showed evidence of electron beam-driven electrostatic solitary waves in conjunction with large amplitude whistler mode waves. This result suggested that the energy budget and particle dynamics of the radiation belts are not as well understood as previously thought.

Wilson et al. (2011) showed that the whistler mode wave amplitudes had a weak positive correlation with the auroral electrojet index or AE-Index – a set of space weather numerical values designed to provide a global, quantitative measure of auroral zone magnetic activity produced by enhanced ionospheric currents. The large amplitude whistler mode waves in this study were concurrent with earthward injections of ~30–300 keV electrons from the geomagnetic tail. Wilson et al. (2011) also obtained a lower bound on the Poynting flux of one wave, which was $\gtrsim$300 μW m^{-2}, or nearly four orders of magnitude larger than any previous measurement for radiation belt whistler mode waves. A previous statistical survey of whistler mode chorus Poynting flux found typical amplitudes of ~0.05 μW m^{-2} (Santolík et al., 2010). The authors used this value to estimate the time scale for filling a ~3 R_E long, field-aligned column flux tube in the radiation belt with ~1 MeV electrons energized from typical plasma sheet energies (i.e., ~200–10^4 eV). Assuming a 1% efficiency Santolík et al. (2010) estimated that chorus could fill the outer radiation belt in a matter of days, consistent with the then standard assumption of the radiation belt refilling time scale of ~1 day (Horne et al., 2005). For comparison, using the $\gtrsim$300 μW m^{-2} *Wind* observation and a 1% efficiency, the time scale decreases to ~33 s providing further evidence that the energy budget and particle dynamics of the radiation belts were not as well understood as previously thought.

These *Wind* studies also helped to define some of the primary science goals for the electromagnetic fields instruments (Wygant et al., 2013) on NASA's *Van Allen Probes*, which were launched in 2012. The *Wind*-estimated timescale of sub-minute energization was considered much too short at the time of publication but later studies using *Van Allen Probes* (Agapitov et al., 2019) reduced the upper limit to less than ~3 h from the previous ~12–24 h time scales. Note these time scales are for electrons below ~1 MeV. Changes in electrons at or above ~1 MeV are still in the ~12 h time range. *Wind* also serves as an upstream monitor for radiation belt studies by the *Van Allen Probes* and other magnetospheric missions (Borovsky & Denton, 2009; Halford et al., 2015; Jaynes et al., 2015; Li et al., 2015; Mann et al., 2016; Schiller et al., 2014; Turner et al., 2014).

In summary, *Wind* observations have led to paradigm shifting results in radiation belt studies specifically on particle energization and loss, modeling, and wave generation.

3.6. The Ion Foreshock

In this section, we discuss the advances made by *Wind* studies to our understanding of the terrestrial foreshock – the region magnetically connected to the quasi-parallel shock. Studies using *Wind* have shown the foreshock is far larger in spatial extent than previously thought, giving us insight into new transient, electromagnetic phenomena, and showed that foreshock transients can locally generate their own miniature foreshocks. Figure 7 shows a cartoon example of a possible foreshock scenario illustrating the multiple particle population regions and the presence of large amplitude electromagnetic fluctuations/disturbances (see Wilson, 2016, for detailed review of the foreshock).

The spatial extent of shock-reflected ions defines the foreshock boundaries. Prior to *Wind*, the most distant foreshock measurement was made by ISEE-3 at 200 R_E, *Wind*'s predecessor (Scholer et al., 1980). Using *Wind*, Berdichevsky et al. (1999) discovered that the ion foreshock could extend to ~250 R_E from Earth. Using a combination of *Wind* and STEREO observations, Desai et al. (2008) subsequently found ion foreshock particles > 3,000 R_E upstream.

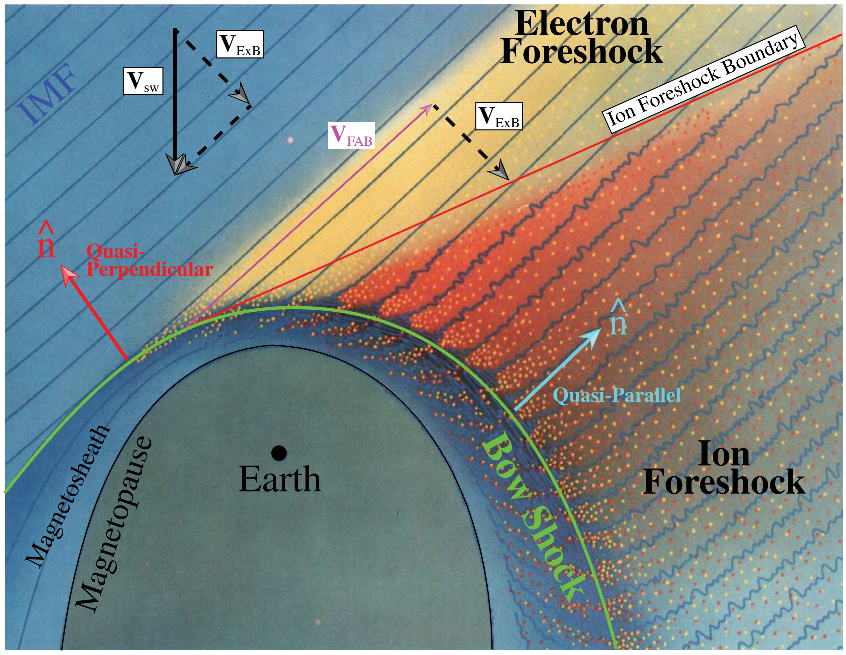

Figure 7. A cartoon example of a possible terrestrial foreshock configuration. The IMF is represented by the dark blue lines, $\mathbf{V}_{sw}$ represents the bulk solar wind velocity, $\mathbf{V}_{ExB}$ is the $(E \times B)$-drift velocity due to the solar wind convection electric field, and $\mathbf{V}_{FAB}$ is the reflected field-aligned ion beam velocity (Adapted from Figure 1 of Wilson, 2016).

In addition to redefining the extent of the foreshock, *Wind* observations also showed that the high energy cutoff for energetic ions is higher upstream of the quasi-perpendicular bow shock (Meziane et al., 1999, 2002, 2003) rather than the quasi-parallel bow shock, in contrast with theory (Caprioli & Spitkovsky, 2014; Park et al., 2015). Upstream of the quasi-parallel bow shock the highest energy ions only reach ∼330 keV while upstream of the quasi-perpendicular bow shock the highest energy ions can reach ∼2 MeV through shock drift and/or diffusive shock acceleration. These energetic ions were observed to be "gyrophase-bunched"(a beam localized in velocity space and not symmetric about $\mathbf{B}_o$) due to their single, adiabatic reflection off of the bow shock.

At lower energies below ∼30 keV, *Wind* observations revealed that magnetic field-aligned ion beams could become disrupted by waves (Mazelle et al., 2000; Meziane et al., 1997, 2001). These three studies presented the first *in situ* evidence that ion-generated foreshock waves can modify foreshock ion velocity distributions by scattering and trapping the particles.

Wind has also played a pivotal role in our understanding of transient ion foreshock phenomena (TIFP) – large-scale (∼1,000 to > 30,000 km), solitary [∼5–10 per day and transient] structures with durations of tens of seconds to several minutes (Sibeck et al., 2002, 2004; Wilson, Koval, Sibeck, et al., 2013; Zesta & Sibeck, 2004). For instance, Sibeck et al. (2002) used *Wind* to identify a new transient ion foreshock phenomenon, called a foreshock cavity, which is driven by a diamagnetic effect due to shock-accelerated ions. Foreshock cavities are diamagnetic regions surrounded by density enhancements and filled with suprathermal particles. Unlike a somewhat similar phenomena, hot flow anomalies, foreshock cavities do not show significant bulk flow velocity deflections, no dramatic ion temperature increase, and they are not centered on an IMF discontinuity. More recently, Wilson, Koval, Sibeck, et al. (2013) used *Wind* to show that transient ion foreshock phenomena can locally reflect ions, generating their own miniature foreshocks. This discovery was completely unexpected because it showed that a collisionless shock can self-consistently energize particles through a multi-step process: (1) the bow shock reflects incident ions; (2) the reflected ions stream against the incident solar wind; (3) the counter-streaming ion beams are unstable and generate TIFP; (4) the TIFP locally energize particles; and (5) these pre-energized particles interact with bow shock and gain even more energy.

In an adjacent region of space called the electron foreshock (see Figure 7), *Wind* provided the some of the first determinations of the source of radio emissions near 2 f_{pe} (Reiner et al., 1996, and see Section 3.10 for more discussion of radio measurements). The work showed the source region was within the electron foreshock and that the emission lacked a distinct polarization, which helped advance our understanding of 2 f_{pe} emissions and reduced the number of possible sources. *Wind* measurements also allowed researchers to examine some of the first time series electric fields of Langmuir waves (Kellogg, Monson, et al., 1996). Electron and ion foreshock processes are relevant to a range of space plasma phenomena, including waves in the lunar wake (see Section 3.3), waves in the solar wind (see Section 3.7.2, magnetotail reconnection (see Section 3.4), and waves upstream interplanetary shocks (see Section 3.8.1).

In summary, *Wind* observations have led to paradigm shifting results in multiple areas of foreshock research and opened up new avenues for future studies.

3.7. Solar Wind Studies

This section focuses on *Wind*'s contribution to several fields of solar wind physics. The section is broken up into four parts including large-scale magnetic phenomena (Section 3.7.1), kinetic instabilities and waves (Section 3.7.2), plasma turbulence (Section 3.7.3), and long-term statistical studies (Section 3.7.4).

3.7.1. Large-Scale and Reconnection Investigations

Wind's diverse orbits (Figure 1) combined with large spatial separation from multiple other spacecraft provided unique opportunities to investigate large-scale magnetic phenomena from solar wind structures, large-scale turbulence, interplanetary (IP) shocks, and solar transients. This section reviews *Wind*'s contribution to advancing our understanding of these phenomena on large spatial scales.

The prograde orbits extending tangentially in the east/west direction and separated from Earth by up to 1° in heliolongitude provided an opportunity for observations separated by much larger distances from Earth than is possible using spacecraft at L1. In fact, *Wind* holds the record for the most time spent at 65–500 R_E ($2.5 \times 10^{-3} - 0.02$ AU) tangentially from Earth (similar distances were reached by the STEREO spacecraft in March-April 2007). Investigations using observations from *Wind* and other spacecraft allowed researchers to test theories of very large scale turbulence (Ogilvie et al., 2007; Wicks et al., 2009, also see Section 3.7.3), solar energetic particles and energetic storm particles (Neugebauer & Giacalone, 2005; Neugebauer et al., 2006, see Section 3.9), the curvature/shape of IP shocks (Koval & Szabo, 2010), and the spatial coherence of interplanetary coronal mass ejections or ICMEs (Farrugia et al., 2005; Möstl et al., 2008; Lugaz et al., 2018, see Section 3.8.2).

Energetic storm particles (ESPs) are particles locally accelerated by an IP shock and have typical energies between 100 keV and 10 MeV. ESP events are typically classified into the following types depending on their temporal profile: spike, rise, step, flat and complex (Lario et al., 2003; Tsurutani & Lin, 1985). There is no simple relationship between the presence/absence and type of ESP events and shock parameters, such as speed, Mach number, or shock normal angle (Cohen, 2006). To understand how the acceleration of particles varies along the shock front, ESP measurements made by *Wind* and ACE of the same events were compared, when *Wind* was in prograde or petal orbits. The analyses of 86 ESP events measured for small longitudinal separations (<0.7°) revealed that the measurements become less correlated as the spacecraft separation increases (Neugebauer et al., 2006; Neugebauer & Giacalone, 2005).

The global radius of curvature of CME-driven shocks (Janvier et al., 2015) is thought to be 0.2–1 AU. This is one of the fundamental quantities that describes shocks since it characterizes the variation of the large-scale shock normal angle (the angle between the shock normal and the magnetic field) along the shock front. However, for smaller spacecraft separations (<0.5°), Koval and Szabo (2010) examined 62 shocks measured by *Wind* and at least one other spacecraft (i.e., ACE, *Geotail*, IMP-8, *Interball-1*, and/or SoHO) to determine the shock radius of curvature. The largest shock curvature that could be determined was 0.04 AU, that is, it reflects the "large-scale local" not global properties of the shock.

Taking advantage of *Wind*'s visit to Earth's magnetotail while ACE remained in an orbit at L1 in October-November 2003, Farrugia et al. (2005) calculated the radial correlation length inside ICMEs (see Section 3.8.2)

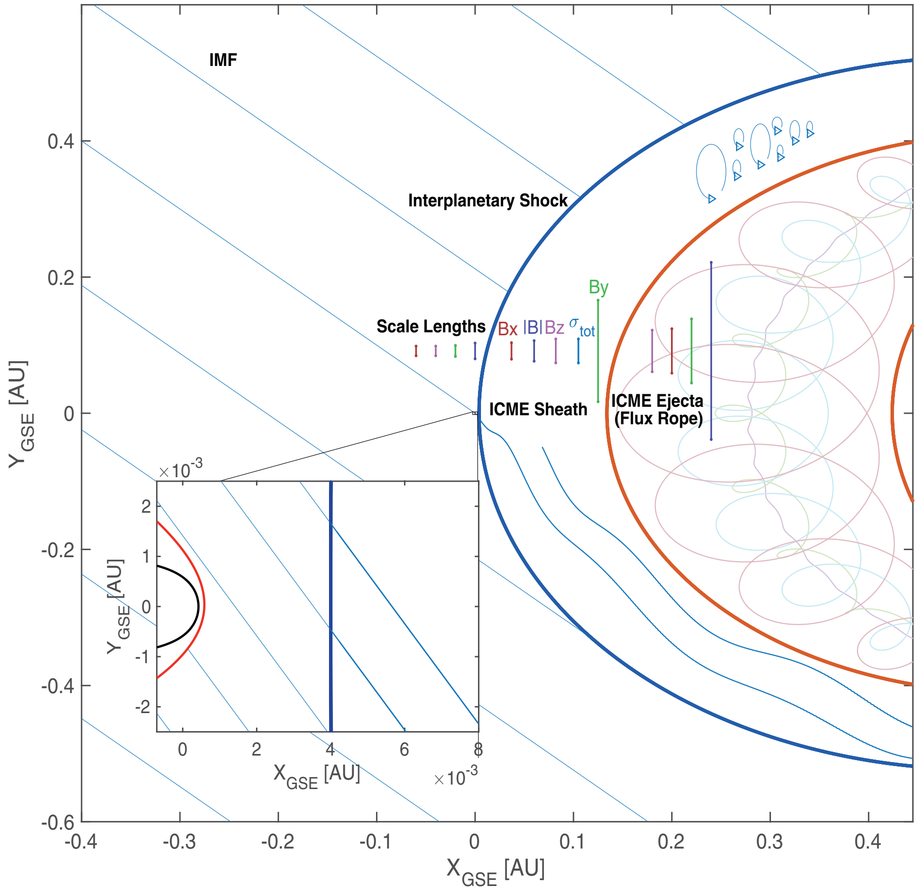

Figure 8. Sketch of an ICME in Earth-centered interplanetary space in the ecliptic plane with scale lengths. The ICME sheath is preceded by an interplanetary shock (dark blue curve) and driven by the ICME ejecta, bounded by orange curves. The ICME is modeled as arcs of a circle by taking the average angular width of the ICME ejecta given by Zhao et al. (2017) and the average radial width reported by Kilpua, Balogh, et al. (2017) for the sheath. Blue lines show and IMF with a 45° Parker spiral angle at the Earth's distance from the Sun. Scale lengths of the solar wind (Richardson & Paularena, 2001), ICME sheath (Ala-Mathi et al., 2020), and ICME ejecta (Lugaz et al., 2018) are illustrated in the *y*-direction with the color corresponding to the magnetic field component and magnitude as indicated for the sheath region. The correlation in light blue (σ_{tot}) illustrate the scale length associated with the overall Pearson correlation obtained by applying the averaging estimator of correlation coefficients for the Pearson correlation values of the magnitude and components (Adapted from Figure 6 in Ala-Mathi et al., 2020).

using observations from the two spacecraft radially separated by 0.02 AU, while Möstl et al. (2008) performed one of the first two-spacecraft reconstructions of a magnetic cloud. *Wind* underwent distant prograde orbits during the maximum phase of solar cycle 23 (2000–2002), that is, *Wind* moved up to 0.01 AU tangentially (east-west in GSE coordinates) of the Sun-Earth line while measuring more than two dozen ICMEs. Lugaz et al. (2018) used these periods to calculate the nonradial correlation length inside ICMEs. Later Ala-Mathi et al. (2020) used the same observations to calculate the correlation length inside the sheath regions of ICMEs. Combined with measurements of the correlation lengths in the IP space, a picture of the coherence of ICMEs near one AU has emerged as shown in Figure 8. The correlation scale lengths of the magnetic field inside ICME ejecta were found to be larger than the scale lengths in ICME sheaths, themselves larger than the scale lengths in the solar wind, as expected. In addition, the correlation scale length of the magnetic field magnitude inside ICME ejecta was very close to the average ejecta radial width of 0.21 AU (Lepping et al., 1990). However, the correlation scale lengths of the magnetic field components inside ICME ejecta were 2–4 times lower than this value, indicating that magnetic field components may not be correlated at two spacecraft separated by one quarter to one half of an ejecta width. The GSE B_y magnetic field in the sheath has a larger correlation length than any other components, in the solar wind, ICME ejecta or sheath.

This may reveal processes associated with the deflection of the magnetic field away from the radial direction behind ICME-driven shocks.

Wind's high time resolution plasma and magnetic field measurements led to numerous studies of reconnection in solar wind current sheets (Gosling, 2007, 2010, 2011; Gosling, Eriksson, Phan, et al., 2007; Gosling, Phan, et al., 2007; Gosling & Szabo, 2008). Widely spaced multi-spacecraft in-situ observations revealed that the reconnection X-line in the solar wind can extend to millions of kilometers (or tens of thousands of ion inertial lengths) and persist for hours (or thousands of Alfvèn transit times). An X-line extending at least 390 Earth radii was discovered using observations from *Wind*, ACE and *Cluster* (Phan et al., 2006). Later, even more extreme events, with X-lines extending 660–1,800 Earth radii, were reported using in-situ data from *Wind*, ACE, *Geotail*, and both STEREO spacecraft (Gosling, Eriksson, Blush, et al., 2007; Lavraud et al., 2009). These observations indicate that reconnection is not intrinsically bursty and patchy. The process can operate in a large-scale and quasi-steady manner even when undriven by external flows. These discoveries involving *Wind* could not have been made in Earth's spatially limited magnetosphere, and have revealed the solar wind as a laboratory for studying the large-scale properties of reconnection.

3.7.2. Kinetic Instabilities and Waves

Perhaps the most unique advance that *Wind* provided to the field of space plasmas was its instrumentation designed to examine small-scale phenomena. For instance, *Wind* was one of the first spacecraft to fully resolve high frequency phenomena like Langmuir waves in time series electric field data (e.g., Kellogg, Monson, et al., 1996). This ability has been further leveraged by *Wind*'s longevity and redundant thermal particle measurement capabilities (i.e., 3DP, SWE, and WAVES), which have allowed researchers to examine one of the more elusive topics in plasma physics, plasma instabilities. Small-scale phenomena play a critical role in the evolution of the solar wind (e.g., see reviews by Marsch, 2006; Verscharen, Klein, & Maruca, 2019). In this section, we discuss kinetic instabilities and waves.

Some of the more heavily examined instabilities are those involving temperature anisotropies in both electrons and ions. The long baseline of observations provided by *Wind* allowed researchers to perform a series of long-term statistical evaluations of the stability of particle VDFs in the solar wind (Adrian et al., 2016; Bale et al., 2009; Chen et al., 2016; Hellinger & Trávníček, 2006; Hellinger et al., 2006; Hellinger & Trávníček, 2014; Kasper et al., 2003, 2006, 2008, 2013, 2002; Maruca et al., 2012, 2011; Maruca & Kasper, 2013). *Wind*'s results showed that the firehose, mirror, and ion cyclotron modes (see Appendix B for details) are relevant to limiting the ion temperature anisotropy in the solar wind for protons and alpha-particles. Furthermore, theories of parallel and obliquely propagating firehose instabilities could be compared, which was only possible due to the large statistics and accuracy of the data. The critical takeaway is that some of these results help explain why the ion VDFs deviate from adiabatic approximations as they propagate away from the sun.

Another free energy source of great interest is secondary beams (secondary to the core population). Note that the source of a second proton beam (in addition to the main solar wind proton beam) is still not well established. Interestingly, the presence of a differential flow between the proton and alpha-particles was found to reduce the instability thresholds for the temperature anisotropy instabilities of the Alfvèn ion cyclotron and fast/magnetosonic-whistler modes (Bourouaine et al., 2013; Verscharen et al., 2013; Wicks et al., 2016). Another study showed electromagnetic ion cyclotron waves were unstable to secondary proton beams in the solar wind (Wicks et al., 2016) suggesting ion cyclotron wave storms may be locally generated. While the influence of this secondary proton beam reduces the thresholds for the temperature anisotropy instability, others have found it also introduces a new beam instability that radiates fast/magnetosonic-whistler modes (Alterman et al., 2018; Chen et al., 2016; Gary et al., 2016).

Electron-driven instabilities are also of great interest as they help regulate the partition of energy among the multiple electron populations in the solar wind. Solar wind electrons are comprised of a cold, dense core, hot tenuous halo, and a warm, magnetic field-aligned beam streaming away from the sun called the strahl (Wilson et al., 2019a, 2019b, 2020a). Specifically, electron VDFs have been compared with electromagnetic wave observations to test theoretical instability thresholds for the whistler mode (Moullard et al., 2001; Wilson, Koval, Szabo, et al., 2013; Wilson et al., 2020a), fast/magnetosonic modes (Kellogg et al., 2011; Verscharen, Chandran, et al., 2019; Wilson et al., 2009; Wilson, Koval, Szabo, et al., 2013), electrostatic solitary modes (Bale, Kellogg, Larson, et al., 1998; Bale et al., 2002; Kellogg et al., 2011), ion acoustic modes near interplanetary (IP) shocks (Wilson, 2010; Wilson et al., 2007, 2020a), Langmuir-like modes (Ergun et al., 1998; Moullard et al., 2001; Pulupa & Bale, 2008), and electron cyclotron drift instability modes near IP shocks (Wilson, 2010; Wilson et al., 2010).

The studies mentioned above have focused on measurements of ions or electrons separately, however the stability of a plasma depends on all species simultaneously. In recent years, data from *Wind*'s multiple particle instruments have been combined to investigate the total plasma stability. Chen et al. (2016) combined data from SWE and 3DP, including all major solar wind species (protons, alphas, and electrons) to compare the stability of the solar wind to the long-wavelength firehose and mirror instabilities, for which analytical thresholds exist. For both instabilities, the dominant contribution (~2/3) was found to be from the protons, but there were also significant contributions (~1/3) from the other species. When a proton beam was present, drifts between species contributed 57% to the firehose instability. In this combined analysis, both instabilities were found to provide good constraints to the data with <1% unstable, suggesting that these long-wavelength multi-species instabilities act to provide a robust limit the evolution of the solar wind.

Klein, Alterman, et al. (2018) then used a method involving Nyquist's instability criterion to search for the presence of unstable plasma using ion (proton and alpha) data from SWE and assuming isotropic electrons. They found the majority (53.7%) of solar wind intervals to be unstable, with the vast majority of these being kinetic (no long-wavelength counterpart), with growth rates satisfying ~0–0.2 Ω_{cp}. However, the majority of growth rates were found to be slow compared to other dynamical timescales, such as the turbulence timescale, making it unclear whether these kinetic instabilities could be dynamically relevant or constrain the solar wind, and may explain why the majority of the plasma was found to be unstable.

Furthermore, examination of ~10 years of data found that $\left(T_e / T_p\right)_{tot} \gtrsim 3$ was satisfied for ~12.4% of ~446,000 intervals (Wilson et al., 2018). This temperature ratio is a threshold often used to determine the separation between strong and weak damping of ion acoustic waves. Wilson et al. (2020a) examined electron

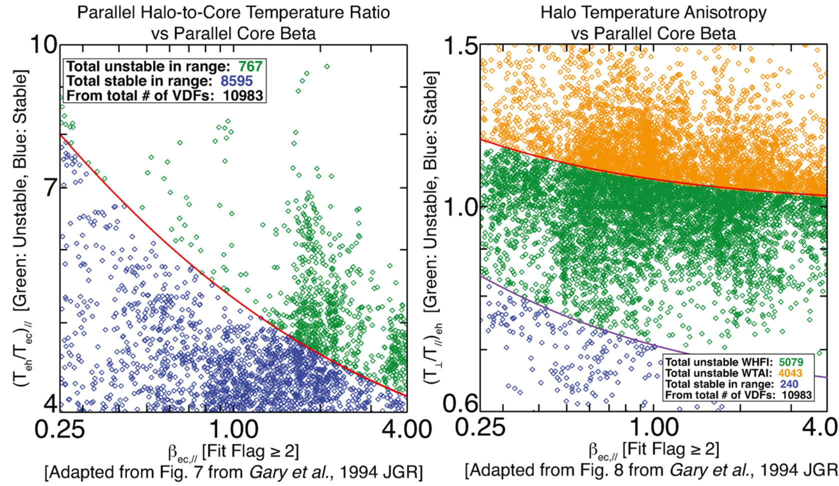

Figure 9. Adaptations of Figures 7 and 8 from Gary et al. (1994) showing the observed data from Wilson et al. (2020a). The left panel shows the parallel halo-to-core electron temperature ratios, $\left(T_{eh} / T_{ec}\right)_{\|}$, versus parallel core electron beta, $\beta_{ec,\|}$ (see Appendix A for symbol definitions) while the right panel shows halo temperature temperature anisotropy, $\left(T_{\perp} / T_{\|}\right)_{eh}$, versus $\beta_{ec,\|}$. The left panel is a proxy for heat flux instability while the right for temperature anisotropy instability. In each panel are curves indicating an instability thresholds (corresponding to maximum growth rates satisfying $\gamma_{max} > 10^{-1}\ \Omega_{cp}$), below(above) which the observed VDF is stable(unstable). Diamonds shown in green and orange are unstable while blue are stable. The green diamonds show data unstable to the whistler heat flux instability (WHFI) while the orange diamonds are unstable to the whistler temperature anisotropy instability (WTAI). This figure illustrates that most electron VDFs are unstable near IP shocks (Taken from Figure 6 in Wilson et al., 2020a). Note these data are publicly available, for example, see Table C1 in Appendix C.

VDFs near IP shocks finding only ∼3% were stable to either the whistler heat flux or whistler temperature anisotropy instabilities, as shown in the right-hand panel of Figure 9. They also found ∼28.6% of all VDFs examined satisfied $\left(T_e / T_p\right)_{tot} \gtrsim 3$ and ∼42.8% of upstream-only VDFs satisfied the same criteria, that is, conducive for ion acoustic wave growth. To compare with ambient solar wind studies, Wilson et al. (2020a) examined the rate of instability of the firehose and mirror modes finding ∼1.3% and ∼13.5% were unstable, respectively. These rates are ∼10 and ∼20 times higher than those found by Chen et al. (2016) in the ambient solar wind for the same instability criteria.

These studies are just small sample of the overall contribution *Wind* has provided to advancing our understanding of instabilities. *Wind* data have revealed that solar wind VDFs are likely strongly shaped by plasma instabilities as they propagate away from the Sun and that the amplitudes of high frequency waves can be orders of magnitude larger than previous data would suggest. These advances were only possible with *Wind*'s unique suite of instruments and the major advance in resolution they provide.

3.7.3. Turbulence

Wind has enabled significant advances in our understanding of plasma turbulence. These were made possible due to the continuous 3 s resolution plasma moments from 3DP together with magnetic field vectors at up to 22 samples per second, allowing the full inertial range to be studied with all MHD variables for the first time, and the start of the kinetic range to begin being probed in detail. These high-resolution data are supported by measurements of the ion temperature anisotropy from SWE allowing a detailed examination of the interaction of electromagnetic fields and particles as a result of turbulence. The many years of data in the free solar wind also allow the study of the dependence of the turbulence properties on important parameters, such as plasma beta and cross-helicity. In this section, we discuss *Wind*'s contribution to our understanding of plasma turbulence.

Turbulence can be described as fluctuations in properties of the plasma (e.g., density) that are chaotic in nature (Bruno & Carbone, 2013; Verscharen, Klein, & Maruca, 2019). Turbulence is an intrinsically multi-scale phenomenon where energy enters at large spatial scales and cascades to much smaller scales. Although the individual realizations cannot be predicted, the statistical properties of the energy cascade rate can be derived and in plasmas it changes at different temporal and spatial scales. Unlike in neutral fluid turbulence, turbulence in magnetized plasmas is generally anisotropic. That is, the distribution of power in wave vector ($\mathbf{k}$) space is not equal in all directions relative to $\mathbf{B}_o$, that is, $k_\perp \neq k_\parallel \neq k$. Often turbulence is examined by use of Fourier transforms in frequency or wavenumber space. In the solar wind, for instance, the magnetic fluctuation power spectrum has the form of multiple broken power-laws where each power-law corresponds to a different type of cascade. The range with the largest scales and lowest frequencies in the spacecraft frame is referred to as the injection range or outer scale. The next range is called the MHD inertial range and it extends up to slightly larger than the relevant ion scales (e.g., ion inertial length or ion thermal gyroradius). Beyond this is the kinetic range, also sometimes known as the dissipation range (Note that this term has become less relevant and been replaced by "kinetic range.") since this is where fluctuations can transfer energy to the medium through heat. For more details, see Appendix A and the Glossary for definitions.

An important achievement of *Wind* has been to establish the MHD inertial range scaling properties. Mangeney (2001) investigated the scaling of the magnetic and velocity fluctuations through conditioned structure functions, finding the velocity to have a shallower scaling, consistent with a wavenumber spectrum $k^{-3/2}$, compared to $k^{-5/3}$ for the magnetic field. This finding was confirmed by later studies (Podesta et al., 2006, 2007; Salem et al., 2009). Podesta and Borovsky (2010) showed that both Elsasser spectra (Spectra of the Elsasser variables $\mathbf{z}^{\pm}$ defined in Appendix A) scale as $k^{-5/3}$, but that the magnetic field and total (i.e., magnetic plus velocity fluctuation energies) energy spectra scale as $k^{-3/2}$ when the cross-helicity is large, which has since been confirmed by others (Boldyrev et al., 2011; Chen et al., 2013). These differences are significant since leading models of plasma turbulence predict these scalings, for example, a total energy spectrum ${k_\perp}^{-5/3}$ by Goldreich and Sridhar (1995) and ${k_\perp}^{-3/2}$ by Boldyrev (2006). Boldyrev et al. (2011); Boldyrev and Perez (2012), based on previous work by Grappin et al. (1983), proposed that the difference between magnetic and velocity fluctuation spectra is due to turbulence-generated residual energy, which is predicted to scale as ${k_\perp}^{-2}$ and this steep scaling was confirmed by Chen et al. (2013). The large dataset

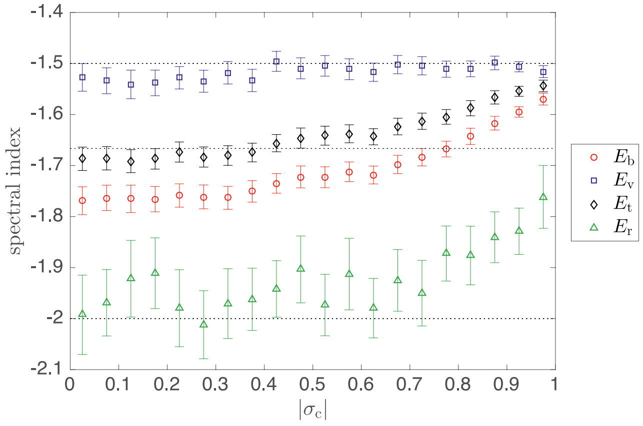

Figure 10. Variation of the wavenumber power spectral indices of magnetic field (E_b), velocity velocity (E_v), total ($E_t = E_b + E_v$), and residual energy residual energy ($E_r = E_v - E_b$) with the level of imbalance $|\sigma_c\sigma_c|$. Note that $|\sigma_c| \approx 0$ corresponds to balanced turbulence and $|\sigma_c| \approx 1$ to highly imbalanced turbulence (Adapted from Figure 4 in Chen, 2016).

provided by *Wind* allows conditional statistics to be used to separate solar wind with different properties and this has allowed the measurement of the impact of cross helicity and residual energy on the turbulent cascade to be measured simultaneously (Bowen et al., 2018; Bruno et al., 2007; Wicks, Mallet, et al. 2013; following Bavassano et al., 1998). The current state of knowledge is summarized in Figure 10 which shows the inertial range spectral indices of the MHD fields as functions of cross-helicity, $|\sigma_c|$, which is a quantitative measure of imbalance – the different fluxes of turbulent fluctuations propagating toward or away from the sun. While not every aspect of this figure is explained (notably the cross-helicity dependence of the total energy spectrum), we are tantalizingly close to understand the physics that governs the spectral properties of the MHD turbulence cascade, and *Wind* has played a dominant role in enabling this.

Wind has also allowed us to measure the anisotropy of the turbulence to further determine the physics of the cascade. Wicks et al. (2011) used a wavelet technique (based on Horbury et al., 2008) to measure the spectrum of the Alfvénic turbulence variables with respect to the local mean field direction. Deep in the inertial range, all fields were shown to be anisotropic, $k_\perp \gg k_\parallel$, with velocity, magnetic, and the dominant Elsasser field having $k_\parallel^{-2}$ scaling parallel to the local mean field. This $k_\parallel^{-2}$ spectrum is one the key predictions of critical balance, the conjecture at the heart of modern turbulence theories, implying that the turbulence becomes increasingly anisotropic toward smaller scales. Verdini et al. (2018) took this further by using a structure function technique (based on Chen et al., 2012) to measure the 3D anisotropy of the turbulent eddies, concluding that under conditions of weak solar wind expansion the turbulence spectrum is different in all three directions resulting in "ribbon" rather than "tube" shaped eddies at small scales, consistent with the Boldyrev (2006) picture. Verdini et al. (2019) then showed that this is also true for the velocity fluctuations, although they maintain overall their shallower scaling compared to the magnetic fluctuations. Figure 11 shows an example of the 3D magnetic eddy shapes measured by *Wind*.

While the dominant fluctuation power in the solar wind is in the Alfvénic fluctuations, there is also a subdominant compressive component to the turbulence, which presents some interesting, but quite different physics. While it has long been known that the solar wind compressive components are broadly pressure-balanced, Howes et al. (2012) and Klein et al. (2012) performed a statistical analysis on the density and magnetic field strength correlation as a function of plasma β using 10 years of *Wind* data. They concluded a compressive component is consistent with being almost entirely in the kinetic slow mode, implying very little or no transfer of energy to whistler turbulence at smaller scales. Later, Verscharen et al. (2017) compared a larger variety of compressive quantities to linear predictions for both kinetic and MHD slow modes, finding the MHD polarizations to be a good match. This unexpected (It was not expected that MHD

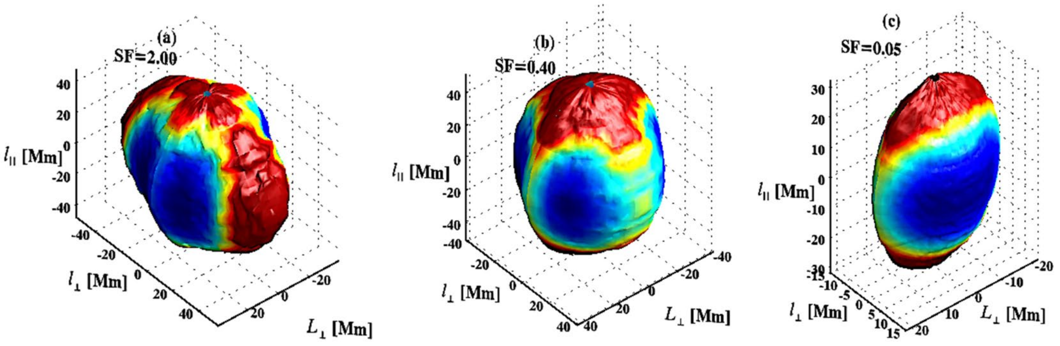

Figure 11. Statistical 3D eddy shapes of magnetic fluctuations at three different scales in the inertial range, from large scales (left) to small scales (right), for the case of weak expansion. Colors represent distance from the origin (Adapted from Figure 11 in Verdini et al., 2018).

would do so well at predicting the polarizations since the solar wind is a weakly collisional plasma.) raises interesting possibilities about what may be causing such fluid-like behavior in the weakly collisional solar wind, with possibilities including wave-particle scattering and anti-phase-mixing; both topics have much broader implications for weakly collisional plasma physics in general.

It is well-known that plasma turbulence is not a completely random process but generates correlated intermittent structures (e.g., Bruno & Carbone, 2013; Salem et al., 2009). However, an open question in solar wind physics is exactly how much of the structure in the solar wind is generated in situ by turbulence versus remnant structure from processes at the Sun (Borovsky, 2008; Owens et al., 2010). One view is that large angle magnetic field rotations represent flux tubes or other structures from the Sun, while the turbulence is responsible for the small-amplitude fluctuations of these structures. However, Zhdankin et al. (2012) presented an analysis to suggest that turbulence can account for the full distribution of angle rotations, large and small. They compared 5 years of *Wind* observations to an MHD turbulence simulation to show a very good match for this distribution, concluding that the majority of solar wind discontinuities arise as intermittent structures from the turbulent cascade. Osman et al. (2012) investigated these structures further, finding the plasma near the discontinuities to be hotter and the temperature more anisotropic and often marginal to the mirror and firehose instabilities, suggesting a link between the structures, turbulent heating and kinetic instabilities. Although the debate on the nature of the structures continues, these results from *Wind* have changed the way we view solar wind structure.

At the large-scale end of the cascade, the correlation length of turbulence is linked to the energy containing scales that feed the cascade. When measuring such large-scale fluctuations in the solar wind, one significant problem is that plasma travels quickly over the spacecraft, meaning that at long timescales the stream structure dominates the signature, rather than the low-frequency fluctuations that might be present within streams. The extensive *Wind* dataset allowed Bruno et al. (2019) to measure the low-frequency spectrum within extended intervals of slow solar wind, showing for the first time that slow solar wind, like the fast wind, is also able to support a “1/f” range, in addition to this well-known result in fast wind. Long time series of fast wind data from *Wind* were also used by Wicks, Roberts, et al. (2013) to show that the scale at which the 1/f range transitions to the inertial range of turbulence depends on the correlation properties of the fluctuations at the spectral break. Intervals with less aligned velocity and magnetic field fluctuations become turbulent at larger scales, even within a single stream. The realization of this property of turbulence is significant since it indicates that the turbulence spectrum may extend to larger scales than previously thought.

Data from *Wind* MFI and SWE have been used in combination with data from other spacecraft to achieve multi-point measurements of the turbulence in the solar wind. Such a multi-point analysis allows the study of the space-time structure of the turbulent fluctuations without having to rely on Taylor’s frozen-in hypothesis, which is usually employed in single-point measurements (Verscharen, Klein, & Maruca, 2019). By combining plasma and magnetic-field data from IMP-8 and *Wind*, Richardson and Paularena (2001) calculated multiple correlation coefficients for solar wind turbulence. The scale sizes for changes in the magnetic-field components perpendicular to the flow direction were found to be about 0.002 AU, while the plasma velocity and density scale lengths were found to be larger by a factor of more than two. The same study found a radial scale length of order 0.017 AU. These results were supported by a later study using the amplitude ratio, coherence, and phase lag of field and plasma measurements from *Wind* and ACE (Matsui et al., 2002), although the radial scale was somewhat smaller than in the earlier estimate.

The combination of magnetic-field data from *Wind* with quasi-simultaneous measurements from ACE and *Cluster* facilitated the determination of the Eulerian correlation scale and the Taylor microscale in the solar-wind plasma frame near Earth (Matthaeus et al., 2005). This multi-spacecraft comparison gives an estimate for the omni-directional correlation length of 0.0082 AU. The combination of this result with *Cluster*’s simultaneous measurement of the Taylor microscale of 1.6×10^{-5} AU provides an estimate for the effective Reynolds number of about 230,000 in the measured solar-wind interval. The same method also reveals a Eulerian decorrelation time of about 2.9 h in the solar wind near one AU (Matthaeus et al., 2010). Later combinations of ACE, *Geotail*, and IMP-8 data with *Wind* data refined this picture, finding slightly smaller correlation lengths and different correlation lengths in fast and slow solar-wind streams (Matthaeus et al., 2016; Wicks et al., 2009, 2010). *Wind* also supported other turbulence studies through, for example, cross-calibrations with ACE measurements for the OMNI datasets (King & Papitashvili, 2005) or as a source of magnetic-field measurements for spacecraft without a working magnetometer (Pitňa et al., 2019; Šafránková et al., 2019).

Leamon et al. (1998) attempted to distinguish between wave and turbulence paradigms at the dissipation scale using *Wind* MFI solar wind data. The authors observed steepening of the magnetic field spectrum at ∼1 Hz with an associated increase in compressibility and nonzero magnetic helicity. Furthermore, the turbulence was measured to be significantly oblique, interpreted as a combination of kinetic Alfvén waves and 2D ($k_{\|} = 0$) modes. A reinterpretation of these results has contributed to our current understanding of a critically balanced dispersive cascade of kinetic Alfvén turbulence (with some damping at ion and electron scales).

Another way to understand the processes occurring in the kinetic range is to investigate the scale at which the spectral break occurs. Leamon et al. (2000) compared the measured power spectral break point—the frequency or wavenumber where the power spectral density power-law profile changes exponent—to the cyclotron frequency, parallel resonant wavenumber, and inertial scale, finding the latter to have the best correlation, and suggested this could be related to current sheets of the break point thickness. Bruno and Trenchi (2014) used *Wind* in combination with MESSENGER and *Ulysses* observations to show that the break point evolves linearly with distance from the Sun, similarly to the ion gyroscale, inertial length, and cyclotron resonance scale. The authors concluded that the scale of cyclotron resonance controls the linear evolution. The difficulty, however, in distinguishing these scales (and therefore processes) is that at $\beta \sim 1$ they are essentially the same, so Chen et al. (2014) examined intervals of very high and low β, showing the break point to be at the gyroscale at high β and inertial scale at low β. Woodham et al. (2018) came to a similar conclusion using the large *Wind* data archive and examining the full range of β. The high β result matches expectations for a transition to dispersive kinetic Alfvén turbulence, but a fully consistent explanation for the low β result has yet to be identified and remains an open question. Boldyrev et al. (2015) suggested that the result could be explained by a significant field-parallel wavenumber component at low β. Vech et al. (2018) used *Wind* data at low electron β to suggest the break to be related to the disruption scale at which reconnection could dominate the cascade dynamics. We still have much to learn about kinetic range turbulence, but *Wind*'s early pioneering results have certainly given key valuable insights.

The early Leamon et al. (1998) results were followed up by statistical studies of the high-frequency magnetic field data, identifying key features of coherent waves with distinct left-handed and right-handed rotations (Markovskii et al., 2015). Woodham et al. (2019) linked these helical waves to the SWE proton temperature anisotropy data and showed that field-parallel propagating modes at the spectral break scale are dominated by ion cyclotron waves driven by temperature anisotropy and proton and alpha particle beams (Wicks et al., 2016) but the background of oblique modes are kinetic Alfvén waves with no particular dependence on proton temperature anisotropy. These statistical studies, only possible with *Wind*, demonstrate the link between particle temperature and the inertial range energy cascade, and provide the current best knowledge of energy transfer in turbulent space plasmas.

These are just a selection of results that *Wind* has enabled in solar wind turbulence, but they illustrate the diverse aspects of the physics that have been revealed. Hopefully *Wind* will continue contributing to our understanding of this important and widespread plasma process over the coming years, in particular in combination with new missions such as *Parker Solar Probe* and *Solar Orbiter*, where the multi-point measurements will likely prove to be invaluable (e.g., Velli et al., 2020).

3.7.4. Long-Term Solar Wind Studies

Wind's longevity has been a major advantage for long-term statistical studies of solar wind physics. Combined with the most accurate solar wind plasma measurements of any near-Earth spacecraft, *Wind* observations have helped researchers uncover subtle collisional effects, the first statistically significant estimate of the electron-to-ion temperature ratio, $\left(T_e / T_s\right)_{tot}$ ($s = p$ for protons, α for alpha-particles), and novel relationships between the alpha-to-proton abundance ratio and parameters such as the solar wind speed and sunspot number. In this section, we hightlight some of these results.

Table 6
Long-Term Solar Wind Statistics

Parameter	$X_{25\%}$[a]	$X_{75\%}$	$\tilde{X}$[b]
Densities			
n_e [cm^{-3}]	5.71	13.0	8.57
n_p [cm^{-3}]	5.05	11.7	7.61
n_α [cm^{-3}]	0.13	0.32	0.21
Temperatures and Thermal Speeds			
$T_{e,tot}$ [eV]	9.41	13.1	11.1
$T_{p,tot}$ [eV]	4.80	15.1	8.45
$T_{\alpha,tot}$ [eV]	5.43	34.0	12.2
$V_{Te,tot}$ [km/s]	1,579	2,411	1,975
$V_{Tp,tot}$ [km/s]	21.9	76.9	40.2
$\left(T_e / T_p\right)_{tot}$	0.78	2.14	1.28
$\left(T_e / T_\alpha\right)_{tot}$	0.32	1.78	0.82
$\left(T_\alpha / T_p\right)_{tot}$	1.39	3.62	2.01
Plasma Betas			
$\beta_{e,tot}$	0.83	2.64	1.45
$\beta_{p,tot}$	0.67	1.90	1.16
$\beta_{\alpha,tot}$	0.02	0.19	0.07
Frequencies and Lengths			
f_{cp} [Hz]	0.04	0.22	0.09
f_{ce} [Hz]	80.2	409	162
f_{pp} [Hz]	371	944	578
f_{pe} [kHz]	17.2	42.5	26.3
ρ_{ce} [km]	1.03	4.62	2.28
ρ_{cp} [km]	32.5	186	88.8
λ_e [km]	1.12	2.77	1.82
λ_p [km]	50.5	129	82.5
λ_{De} [m]	4.74	13.8	8.58

[a] $X_{y\%}$ is the yth percentile. [b] $\tilde{X}$ is the median.

Surprisingly, the first long-term statistical study of $\left(T_e / T_s\right)_{tot}$ was $\left(T_e / T_s\right)_{tot}$ was only recently performed using *Wind* observations (Wilson et al., 2018). The study used ~10 years of solar wind data, from January 1995 to December 2004, publicly available at SPDF CDAWeb. A summary of the results for all solar wind conditions from Wilson et al. (2018) are shown in Table 6. See Appendix A for further symbol definitions.

Wilson et al. (2018) showed, however, that not only is the solar wind plasma not in thermodynamic equilibrium, the plasma is not in thermal equilibrium either. Note that the work by Wilson et al. (2018) was not the first to show the solar wind is out of equilibrium. It is referenced here as it's recent, it's a *Wind*-based study, and it shows the largest statistically significant dataset that includes electron velocity moments. The authors illustrated that because the particle-particle Coulomb collision rates are so low in the IP medium, an interaction with just one small-amplitude wave packet can cause a greater effect than the cumulative effect of collisions between the sun and Earth. This begs the question of why we actually see any evidence of particle-particle collisions in the solar wind (e.g., see results in Adrian et al., 2016; Bale et al., 2013; Horaites et al., 2015, 2019; Kasper et al., 2017; Maruca et al., 2013; Salem et al., 2003; Wilson et al., 2018, 2019a) since we consistently observe, directly or indirectly, numerous different types of electromagnetic fluctuations in the solar wind (Agapitov et al., 2020; Bale et al., 2009; He, Wang, et al., 2015; He, Pei, et al., 2015; He et al., 2019; Kasper et al., 2013; Malaspina et al., 2020; Maruca et al., 2012; Vasko et al., 2020; Wicks et al., 2016). That is, the ubiquitous electromagnetic waves should wash out any particle-particle collision signatures much faster than particle-particle collisions can relax the distributions. Note that the result of wave-particle interactions is not to reduce a particle distribution to an isotropic Maxwellian. Rather, wave-particle interactions tend to produce power-laws or plateaus and sometimes even introduce anisotropies (e.g., see discussion in Wilson et al., 2020a, and references therein for more details). So there are clear differences between the effect of waves versus particle-particle collisions on the particle distribution functions. The observation of collisional effects despite their weak/slow influence on the particle distributions compared to other effects (e.g., waves and/or turbulence) remains an outstanding question.

In contrast researchers have found evidence of a preferential ion heating source in the solar corona and even placed limits on the heliocentric distance below which this heating occurs (Kasper et al., 2017; Kasper & Klein, 2019), a result only found due to the large statistics available from *Wind* data sets. That is, the ions appear to be heated below some altitude near the sun and then negligible changes occur as the particles propagate to Earth. The conflict between the preferential coronal ion heating observations and the expected plasma evolution due to interactions with ubiquitous waves between the Sun and Earth still remains an unanswered and fundamentally critical question in studies of the solar wind.

Finally, *Wind* studies of the relative abundance between protons and alpha-particles have shown solar cycle and other effects (Alterman et al., 2018; Alterman & Kasper, 2019; Kasper et al., 2007, 2012). The authors showed that the alpha-particle-to-proton abundance varies with solar cycle and is a function of solar wind speed (Alterman & Kasper, 2019; Kasper et al., 2007, 2012). That is, higher speed solar wind has a higher alpha-particle abundance than slower wind and the abundances peak near solar maximum. In fact, when binned by solar wind speed, Kasper et al. (2007) showed a consistent six month periodicity in the alpha-particle abundance, due to the heliographic latitudinal changes as the spacecraft orbits the Sun. Later, Alterman and Kasper (2019) showed that there is a phase delay between the rise in sunspot numbers and the rise in alpha-particle abundance, which turns out to be a monotonic function of the solar wind speed. The authors found that changes in the sunspot number precede changes in alpha-particle abundance with the smallest lag time, ~150 days, corresponding to the lowest solar wind speed. The alpha-particle abundance was assumed to be modified in the photosphere only but the speed-dependent lag in the alpha-particle abundance in response to changes in SSN suggests other processes at higher altitudes are important. This work has yielded new clues about the source of the slow solar wind, a long-standing problem in solar wind physics.

The above contributions to our understanding of the solar wind almost entirely rely upon the longevity and accuracy of *Wind* measurements. That is, the use of data from a single spacecraft removes the uncertainties introduced when cross-calibrating between different sets of instrumentation from different spacecraft. Given that many of these nuanced results are relatively small in magnitude and/or difficult to measure, it is unlikely many could have been obtained using multiple missions over similar periods of time.

3.8. Transient Large-Scale Magnetic Phenomena

The *Wind* mission has provided numerous opportunities to identify, characterize, and model IP transients such as corotating interaction regions (CIRs), stream interaction regions (SIRs), IP shock waves, and ICMEs. This section summarizes the results of investigations that have improved our understanding of these structures and their importance for Sun-Earth connections. This section is broken up into the following three subsections: Section 3.8.1 highlights advances made on IP shocks, Section 3.8.2 discusses *Wind*'s pivotal role in our understanding of ICMEs, and Section 3.8.3 discusses advances in our understanding of SIRs/CIRs.

3.8.1. Interplanetary Shock Waves

One of the most important astrophysical phenomena for particle energization and space weather impacts are collisionless shock waves. *Wind* has made several critical contributions to our understanding of collisionless shock waves including, but not limited to, improved understanding of energy dissipation mechanisms, particle energization processes and sources, the structure of shocks, and remote sensing of shocks. In this section we briefly highlight a few of these advances while pointing the reader to other sections where the remaining topics are discussed. This section focuses on IP shocks but a few important contributions from measurements at the terrestrial bow shock are discussed as well.

In the IPM, shocks are mainly caused by ICMEs (see Section 3.8.2) and planetary bow shocks. When ICMEs reach a supersonic velocity as they propagate and expand through the IPM (Lepping et al., 2007; Lepping, Wu, Berdichevsky & Ferguson, 2008; Vandas et al., 2009) a shock can form on their leading (anti-sunward) edge. IP shocks can also be generated by interaction regions between slow and high speed solar streams (G. Mann et al., 2002; Mason et al., 2009), often referred to as CIRs, or stream interaction regions or SIRs (see Section 3.8.3). Although we know what forms collisionless shocks, the energy dissipation mechanism(s) that govern shock dynamics in astrophysical plasmas are still not well understood.

As previously discussed in Section 3.6, in relation to the terrestrial ion foreshock, there are numerous unknowns on the topic of shock particle energization by collisionless shocks. *Wind* studies led to some of the first pieces of evidence to illuminate how, for example, field-aligned ion beams can be generated at the quasi-perpendicular bow shock (e.g., Meziane et al., 1997; Meziane et al., 1999, 2002, 2003, 2011). A tangential study discovered that a type of TIFP could generate similar field-aligned ion beams, but the generation was occurring locally in the ion foreshock not at the quasi-perpendicular bow shock (e.g., Wilson, Koval, Sibeck, et al., 2013, and discussed in Section 3.6). This spawned a whole new field of study and helped lead to the serendipitous discovery that the same types of TIFP could also locally generate relativistic electrons (e.g., Wilson et al., 2016, and discussed in Section 3.6). Multispacecraft studies including *Wind* have even confirmed the long-theorized concept of shock-shock acceleration between the terrestrial bow shock and an IP shock (though this was not surprising) (e.g., Hietala et al., 2011, 2012). Thus, *Wind*'s unique compliment of instrumentation has led to several critical contributions to our understanding of shock acceleration.

Early *Wind* observations illustrated evidence of numerous kinetic instabilities located in and around collisionless shocks (e.g., Bale et al., 1997; Bale, Kellogg, Larson, et al., 1998; Bale, Kellogg, Goetz, & Monson, 1998; Kellogg, Monson, et al., 1996; Kellogg et al., 1999). The waves radiated by these instabilities have long been theorized to dissipate energy in collisionless shock waves (e.g., see Sagdeev, 1966). Therefore, Wilson et al. (2007) examined electrostatic waves around 67 IP shocks finding that the wave amplitudes increased with increasing Mach number and strength. The positive correlation is evidence that as the shock gets stronger, it requires larger amplitude waves to dissipate more energy. A follow-on case study examined a high Mach number shock presenting the first observations of electron Bernstein-like modes identified as having been radiated by the electron cyclotron drift instability or ECDI (Wilson, 2010). The importance of the identification is that the ECDI results from the free energy between incident electrons and shock-reflected ions, that is, the wave couples to both ions and electrons and illustrates a connection between particle reflection and wave generation. Later work (Wilson et al., 2012) led to the observation of large amplitude magnetosonic-whistler precursors (see Appendix B for definition and properties) upstream of shocks that could not have generated said waves through dispersive radiation—waves emanating from a time- and spatially varying current structure with a frequency depending upon the wave number (Tidman & Northrop, 1968). It was determined that the precursors were likely radiated by a modified two-stream instability due to free energy similar to what drives the ECDI. Furthermore, the waves were shown to be stochastically accelerating the electrons parallel and ions perpendicular to the quasi-static magnetic field. The same mechanism has since been proposed as a possible source mechanism for the relativistic electrons discussed above (e.g., see Roberg-Clark et al., 2018). Thus, *Wind*'s kinetic-physics-based instrumentation has helped greatly advance our understanding of instability-based energy dissipation mechanisms in collisionless shocks.

More recently a *Wind*-based study examined the structure of low Mach number, low plasma beta, quasi-perpendicular shocks (Wilson et al., 2017). The work was motivated by discussions in the literature that argued such shocks should be laminar in their magnetic field profiles, thus the particle trajectories through the shock should be well behaved (e.g., see review by Mellott, 1985). Interestingly, with the high cadence *Wind* magnetometer data it was found that not only are these low Mach number, low plasma beta, quasi-perpendicular shocks filled with magnetosonic-whistler precursors, the precursor amplitudes were, on average, ~220% of the change in magnetic field magnitude across the shock. That is, the precursors contained the largest magnetic field gradients in the shock transition, not the shock ramp. Note that unlike the Wilson et al. (2012) study, these shocks are too low in Mach number to reflect sufficient ions to generate the modified two-stream instability or ECDI. Thus, the waves are likely generated through dispersive radiation. The critical point is, however, that such large amplitude waves clearly affect the incident ion and electron trajectories as recently illustrated using the Magnetospheric Multiscale (MMS) spacecraft (e.g., Chen et al., 2018; Hull et al., 2020; Oka et al., 2019). Thus, *Wind* has also advanced our understanding of collisionless shock structure.

There are several other IP shock-related advances led by *Wind* studies that will not be discussed here as they are discussed elsewhere in this review. Some of these include radio emissions such as type II solar radio bursts (e.g., Bale et al., 1999; Pulupa & Bale, 2008, and discussed in Section 3.10), acceleration and transport of solar energetic particles events (SEPs) (e.g., Reames, 2017, and discussed in Section 3.9), and the nonplanar structure of IP shock fronts (e.g., Neugebauer & Giacalone, 2005, and discussed in Section 3.7.1).

Below we discuss *Wind*'s contribution to understanding the phenomena associated with ICMEs and CIRs.

3.8.2. Interplanetary Coronal Mass Ejections

Interplanetary coronal mass ejections (ICMEs) are the manifestations in the solar wind of CMEs at the Sun and are the major solar wind drivers of space weather. In particular, around 90% of major geomagnetic storms (Dst ≤ -100 nT) occur when ICMEs encounter Earth (Zhang et al., 2007), and especially severe storms driven by ICMEs, such as the March 1989 storm that caused a blackout of the Quebec power grid, and the 1859 "Carrington" event (Carrington, 1859; Siscoe et al., 2006), can lead to significant societal and economic impact (Oughton et al., 2017; Riley et al., 2018). On the other hand, most ICMEs produce only modest geomagnetic effects (e.g., Richardson & Cane, 2010). A leading driver of enhanced geomagnetic activity is the presence of strong, sustained southward-directed magnetic fields, and these are frequently found in a subset of ICMEs termed "magnetic clouds" (MCs) (Burlaga et al., 1981) characterized by an enhanced, slowly rotating, flux-rope-like magnetic field; southward fields in the ICME sheath can also contribute (Kilpua, Balogh, et al., 2017). Particles accelerated at ICME-driven shocks also contribute to solar energetic particle events (e.g., Reames, 2012). Although ICMEs and their characteristic signatures (e.g., Zurbuchen & Richardson, 2006) were largely discovered in early in-situ observations (often being referred to as "shock drivers", "pistons," and "ejecta"), *Wind* has made significant contributions to the study of ICMEs and MCs (e.g., Hidalgo & Nieves-Chinchilla, 2012; Lepping, Wu, Berdichevsky & Szabo, 2018) and their space weather effects.

Wind launched roughly two years before the SoHO spacecraft that carries the LASCO coronagraphs, which makes near-continuous observations of the corona and CMEs. The combination of *Wind* in situ measurements from MFI, SMS, 3DP, and SWE, SoHO LASCO CME observations and and extreme ultraviolet observations from EIT Yokhoh X-ray observations (e.g., Berdichevsky et al., 2002) resulted in the confirmation of the connection between CMEs in the corona and MCs subsequently observed near-Earth (e.g., see Webb, 1998; ; Webb et al., 1998; Webb et al., 2000). Previous studies had associated the arrival of a magnetic cloud with the disappearance or eruption of a prominence at the Sun a few days earlier (Webb, 1988; Wilson & Hildner, 1984), while the orientation of the MC had been found to match well with the orientation of the prominence in many cases (Bothmer & Schwenn, 1994). The discovery of cold prominence material in a small fraction of a magnetic cloud at Earth (Larson et al., 2000) indicates that prominence and magnetic cloud are not a one-to-one equivalent. Combining coronagraphic observations with SoHO and statistical surveys showing that the typical radial size of a MC is 0.21 AU (e.g., Lepping et al., 2006) enabled the discovery that MCs are associated with the dark cavity of the three-part CME structure (Illing & Hundhausen, 1985) observed remotely in the corona.

Another important contribution to understanding the origin of ICMEs is the observation of enhanced solar wind $^3\mathrm{He}^{2+}$ within ICMEs. Ho et al. (2000) identified six enhanced $^3\mathrm{He}^{2+}/^4\mathrm{He}^{2+}$ periods from January 1995 to May 1998, using data from the MASS high resolution solar wind spectrometer on *Wind*. The ratios observed in these events were four to 10 times higher than previously reported average solar wind values. It was suggested that these enhancements originated in the prominence core embedded within the CME. In a separate event, *Wind*/MASS high-mass resolution measurements of helium ions, including their number density, velocity and temperature, revealed the presence of $^4\mathrm{He}^+$ ions, and SWICS observed unusually low charge states of O^{5+} and Fe^{5+}, during a short interval within an MC apparently composed of cold prominence material (Burlaga et al., 1998).

The 3DP instrument's ability to measure thermal, suprathermal and energetic electrons allowed *Wind* to provide some of the first measurements of extremely cold (temperature down to below 1 eV) electrons inside MCs (Larson et al., 2000). Because *Wind* is a spinning platform, careful analysis of the spacecraft potential with similar measurements of proton temperatures allowed Larson et al. (2000) to presented the first experimental observation of collisionally coupled electrons and protons in interplanetary space.

To probe the internal structure of MCs, Shodhan et al. (2000) used observations of suprathermal electrons from *Wind* and several other spacecraft to assess the fraction of time when bidirectional versus unidirectional electron strahl flows were present during the passage of MCs. This classification indicates the presence of looped field lines rooted at the Sun at both ends versus open field lines, respectively. The fraction of bidirectional flows was found to vary widely from no bidirectional streaming to ∼100%, with the largest MCs being the most closed. The different flows were also distributed randomly within the MCs. These results suggest that although MCs are large-scale coherent structures, reconnection, either near the Sun or with the IMF, sporadically alters the field topology from closed to open. A separate analysis technique was also used to investigate the open/closed field line nature of MCs. By measuring the arrival time and velocity dispersion of suprathermal and energetic electrons (100 eV–100 keV) associated with a series of impulsive solar flares that fortuitously were injected into the footpoints of a MC as it passed over *Wind* in October 1995, Larson et al. (1997) estimated the path lengths traveled by these electrons at different locations within the MC. These were overall found to be consistent with a low-twist core and a more highly twisted outer shell, as expected for a flux rope configuration as shown in Figure 12. On the other hand, Kahler et al. (2011) applied a similar method to eight MCs and found a poor correlation between the inferred electron path lengths and those expected from MC field models, with the exception of the event studied by Larson et al. (1997). Note that the fitting discussed here refers to the model path length in Figure 12d and not to the magnetic field magnitude in panel a which is evidently a poorer fit to the observed field magnitude. We note that a critique of the magnetic field magnitude fit is not appropriate here as we are reporting the main findings of this work.

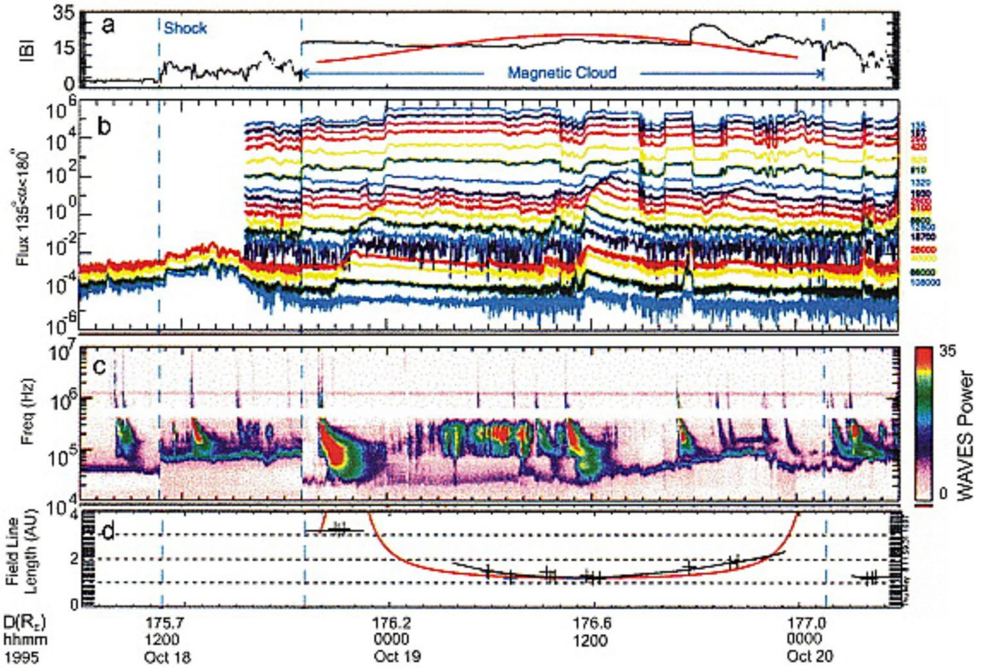

Figure 12. Analysis of the length of magnetic field lines inside an MC measured by *Wind* for the October 18–20, 1995 ICME (Larson et al., 1997). The figure is taken from Kahler et al. (2011), which was adapted from the Larson et al. (1997) study. The panels show from top to bottom, the magnetic field strength with results from the force-free model in red (a), the flux of suprathermal electrons for various energies between 135 eV and 100 keV propagating anti-parallel to the magnetic field from 3DP (b), the wave power of solar radio emissions observed by WAVES (c) including multiple type III bursts, some associated with the electron injections in (b), and the derived field line length in AU for each of these bursts with the modeled length from the force-free model of panel (a) in red (d).

Fitting and reconstruction techniques are needed to determine the global structure of ICMEs and MCs from single-spacecraft crossings. In the best cases, MCs are well-ordered (single flux ropes) and they can be readily modeled by a variety of techniques. Although spheromak-like plasmoid models have been proposed for MCs (Vandas et al., 1993), work has focused on flux rope models of various levels of sophistication (Burlaga, 1988; Farrugia et al., 1993; Hidalgo et al., 2002; Lepping et al., 1990; Marubashi, 1986). Frequently, MC are reconstructed by neglecting expansion or cross-section distortion. In particular, Lepping et al. (1990) developed the most commonly used in situ reconstruction technique in which the magnetic structure is assumed to be a static, axially symmetric cylinder that can be approximated by a linear force-free magnetic configuration (Burlaga, 1988; Lundquist, 1951). Following the same geometrical assumptions, but relaxing the force-free requirement, Hidalgo et al. (2000) derived a family of models that attempt to reproduce the varying physical and geometrical characteristics of MCs found in in situ data (Hidalgo et al., 2002; Hidalgo & Nieves-Chinchilla, 2012; Nieves-Chinchilla et al., 2012, 2016). However, it is not yet clear whether any one of these models is sufficiently realistic to describe the observed variety of MC signatures. *Wind* measurements of the magnetic field and plasma pressure have resulted in the development of MC analysis techniques that go beyond force-free approximations to extend to magneto-hydrostatic equilibrium through the Grad-Shafranov technique (e.g., Hu & Sonnerup, 2001). This was first applied to *Wind* measurements of magnetic clouds by Hu and Sonnerup (2002) and has been used extensively since. However, recent comparisons of various fitting and reconstruction models, both for general (Al-Haddad et al., 2013) and simple ICMEs (Al-Haddad et al., 2018), have highlighted that different techniques do not return consistent results for the ICME orientation. While this result may appear pessimistic, we emphasize a couple of positive consequences: (a) with the large number of reliable and complete measurements of MCs and ICMEs over 25 years by *Wind*, fitting and reconstruction models have been developed and improved to better integrate physics, that is, moving away from a constant-alpha force-free circular cross-section model, (b) comparative studies have highlighted that work using a single fitting or reconstruction technique may lead to unreliable

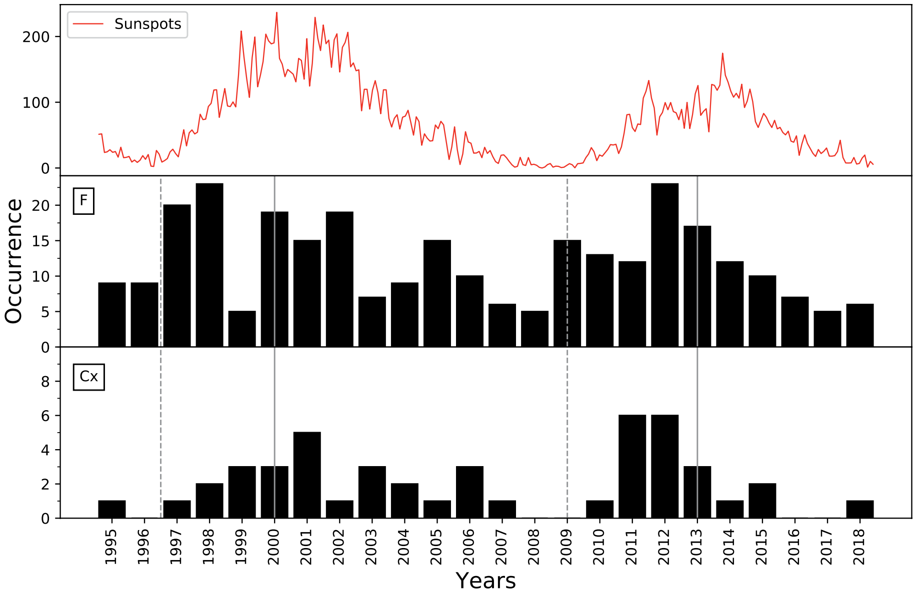

Figure 13. Occurrence of magnetic ejecta (e.g., MCs) per year near 1 AU as compared to sunspot number. Top panel: sunspot number showing the weaker solar maximum in 2012–2014 as compared to 2000–2002. Middle and bottom panels: number of flux-rope like ICME (F, middle) and complex ICMEs (Cx, bottom) from *Wind*.

results when comparing MC orientation with the orientation of the related prominence and flux rope at the Sun.

Gopalswamy, Yashiro, et al. (2015) and Nieves-Chinchilla et al. (2018) used *Wind* data to elucidate properties of MCs during solar cycles 23 and 24 (e.g., see Table C1 in Appendix C). Of particular importance is the relation between ICMEs or MCs measured at L1 and the solar activity, which was weaker in cycle 24 than cycle 23 with an extended deep minimum in 2007–2009. Although the average sunspot number declined by ~40% between solar cycles 23 and 24, there was no decline in the number of MCs in cycle 24 compared with cycle 23 (see Figure 13). However, of the intense geomagnetic storms (Dst < −100 nT), ~80% were associated with ICMEs and the majority associated with MCs was significantly lower in solar cycle 24 as compared to solar cycle 23 (Gopalswamy et al., 2020; Jian et al., 2018; Shen et al., 2017). Some of this reduction in geo-effectiveness in cycle 24 as compared to cycle 23 may be related to the 22-years cycle in bipolar MCs (Li et al., 2018) and also associated with the weaker magnetic fields inside MCs, and the shorter MC duration, during solar cycle 24 (Lepping et al., 2011). Wood et al. (2017) used *Wind* in situ observations of MCs in conjunction with observations from the coronagraphs and Heliospheric Imagers on the STEREO spacecraft to track 31 MCs from the Sun to near 1 AU and compare the properties of the MCs with the associated erupting flux ropes at the Sun. They found that the flux rope orientations and sizes inferred from imaging near the Sun were not well correlated with those of the in situ MCs. This has significant implications for attempts to predict MC magnetic fields and their geoeffectiveness from observations of the solar source regions (e.g., Savani et al., 2015). However, the arrival times at 1 AU were well predicted.

Estimates in the literature of the fraction of ICMEs that include MCs vary from ~15% to 80% (Bothmer & Schwenn, 1996; Gosling et al., 1990; Marubashi, 2000; Mulligan et al., 1999; Richardson & Cane, 2004). Long-term statistical studies including observations during the *Wind* mission make it possible to reconcile these various studies by recognizing that the fraction of MCs varies with with the solar cycle (Lepping, Wu, Berdichevsky, & Kay, 2018; Lepping et al., 2020; Richardson & Cane, 2004).

The several hundred ICMEs measured by Wind also allow the characteristics that distinguish MCs from those with more complex magnetic structures to be better defined (Nieves-Chinchilla et al., 2018). Non-MC-like configurations may arise in several circumstances: the ICME may result from the interaction of several individual ICMEs on their way to Earth (Burlaga et al., 2002; Lugaz et al., 2007), or if the magnetic field configuration of the original CME was more complex than a simple flux rope. For example, a MC may be a substructure of a more extended ICME region (Richardson & Cane, 2010) and not encounter the observing spacecraft. The absence of the flux rope signatures can be explained by the spacecraft encountering the MC far from the center axis or in the flux rope leg. Magnetic flux erosion by reconnection at the front of the magnetic ejecta may also erase the clear flux rope signature (Dasso et al., 2007; Kilpua et al., 2011; Ruffenach et al., 2012). Some studies classify a subset of ICMEs that meet some but not all the magnetic and plasma signature of MCs as "MC-like" or "flux rope like" (Gopalswamy, Yashiro, et al., 2015; Lepping et al., 2005; Wu & Lepping, 2015). One of the first detailed studies of an ICME with signatures of complexity was made by Lepping et al. (1997). *Wind* instruments measured a coherent structure with an embedded shock in the back half of the structure. This complex event triggered an intense geomagnetic storm for which the joint measurements by *Wind* and *Polar* provided a new coupling function between the solar wind and the magnetosphere (Farrugia et al., 1998; Takeuchi et al., 2000).

The Lepping et al. (2003) catalog of MCs has been central to numerous statistical studies (Démoulin et al., 2013, 2016; Janvier et al., 2019; Lepping et al., 2017; Lepping, Wu, Gopalswamy, & Berdichevsky, 2008, among others) and is based on the approximation of MCs as simple, circular flux rope in force-free equilibrium. The results from the analyses have shaped two different MC catalogs, both included on the *Wind* webpage https://wind.nasa.gov/ICMEindex.php These catalogs provide fitting parameters for most entries. These parameters include magnetic field strength, closest approach (or impact parameters), orientation as well as measures of the goodness of the fit for all *Wind* MC measurements.

Results from these catalogs include data-driven models of typical MCs and shocks (Démoulin et al., 2016), studies of the importance of expansion to understand MC measurements (Lepping, Wu, Gopalswamy, & Berdichevsky, 2008) as well as investigations of the impact of the distance of closest approach on the spacecraft measurements (Démoulin et al., 2013; Lepping et al., 2017). These studies revealed that the cross-section of MCs is in fact noncircular (Démoulin et al., 2013, 2019) and the distribution of magnetic field line twist may be more complex than that derived from a force-free model (Lanabere et al., 2020). These results have led to the development of several new models which incorporate more complex magnetic field structures and cross-sections.

The Nieves-Chinchilla et al. (2018) catalog also provides the internal flux-rope physical properties as well as the orientation and closest approach based on the model and reconstruction technique described in Nieves-Chinchilla et al. (2016). The statistical study published by Nieves-Chinchilla et al. (2019) revealed the remarkable spatial complexity of ICMEs. Figure 13 displays the occurrence of ICMEs with complex topology (bottom), with clear flux rope signatures (middle) and both populations compared with the sunspot number over the *Wind* mission. It has been shown by Li et al. (2018) that the orientation of ICME flux ropes follow orientation of the heliospheric current sheet, confirming the results of previous studies (e.g., Mulligan et al., 1998) based on visual inspection that found a Hale cycle dependence of the reversal in the flux rope poloidal field.

In combination with measurements from *Wind*, in situ measurements from STEREO, *Parker Solar Probe*, MESSENGER, *Venus Express*, and *Solar Orbiter* reveal the heliospheric dynamic evolution of the internal structure of MCs. The evolutionary signatures of evolution include distortions, deformations, rotations, deflections, and deviations from self-similar expansion or radial propagation (Good et al., 2019; Kubicka et al., 2016; Lugaz et al., 2020; Nakwacki et al., 2011; Nieves-Chinchilla et al., 2012; Salman et al., 2020; Vršnak et al., 2019; Wang et al., 2018; Winslow et al., 2016). These analyses use data from spacecraft that are radially aligned or in quadrature, giving multi-point or multi-view observations of the evolving MC, respectively.

In summary, *Wind* has made important contributions to the study of ICMEs ranging from confirming the fundamental association between CMEs and ICMEs and understanding the complexity of their structures and related space weather effects, through to the multi-spacecraft studies that are possible in conjunction with new missions in the inner heliosphere and beyond.

3.8.3. Corotating Interaction Regions

Wind observations of CIRs and SIRs near 1 AU have helped researchers confirm that not only are particles accelerated by these structures, the acceleration need not require a local shock. Furthermore, they have

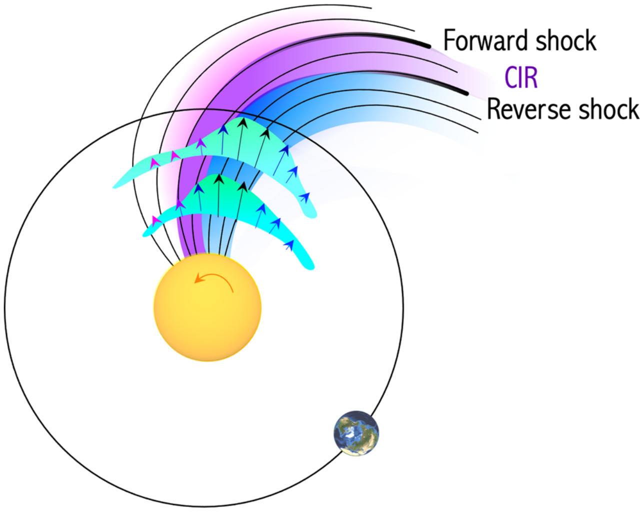

Figure 14. Cartoon of stream interaction region (SIR) and/or corotating interaction region (CIR). The black arrows indicate velocity and the solid lines represent magnetic field lines. The thick magenta and blue arrows indicate the local, outward normals of the expanding compression region that can form a forward and reverse shock, respectively, as the SIR/CIR propagates further away from the sun.

found that the structures evovle on much shorter time scales than the solar rotation period. In this section, we review some of these highlights of CIR and SIR research using *Wind* observations.

A CIR (e.g., see Richardson et al., 2018, for a recent review) is formed by the interaction of a high-speed solar wind stream (HSS) originating in a coronal hole at the Sun with the preceding slower solar wind (e.g., see Figure 14 for illustration). The term SIR is often reserved for those interaction regions that do not recur on two or more solar rotations, though SIR and CIR are also used interchangeably. This interaction forms a region of compressed solar wind—the CIR—that lies along the leading edge of the high-speed stream and has an approximately spiral configuration. CIRs/HSSs corotate with the Sun and may recur for several solar rotations. Expansion of the CIR may lead to the formation of a corotating forward (reverse) shock at the CIR leading (trailing) edge. These shocks usually form beyond 1 AU (Smith & Wolfe, 1976) but occasionally are found at 1 AU (e.g., Jian et al., 2006). They are also important drivers of geomagnetic activity, accounting for around 10% of major geomagnetic storms (Alves et al., 2006; Zhang et al., 2007). They can also generate extended (several day) periods of enhanced geomagnetic activity, driven by intermittent southward magnetic fields associated with Alfvenic fluctuations propagating outward from the Sun, as they pass over Earth (Tsurutani et al., 2006), which in turn may lead to the acceleration of MeV electrons in the outer radiation belts (Baker & Kanekal, 2008; O'Brien et al., 2001). Such "killer electrons" are often associated with spacecraft anomalies or failures (e.g., Wrenn et al., 2002).

Jian et al. (2006) summarize the properties of 365 SIRs (some of which are CIRs) at 1 AU during 1995–2004 using *Wind* and ACE data, and provide a catalog of these events and their properties. They emphasize the use of the total (magnetic and plasma) pressure perpendicular to the magnetic field direction as an aid to identifying interaction regions, with a local pressure peak being a characteristic feature of the stream interface (Forsyth & Marsch, 1999) separating slow and fast solar wind plasma. They found that ~17% (5.75%) of interaction regions at 1 AU had only a forward (reverse) shock, and 1.37% had a forward-reverse shock pair. An extended catalog of 588 CIR/HSS during 1995–2017 has been compiled by Grandin et al. (2019) using a detection algorithm applied to OMNI data which incorporates *Wind* observations. They also show superposed-epoch analyses of the solar wind parameters and geomagnetic activity associated with these structures for different phases of solar cycles 22–24, noting for example, cycle to cycle variations in their occurrence and properties, such as the lower geoeffectiveness of CIRs/HSS in cycle 24 due to lower magnetic field strengths and lower stream speeds (e.g., see Figure 15).

Although CIRs and HSSs are long-lived structures corotating with the Sun, they do evolve on shorter timescales, for example due to changes in the configuration of the source coronal holes and development of the stream interaction. Several studies have used data from *Wind* and other spacecraft separated from Earth to study this evolution. For example, Jian et al. (2009) examined a CIR in August 2007 that was observed in succession by STEREO B, 10° east of *Wind*, then by *Wind*, and by STEREO A, 15° to the west; the spacecraft were only separated by 2° in heliolatitude. Figure 16 shows the differences in the profiles of various solar wind parameters at each spacecraft (the CIR is indicated by enhanced magnetic fields and plasma densities on the leading edge of the HSS) and the varying locations of a crossing of the heliospheric current sheet (HCS) – The boundary that separates the two magnetic polarities or hemispheres of the heliosphere – ahead of the CIR, the stream interface (SI), and a forward shock forming at the CIR leading edge, which was only present at *Wind*, and a reverse shock forming at the CIR trailing edge, only evident at STEREO (b) Occasionally, a MC interacts with a CIR, as in the example discussed by Farrugia et al. (2011). Observations from *Wind* and both STEREO spacecraft, separated by ~40° in heliolongitude, illustrate the distortion and rotation of the MC that resulted from this interaction.

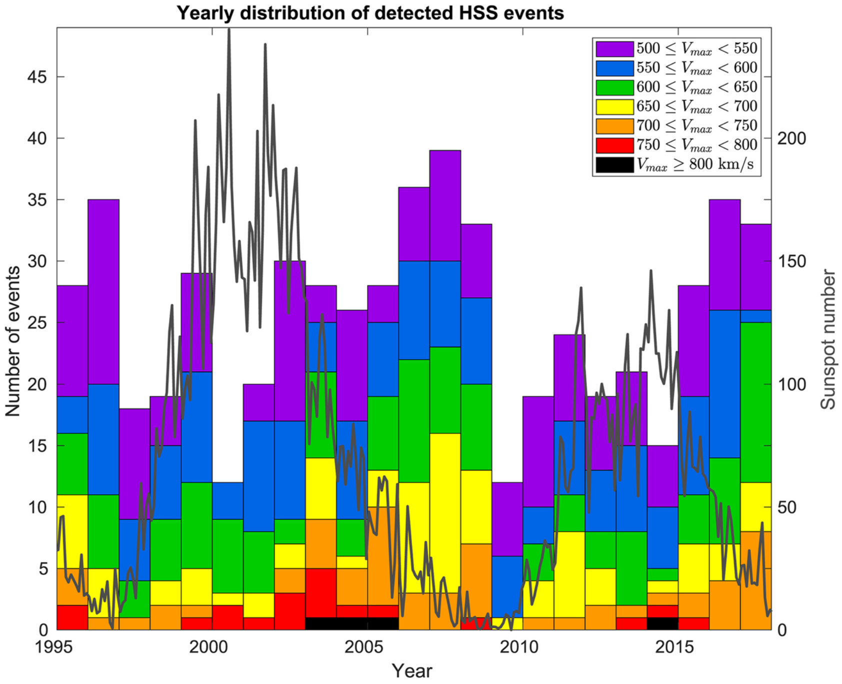

Figure 15. Yearly number of high speed streams in various peak speed ranges (minimum 500 km/s) with the sunspot number for solar cycles 23 and 24 superposed, showing the tendency for HSS to be most frequent during the declining phase of the cycle and the generally lower peak speeds in cycle 24 versus 23 (Adapted from Grandin et al., 2019).

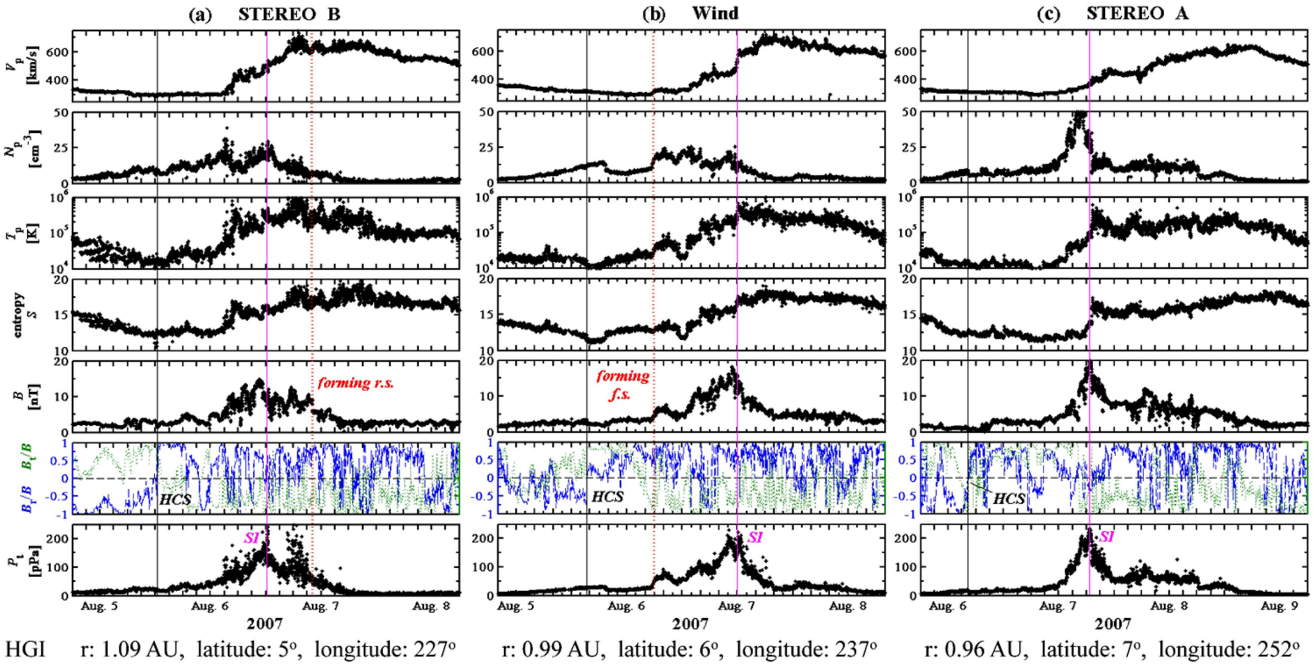

Figure 16. A CIR and HSS observed in turn by STEREO B (left), *Wind* (center) and STEREO A (right), illustrating the differences in various solar wind parameters observed over a heliolongitude range of only 25°. The parameters shown are (from top) the solar wind speed (V_p), proton density (n_p) and (n_p) and temperature (T_p), entropy ($S = \ln | T_p^{3/2} \, n_p |$), magnetic field intensity (B_o), the ratios of the radial and transverse components of the magnetic field to field to B_y, and the total perpendicular pressure (P_t) (Adapted from Jian et al., 2009).

Such studies about CIRs and SIRs Jian et al. (2009) have highlighted a number of important aspects of the variability of corotating solar wind streams: (a) their properties, including the presence/absence of shocks, can vary significantly close to the ecliptic even with small latitudinal separations as the slow and fast wind streams are tilted and the interaction region can have a complex 3D shape, (b) their properties can have large variations on moderate timescales (∼6–24 h); some of this variability is likely to be associated with the changing boundaries and magnetic field distribution of equatorial coronal holes at the Sun (the source of the fast solar wind streams), (c) Earth (or 1 AU in general) is situated in a place where the interaction process between slow and fast streams is still ongoing. As such, small variations in longitude, latitude or radial distance can result in significant differences in the SIR/CIR properties, in a way which is not necessarily clearly understood yet. While *Wind* prograde orbits in 2000–2002 can be used for such studies, there have not been any dedicated measurements of the solar wind 0.5–5° from the Sun-Earth line since, except for a few months of STEREO measurements after launch in 2007.

Broiles et al. (2012) used observations from *Wind* and ACE to search for planar magnetic structures in 153 CIRs and, from their orientation, inferred the tilt of the CIR, which might be expected to reflect the orientation of the fast-slow stream interaction. The mean azimuthal tilt was found to be consistent with the average Parker spiral direction. Average out-of-the-ecliptic tilts were ∼20° both north or south, but these values often changed significantly between successive recurrences of the same stream. Such studies for example raise questions about using observations from a spacecraft monitoring the solar wind, and particularly CIRs/HSS, at a location east of Earth (e.g., L5) to provide an advance forecast of near-Earth solar wind conditions. They also suggest the presence of a complex, evolving, structured solar wind in the inner heliosphere that can be studied by *Parker Solar Probe* and *Solar Orbiter* in conjunction with observations by *Wind* and other spacecraft at 1 AU.

Several studies of energetic particles associated with CIRs have been made with *Wind*/EPACT. For example, (Mason et al. 1997, 1999) used measurements from *Wind*/EPACT to demonstrate that the spectra of energetic particles do not show the depletion of low energy ions expected (Fisk & Lee, 1980) if the particles were accelerated at CIR shocks at several AU (Barnes & Simpson, 1976). That is, the particles would lose energy due to adiabatic deceleration in the expanding solar wind whilst propagating sunward to the spacecraft. Instead, observations suggest the particles are accelerated closer to the spacecraft. Chotoo et al. (2000) found that the spectra of energetic particles in the vicinity of CIRs merged with the suprathermal tail of the solar wind ion distribution, also suggesting that the particles were accelerated relatively local to the spacecraft, possibly out of the solar wind distribution. Ebert et al. (2012) used EPACT/STEP observations of suprathermal He ions to show that acceleration occurred near the trailing edges of two well-developed CIRs. One of the CIRs was associated with a reverse shock, while the other was not. This surprising result suggests that particle acceleration at CIRs does not require the presence of a shock. Filwett et al. (2017) investigated suprathermal heavy ion abundances at 41 CIRs using STEP. The authors concluded that the upper limit on the distance traveled from the source to the spacecraft was 1 AU, which is consistent with a relatively local source. Filwett et al. (2017) also found evidence for enhanced Fe abundances in CIR-associated particles at higher solar activity levels. Their result suggests that Fe-rich particles from impulsive solar events contribute to the source of CIR particles. Interstellar pick up ions—interstellar neutrals that are ionized near the Sun—such as He^+ (Chotoo et al., 2000), may also be accelerated at CIRs (Chen et al., 2015). Reames (2018), using EPACT/LEMT data, concluded that the element abundances of CIR-accelerated ions mirror the solar wind abundances with a modification depending on the mass to charge ratio of the ions.

3.9. Solar Energetic Particles

The *Wind* EPACT/LEMT instrument was the first to detect ultra-heavy ($34 \leq Z \leq 82$) ions in impulsive solar particle events accelerated by solar flares and jets. *Wind*'s longevity has given researchers a unique opportunity to examine SEP abundances at lower masses over extended time periods. In this section, we highlight some advances made by *Wind* on the topic of SEPs.

The *Wind* EPACT instrument has made observations of solar energetic particles or SEPs throughout the mission lifetime (e.g., see Reames, 2017, and references therein). First, we highlight one result that illustrates the ability of the EPACT/LEMT instrument to detect, for the first time, ultra-heavy ($34 \leq Z \leq 82$) ions

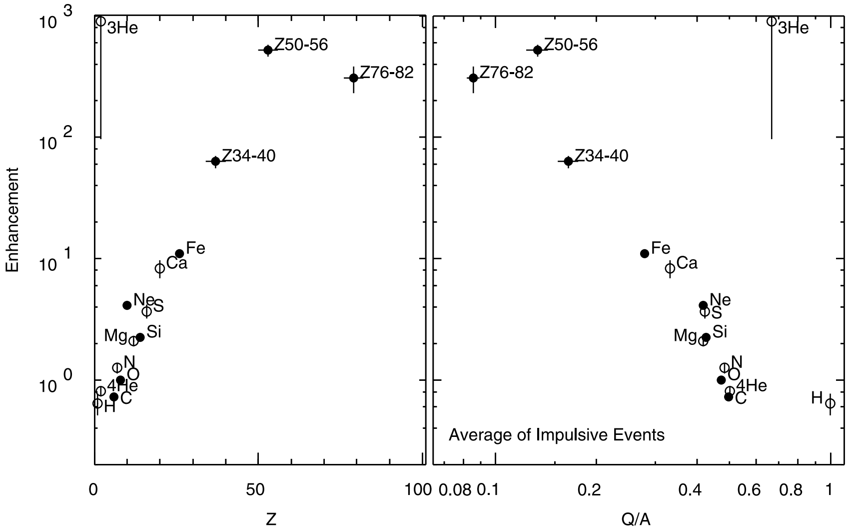

Figure 17. Abundance enhancements in average large impulsive events relative to coronal abundances, shown as a function of atomic number, *Z*, and charge-to-mass ratio, *Q*/*A*, at ~3 MK. The solid circles are from the study by Reames and Ng (2004) and open circles are from previous studies (Adapted from Figure 4 in Reames & Ng, 2004).

in impulsive solar particle events accelerated by solar flares and jets. With a large collecting geometry, a large dynamic range above ~2 MeV amu^{-1}, and a pulse-height analysis scheme that prioritizes $Z > 33$ particles, LEMT is ideal for heavy element detection. It was well-established by previous missions that smaller and shorter duration "impulsive" SEP events accelerated by solar flares exhibit remarkable enhancements in the abundances of ^{3}He and heavy ions compared to coronal abundances. LEMT observations (Reames, 2000; Reames & Ng, 2004) demonstrate that these abundance enhancements extend to ultra-heavy ions.

Figure 17, from Reames and Ng (2004) shows the increase in the ion abundance enhancement relative to coronal abundances with increasing *Z*. Clearly, the ultra-heavy ions continue the trend evident for ions lighter than iron (filled circles are LEMT data, open circles are from previous missions). Figure 17 (right) shows that the abundance enhancements decrease with increasing *Q*/*A*, where a coronal temperature of 3 MK is assumed to estimate the charge states. Note that the enhanced but low charge state ^{3}He does not fit these trends, suggesting that the ^{3}He enhancement arises from a separate process. Remarkably, the strongest heavy ion enhancements are associated with the smallest impulsive events associated with the weakest solar flares and softest particle spectra (Reames & Ng, 2004).

The reason for these heavy and ultra-heavy ion abundance enhancements is still under discussion, but they may occur if the ions interact with a turbulent region where there is more power at larger length scales, which favors the acceleration of heavier ions with larger gyroradii. A promising candidate is the formation of islands by reconnection (Drake et al., 2009; Drake & Swisdak, 2012), where the island size distribution may lead to a strong *Q*/*A*-dependence in the particle abundances. However, such a process could not account for the enhancement of ^{3}He over ^{4}He. This may result instead from acceleration through a resonance with ion cyclotron waves generated by streaming electrons (Roth & Temerin, 1997; Temerin & Roth, 1992).

The *Wind* mission has also allowed SEP abundances at lower masses to be compared over an extended time period. For example, Reames et al. (2014) show, for 8 h intervals during a 19 year period, a range of values of Ne/O and Fe/O (both normalized to typical values in large SEP events) at ~3 MeV/nucleon. The observations show evidence for a bimodal distribution, with a group of periods with enhanced Fe and Ne abundances likely to be associated with impulsive SEP events and another, larger, group with abundances similar to those in large SEP events, associated with gradual events. However, intervals with intermediate values are also present.

Considering particles accelerated by interplanetary shocks, Reames (2012) studied the spectra of ~1–10 MeV/nucleon ^{4}He at 258 shocks in the CfA Wind shock database (https://www.cfa.harvard.edu/shocks/

wi_data/) with the aim of determining which shock parameters are more important to produce particle acceleration. Only 39 (∼15%) of these shocks had significant particle acceleration to these energies, and the shock speed was found to be the strongest determinant of the particle intensity at the shock followed by the shock compression ratio; quasi-perpendicular shocks were also favored.

3.10. Solar Radio Bursts

Before the launch of *Wind*, type II bursts were known in only two domains: metric (>15 MHz) from ground-based observations, and hectometric-kilometric (<2 MHz) from space-based observations (e.g., see discussion in Maroulis et al., 1993, and references therein). These frequencies correspond to spatial domains of <2 R_s and > 10 R_s from the Sun center. The *Wind*/WAVES experiment is capable of observing radio emission in ∼2–14 MHz range and determining the direction to the emission source region. Thus, *Wind*/WAVES filled a previous observational frequency gap and narrowed down the source regions of these emissions, resulting in a number of new discoveries that will be highlighted in this section. The coronal domain sampled by *Wind*/WAVES overlaps with that imaged by space-borne coronagraphs. A quarter century of *Wind*/WAVES observations and white-light observations from the Solar and Heliospheric Observatory (SOHO) mission have contributed enormously to our understanding of solar eruptions and their heliospheric consequences. The combined radio and coronal imagery were enhanced with the addition of STEREO in 2006, which greatly advanced our understanding of inner heliospheric nonthermal processes associated with solar magnetic active regions. All radio emissions are due to nonthermal electrons of various energies, so the radio bursts provide key information not only on the particle energization process but also on the ambient medium in which the electrons propagate and produce the radio signatures. Note that in this section, we intentionally refer to both coronal mass ejections (CMEs) and interplanetary coronal mass ejections (ICMEs). The former refers to CMEs observed using coronal imagers and the later to those observed with in situ plasma measurements (see Section 3.8.1).

Nonthermal radio signatures in the IPM are simple compared to those in the corona (<2 R_s). Most of the IP radio emissions arise from the plasma emission mechanism (i.e., nonthermal electron beams excite Langmuir-like waves which nonlinearly mode convert to free electromagnetic radio emissions at frequencies near the plasma frequency of their source region), whereas near the Sun additional mechanisms such as cyclotron emission, gyrosynchrotron emission, and bremsstrahlung emission operate. Early *Wind* studies showed that nearly all the known radio burst types (e.g., type II, type III, and type IV; see review by Wild et al., 1963) were observed by the WAVES radio receivers (Bale et al., 1999; Gopalswamy et al., 1998, 2001, 2001; Gopalswamy, 2004a, 2004b; Gopalswamy & Mäkelä, 2010; Kaiser, 2003; Reiner et al., 1998, 2001). Type I radio bursts occur at higher frequencies than can be resolved by *Wind*/WAVES, so they will not be discussed herein.

Type III bursts occur as regular, frequency-drifting radio emissions and as type III storms. Type III storms typically start in the metric domain (around 80 MHz) in association with type I storms at higher frequencies but extend down to sub-MHz frequencies. Type III storms are characterized by broadband (>few MHz), very short duration (i.e., $\lesssim$1–2 min) emissions that occur in rapid succession (typically > 10 per hour). Type III bursts are characterized by their fast frequency drift (i.e., MHz per minute) versus time, which is a tracer of the gradient in the IP electron number density. Type III storms are caused by nonthermal processes taking place in active regions outside of eruptions. Both type III storm bursts and regular type III bursts result from emissions due to nonthermal electrons propagating along open magnetic field lines. Type II bursts are caused by nonthermal electrons accelerated by CME-driven shocks. Type II bursts are characterized by their slow frequency drift (i.e., few 100s of kHz per hour) versus time, which is a tracer of the shock speed and electron number density upstream of the shock. Type IV bursts are thought to be due to nonthermal electrons trapped in post-eruption arcades (i.e., half-loop-like arches of intense magnetic field connecting to active regions on the solar surface) in the eruption site. Type IV bursts are characterized by a broadband frequency emission in the several to >10 MHz range, sometimes showing a U-shaped profile.

Figure 18 shows a solar eruption that exhibits all the IP burst types: type III storm, type III burst, type IV burst, and type II burst. All the burst types are associated with complex magnetic regions on the Sun. All but the type III storm are associated with solar eruptions involving CMEs and solar flares.

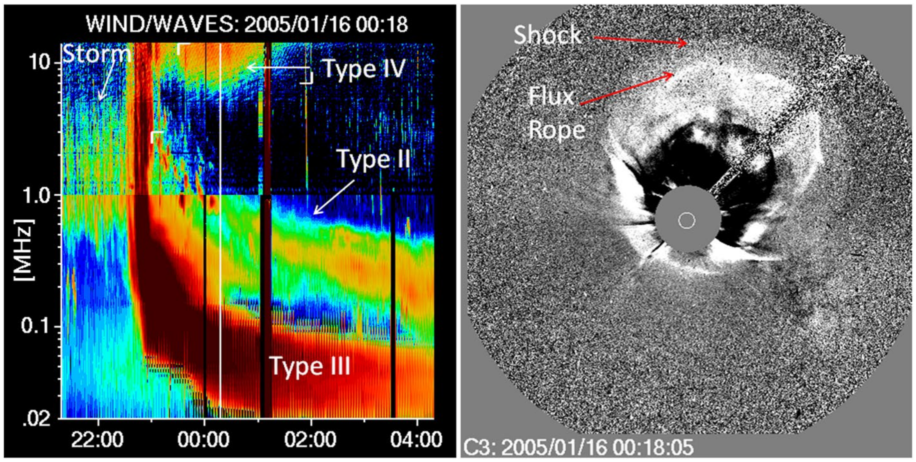

Figure 18. Four types of radio bursts observed by *Wind*/WAVES on January 15, 2005 toward the end of the day: type III storm was in progress when the eruption occurred. The eruption is marked by the regular type III burst, followed by a type II burst and a type IV burst. (right) The associated CME observed by SOHO/LASCO. The CME has a flux rope driving a shock as indicated. The shock is at a heliocentric distance of $\sim$25 R_s in sky-plane projection (Adapted from Gopalswamy, 2016).

3.10.1. Type II Bursts

As previously stated, type II bursts result from nonthermal electrons accelerated by CME-driven shock waves. Thus, they are a tracer of the shock speed/position versus time and of the electron number density immediately upstream of the shock front. Remotely tracking shocks using radio waves is an important element of our space weather forecasting infrastructure. It also provides information on the radial gradient of the IP electron number density, critical for heliospheric models. Therefore, it is important to understand the origin and evolution of the frequency drifts of type II bursts.

Type II bursts can exist in the decametric-hectometric (DH), metric (m), and km wavelength range. Interestingly, there are type II bursts that start in the m range and evolve to the DH range (i.e., meter to DH or m-DH range) while other DH type II bursts are not continuations of m type II bursts. Some type II bursts start in the DH range and end there as well, called pure DH type II bursts. Some type II bursts occur in the m and DH ranges simultaneously while others start in the m range and evolve to the DH and onto the km range. Finally, there can be purely km type II radio bursts (Gopalswamy, 2004a; Gopalswamy et al., 2000; Kaiser et al., 1998; Reiner & Kaiser, 1999). Thus, initially there was a mystery as to the source of the diversity in type II radio bursts.

The mystery was resolved in a subsequent investigation by Gopalswamy et al. (2005) who found that the wavelength extent of type II bursts depends on CME kinematics, that is, their speed and acceleration/deceleration. The authors showed that the frequency/wavelength of the radio emissions depends upon the CME speeds where the emission ranges and speeds (averages from multiple events) were: ~610 km/s (m), 1,068 km/s (m-DH, DH, and DH-km combined), 1,490 km/s (m-to-km), and 540 km/s (purely km). When examining coronal images using the SOHO coronagraphs, Gopalswamy et al. (2005) observed all CMEs decelerated in the coronagraph FOV except those associated purely km type II bursts. These accelerated to super Alfvénic speeds at tens of R_s from the Sun.

Simultaneous type II bursts at different frequencies

Further investigation after the accumulation of numerous type II bursts showed the simultaneous occurrence of two type II bursts: one in the DH domain that evolved from the m domain and one starting in the DH domain and continuing to the km domain. Gopalswamy (2011) reported on one such CME-associated event on June 17, 2003 where the inferred source height of the m-DH component (from the Sun center) was $\sim$2.4 R_s and the DH-km type II was at $\sim$7 R_s. A possible explanation proposed was a curved shock front where the nose was at $\sim$7 R_s and the R_s and the flanks at $\sim$2.4 R_s (e.g., see the shock surrounding the flux rope in Figure 18). The CME was very fast (~1,800 km/s), so the flanks are also fast enough to drive shocks and accelerate electrons. The flanks are at lower altitudes (where the higher electron density corresponds to higher emission altitudes (lower electron density corresponds to lower emission frequency). The Gopalswamy (2011) study is supported by an earlier study by Raymond et al. (2000) of a slower CME (only ~1,300 km/s, thus without flank shocks), only showing type II bursts in the m domain.

Wind/WAVES is also capable of determining the direction from which a radio emission propagated to the spacecraft (Hoang et al., 1998). This analysis has been applied to another fast CME (~1,900 km/s) on July 6, 2012 with both m-DH and DH-km domain type II bursts (Mäkelä et al., 2018). The authors also used the same technique using STEREO to confirm the source regions to be near the nose of the CME shock. Thus, these studies support the nose-flank emission source regions, in contrast to another model that invokes a second shock—the flare blast wave—to explain the metric emission.

Type II burst dependence on ICME properties

Another curiosity is that not all CMEs have an associated type II burst. By the end of 2019, *Wind*/WAVES has observed more than 500 bursts at frequencies below 14 MHz. Even so, early work of ~100 events revealed that type II bursts are associated with fast (>900 km/s) and wide (>60°) CMEs (Gopalswamy et al., 2000, 2001). Later work noted that the average CME speed in the sky plane of coronagraphs has increased to ~1,164 km/s due to the energetic CMEs during the maxima of cycles 23 and 24 (Gopalswamy, Mäkelä, & Yashiro, 2019).

An interesting correlation was observed between the initial deceleration and initial speed of CMEs associated with type II bursts. The CMEs were found to decelerate in the coronagraph FOV at ~0–100 m s^{-2}, where the deceleration is correlated with initial speed (Gopalswamy et al., 2001). Later work confirmed the correlation between initial deceleration and initial speed using the frequency drift rate of the observed type II bursts (Reiner, Kaiser, & Bougeret, 2007; Zhao et al., 2019).

Given that CMEs are strongly coupled to the solar cycle, examinations of DH type II bursts showed a solar cycle variation with maximum rates of ~10 bursts per Carrington rotation (~27.3 days)—the approximate rotation period of low solar latitudes—during solar maximum. However, no DH type II bursts were observed in the lowest part of solar minimum (Gopalswamy et al., 2020). Interestingly, the occurrence rate of type II bursts depends upon the CME properties (i.e., fast and wide CMEs produce type II bursts) rather than the sunspot number (SSN). Gopalswamy et al. (2020) showed that the decrease in SSN between solar cycles 23 and 24 was ~39% while the decrease in type II bursts was ~48%. The authors argued the decrease in fast and wide CMEs was also ~48%, illustrating the connection between the CMEs and type II bursts.

Shock arrival prediction using type II bursts

Recall that type II bursts are a tracer of the shock speed/position versus time and of the electron number density immediately upstream of the shock front. Thus, researchers can use the frequency drift rate, $\frac{df}{dt}$, as a function of time to examine the evolution of the associated ICMEs and the density gradients in the IPM. Aguilar-Rodriguez et al. (2005) showed that the drift rate followed a power law of the form $\left| \frac{df}{dt} \right| \sim f^{-\varepsilon}$, where the exponent $\varepsilon \sim 1.8$ for the entire wavelength domain (m to km) and was higher in the km domain (2.7 at $f < 1$ MHz), and lower at m-DH domain (1.5 at $f > 1$ MHz). The different exponents in the different spectral domains reflect the CME/ICME evolution at different distances from the Sun (Gopalswamy & Mäkelä, 2011; Vršnak et al., 2001). Initially ICMEs accelerate into a more and more tenuous region which results in a smaller ε. Further from the Sun, ICMEs decelerate which increases ε. The evolution of the ICME shocks and influence on ε have been supported by case studies (e.g., Gopalswamy, Mäkelä, Akiyama, et al., 2018; Liu et al., 2013).

After type II bursts reach the km range their evolution is more consistent with a constant IP shock speed, thus allowing researchers to predict the shock arrival time at Earth. Cremades et al. (2015) combined coronagraph images of CMEs, type II radio emissions in the km range, and in situ information on shocks to investigate the height-time history of 71 IP shocks. The authors were able to predict the shock arrival time within ~6 h for 85% of the events. Other studies (Corona-Romero et al., 2013) attempted to approximate the shock evolution as that of a blast wave. However, the speeds of magnetic clouds (MCs) and the associated shocks have been shown to be highly correlated (95%) (Gopalswamy, 2006). Thus, ICMEs and their shocks remain coupled at 1 AU, even though both have undergone significant decelerations, which is inconsistent with a blast wave scenario.

Type II bursts and SEPs

Type II bursts are the earliest indicators of CME-driven shocks, and can also serve as an indicator of solar energetic particle (SEP) events because the same shock accelerates electrons and ions (see Section 3.9 for more discussion of SEPs). Recall that the observed frequency of type II bursts is strongly related to the CME speed. For instance, purely m type II bursts are associated with average speed CMEs satisfying ~600 km/s while m-DH type II bursts are associated with >1,000 km/s CMEs. Faster CMEs tend to result in stronger (higher Mach number) IP shocks, which are known to be more efficient accelerators of particles (e.g., see discussion in Caprioli & Spitkovsky, 2014, and references therein). Therefore, investigating the relationship between type II bursts and SEPs was an obvious avenue for improving space weather forecasting.

Cliver et al. (2004) found that only ~25% of purely m type II bursts are associated with >20 MeV SEP events but the rate almost quadrupled to 90% when a m type II had a DH counterpart. Gopalswamy et al. (2005) found that CMEs producing type II bursts in the m-to-km range also had high energy SEPs. Furthermore, all SEPs strong enough to generate a ground level enhancement (GLE)—solar particles observed by ground-based instruments—are associated with m-to-km type II bursts (Gopalswamy et al., 2012).

Later work (Cliver et al., 2019; Gopalswamy, Mäkelä, et al., 2015; Gopalswamy, Yashiro, et al., 2016) found that the initial frequency of type II bursts correlated with the spectral slope of the SEP number flux versus energy power-law relationship. Shocks forming closer to the solar surface (i.e., with a higher initial type II burst frequency) had harder spectra (i.e., indicates a flatter or less-steep drop in number flux with increasing energy) than those forming at higher altitudes. The harder spectra SEP events are often also GLE events. The reason for the shock formation altitude dependence on spectral slope relates to the background plasma parameters in which the shock formed. At lower altitudes, the magnetic field magnitude is much larger and the geometry is more complicated, both of which make for more efficient particle scattering and acceleration (Cliver et al., 2019; Gopalswamy et al., 2017).

Finally, the examination of type II bursts have helped us understand the source of the >300 MeV protons required for producing the pion-decay continuum observed as sustained gamma-ray emission (SGRE) from the Sun (Gopalswamy, Mäkelä, Yashiro, et al., 2018; Share et al., 2018). Gopalswamy, Mäkelä, Yashiro, et al. (2018) and Gopalswamy, Mäkelä, Yashiro, et al. (2019) demonstrated a close linear relationship between the SGRE and type II burst durations, in every SGRE event with duration > 3 h, supporting the hypothesis that the >300 MeV protons continue to be accelerated at the shock as it moves away from the Sun, and then propagate back to the Sun, generating the SGRE. However, other studies (de Nolfo et al., 2019; Klein, Tziotziou, et al., 2018; Malandraki & Crosby, 2018) may not support this hypothesis for the origin of SGRE.

3.10.2. Type III Bursts

Type III bursts result from nonthermal electrons accelerated in solar magnetic active regions exciting plasma waves as they stream along the magnetic field away from the Sun. Early work using triangulation between *Ulysses* and *Wind* identified the electron beam source of type III bursts, finding that the electrons were traveling at a speed of ~0.3 c (Reiner et al., 1998). When the radio emission of a type III burst reaches the local plasma frequency of the observing spacecraft, the emission is occurring locally. Reiner and MacDowall (2015) analyzed five in situ type III radio bursts observed by *Wind* and STEREO, finding that the electron beam speed ranged from 0.2 c to 0.38 c near the Sun but was only ~0.2 c near 1 AU. The reduction in beam speed corresponded to a deceleration of ~30 km s^{-2}. That is, the primary electrons exciting type III bursts near the sun correspond to energies of 20–30 keV while they drop to ≤ 10 keV near 1 AU. The reduction in energy is consistent with the beam losing energy as it converts kinetic energy to electromagnetic energy to generate the initial Langmuir waves.

Type III bursts generally accompany SEP events (e.g., Cane et al., 2002; MacDowall et al., 2003, 2009; Miteva et al., 2017; Richardson et al., 2018; Winter & Ledbetter, 2015, and see Section 3.9). In particular, large SEP

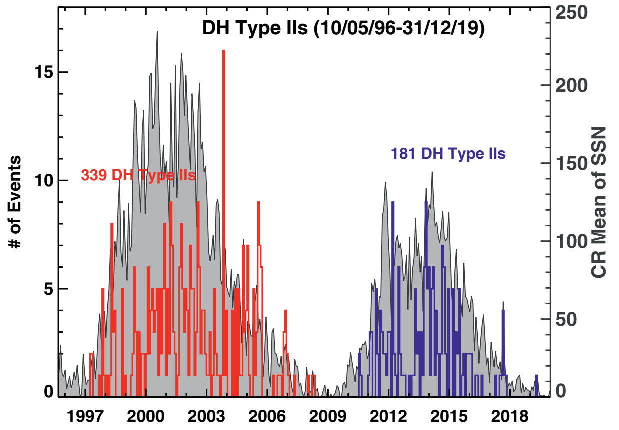

Figure 19. Occurrence rate of DH type II bursts May 10, 1996–December 31, 2019 (red: cycle 23; blue: cycle 24) summed over Carrington rotation periods. The sunspot number is shown for comparison. Gopalswamy, Mäkelä, and Yashiro (2019) found that the drop in the number of events in cycle 24 is similar to the drop in the number of fast and wide CMEs (figure updated from Gopalswamy, Mäkelä, & Yashiro, 2019).

events are usually associated with bright, long duration, complex type IIIs such as that shown in Figure 19. These long-duration emissions were originally thought to result from electrons accelerated at or associated with CME-driven shocks (Bougeret et al., 1998; Cane et al., 1981). Based on *Wind*/WAVES observations, which as discussed above, closed a frequency gap between ground and previous space-based instruments, these complex type III emissions can appear to extend from the associated type II bursts (Gopalswamy et al., 2000), but they are now thought to result from electron acceleration in magnetic reconnection below CMEs (Cairns et al., 2018; Cane et al., 2002; Reiner et al., 2000). Characteristics such as correlations between the burst duration or intensity and SEP peak intensity, and their rapid onset and frequency drift following solar flares, have led to the inclusion of type IIIs in proposed SEP prediction schemes (e.g., Laurenza et al., 2009; Richardson et al., 2018; Winter & Ledbetter, 2015). However, these require real-time radio observations that are not available from *Wind*. The largest SEP events are usually associated with type III burst durations of $\gtrsim$15 min at $\sim$1 MHz (Cane et al., 2002; MacDowall et al., 2009; Richardson et al., 2003, 2018; Winter & Ledbetter, 2015). Krucker et al. (1999) examined the relationship between type III bursts and energetic electrons observed in situ using *Wind* 3DP electron and WAVES observations. They found that while some near-relativistic electron events are released at the Sun at the time of the type III burst, others are apparently released up to half an hour later, suggesting that they originate from a different population than the type III-producing electrons. Similar conclusions were reached by Haggerty and Roelof (2002), Klassen et al. (2002), and (Wang et al. 2006, 2016). An alternative interpretation is that the energetic electrons may be delayed during propagation through the IPM (Cane, 2003; Cane & Erickson, 2003; Wang et al., 2011).

3.10.3. Type III Storms

Solar noise storms are nonthermal radio emission due to electrons accelerated in a noneruptive energy release in active regions. At metric wavelengths, noise storms manifest as type I bursts, which transition into type III storms in the outer corona. Thus, type III storms are the low-frequency extensions of type I storms (Fainberg & Stone, 1970). Type III storms can last for several days and can be observed at heliocentric distances of up to 170 R_s (Bougeret et al., 1984). Interestingly the rate of type III storms and their intensity increase as the source active region crosses the central meridian (Gopalswamy, 2004b; Morioka et al., 2015, 2007; Reiner et al., 2001; Reiner, Fainberg, et al., 2007). Further work has indicated that type III bursts and storms have different energization processes based upon differences in occurrence frequency and emitted power flux (Morioka et al., 2007).

The source regions of type III storms were later identified to be solar active regions accompanied by coronal holes. These are regions in which the magnetic field lines do not connect back to the solar surface but rather are directed outward into the IPM. The suggested mechanism (Del Zanna et al., 2011) is a type of magnetic reconnection called interchange reconnection—magnetic reconnection between coronal hole and adjacent, closed magnetic field lines that leads to the energization of low energy electrons (see Section 3.4 for details on magnetic reconnection). These sustain the type III storm on closed magnetic field loops and give rise to weak type III emission on open field lines.

Type III storms can be disrupted by CMEs for upwards of $\sim$10 h (see Figure 18). Gopalswamy (2016) reported on a type III storm starting on January 14, 2005 that was disrupted by five CMEs (including that in Figure 18), with the last one being an extreme event that occurred on January 20, 2005. Following the final CME the type III storm did not reappear suggesting a possible reconfiguration of the active region or a change in the directivity of the storm or the active region complexity.

Type III storms also exhibit an interesting change in degree of polarization with radial distance. In the metric range, type III storms have a degree of circular polarization of up to $\sim$25%. In the IPM, type III storms have much smaller degrees of circular polarization ($<5\%$) at frequencies near 1 MHz (Reiner, Fainberg, et al., 2007). Reiner, Fainberg, et al. (2007) used the change in the degree of circular polarization to determine the magnitude and radial projection of the magnetic fields above solar active regions. Typical magnetic field strengths of ∼50 mG (or ∼5,000 nT) at a heliocentric distance of 25 R_s were R_s were calculated and the field strength decreased faster than the inverse-square of the radial distance. Thus, type III storms can be used to remotely probe the magnetic structure and strength of solar active regions.

3.10.4. Type IV Bursts

Type IV bursts are another phenomenon that has been better understood through observations of their lower frequency range by WAVES in the DH frequency range. The type IV burst on May 2, 1998 studied by Leblanc et al. (2000) was one of the first observed down to 7.5 MHz (e.g., similar to the one shown in Figure 18). Gopalswamy (2004b) studied a dozen DH type IV bursts finding they are extensions of the emissions in the metric range. The type IV bursts lasted typically for ∼2 h at 14 MHz with a typical ending frequency of ∼7.7 MHz. The type IV bursts in the DH frequency range are associated with very energetic CMEs (average speed ∼1,200 km/s). Further, the average speed of CMEs (∼1,500 km/s) associated with DH type IV bursts is similar to that in large SEP events (Gopalswamy, 2011, 2016; Hillaris et al., 2016). The most likely source of type IV bursts is electrons accelerated in a solar flare site that become trapped in the closed magnetic fields of the post eruption arcades.

More recent studies discovered that DH type IV bursts have a relatively narrow emission cone (e.g., Gopalswamy, Akiyama, et al., 2016). That is, DH type IV bursts associated with eruptions in the middle of the solar disk show a symmetric time profile about their lowest frequency (i.e., the lowest frequency boundary of the emission is U shaped). In contrast, DH type IV bursts associated with eruptions on the limb of the solar disk show an asymmetric time profile. Gopalswamy, Akiyama, et al. (2016) concluded that the type IV emission cone is less than ∼60° in full width and that this narrow cone results from the small angular extent of the source region, the post eruption solar arcades. Another proposed explanation is that the shock-compressed, high-density plasmas in the foreground of the emission attenuate the intensity of the type IV bursts more on the shock flanks than the center (i.e., due to larger line of sight integration) (Pohjolainen & Talebpour Sheshvan, 2020; Talebpour Sheshvan & Pohjolainen, 2018). The reason for the narrow type IV emission cone continues to be an active area of research.

3.11. *Wind*'s Relevance to the HSO and Future Research

Wind is the "standard candle" against which numerous other missions have and continue to calibrate their instruments (e.g., McFadden, Carlson, et al., 2008). *Wind* is a primary collaborator with NASA's *Parker Solar Probe* (PSP) (Fox et al., 2015) and ESA's *Solar Orbiter* (SolO) missions (Müller et al., 2020). The short ∼88 day orbit of PSP and the ∼0.3–0.76 AU orbit of SolO will provide frequent radial and magnetic field alignments with *Wind* allowing for multi-spacecraft studies that will significantly enhance the science return of both PSP and SolO. *Wind* is also expected to play a major role in NASA's upcoming Interstellar MApping Probe (IMAP) mission (McComas et al., 2018). Below we highlight some exciting new results that arose from the combined use of *Wind* and PSP.

Wind's broad contributions to solar and heliospheric physics can be viewed through the lens of PSP's mission objectives. PSP was launched in August, 2018 to study the origin and acceleration of the solar wind in the upper solar corona. PSP will not reach its minimum perihelion of ∼10 solar radii (R_s) until 2026, but PSP is already significantly closer to the sun than any previous mission. One method of understanding the evolution of the solar wind in the inner heliosphere is to compare the near-sun PSP in situ observations with *Wind* observations at 1 AU. Although these studies may require specific spacecraft alignments and are still in their early phase, PSP and *Wind* have already provided insight into the heliospheric current sheet, stream interaction regions, and radio remote sensing as detailed in the following.

The Heliospheric Current Sheet (HCS) varies significantly from its formation in the solar corona to its interaction with Earth at 1 AU. PSP observations of HCS crossings during the first solar orbit were successfully mapped to *Wind* observations at 1 AU (Szabo et al., 2020). The authors found that during this period at solar minimum, the HCS showed remarkable stability and could be successfully traced over full solar rotations. However, earlier work showed that the internal structure of the HCS exhibits a marked difference between solar minimum and solar maximum. Although magnetic reconnection-induced magnetic structures appear to have been present near PSP as well as near 1 AU, Szabo et al. (2020) found that the characteristics of individual structures differed. Magnetic signatures were stronger and more pronounced at PSP, while density enhancements were more pronounced at 1 AU. SIRs can also be traced from PSP to *Wind* (Allen et al., 2020). This study demonstrated that during the first PSP orbit, SIRs formed well within 0.5 AU, and also determined that the associated locally accelerated Allen et al. (2020) suprathermal particles penetrate deeper into the fast stream further away from the sun.

Supplemented with data from STEREO and *Wind*, PSP radio observations of Type III radio bursts confirmed they are associated with energetic electron beams (Krupar et al., 2020). The radio beams showed significant scattering due to solar wind density fluctuations in the inner heliosphere. The predicted density fluctuation levels from the radio data were compared to the in situ PSP observations and yielded the same 6%–7% level. There are additional efforts involving SolO and *Wind* that are currently in preparation as of time of the submission of this review.

Thus, *Wind* continues to produce significant and relevant data that contribute to studies helping to improve the science output of other solar wind missions. As evidenced by the numerous recent, novel scientific studies referenced herein, *Wind* also continues to be a valuable independent mission for studies of topics ranging from solar wind physics, kinetic physics, remote solar and astrophysics to large-scale structures such as ICMEs and SIRs/CIRs. Its diverse compliment of instruments combined with their longevity and accuracy have made *Wind* a truly special resource for studies of space plasma physics.

4. Summary

Wind launched on November 1, 1994 and has journeyed through nearly every part of the terrestrial magnetosphere, several hundred R_E prograde and retrograde of Earth, to L2 and is now stationed at L1. Over its 26+ year lifetime of observations and discoveries, *Wind* has illustrated its importance and relevance by the >5,810 refereed publications, numerous discoveries and firsts, and its continued collaboration with multiple other missions in the HSO. *Wind* has made paradigm altering advances in multiple fields of study from gamma ray astrophysics to magnetospheric, solar wind, and solar radio physics. *Wind*'s longevity and diverse and redundant instrumentation has led to it becoming the so called "standard candle" for near-Earth solar wind measurements.

Wind was launched with the first Russian instrument to fly on a US spacecraft, called KONUS. It was the first such collaboration and has been extremely fruitful leading to the identification of thousands of GRBs, nearly 30 magnetars or SGRs, several magnetar GFs, and the first evidence of the source of FRBs originating from magnetars. *Wind*/KONUS continues to play an active role in the gamma ray astrophysics community as part of the IPN and GCN.

Although *Wind* was not designed explicitly to detect IPD or ISD, it has accumulated >100,000 dust impact detections through the end of 2015, publicly available through SPDF CDAWeb. The large statistics, directional information determined from *Wind*, when combined with observations from the dedicated dust instrument on *Ulysses* helped researchers calculate the flow of ISD, thus the interstellar flow. The dust impact database has also been used in collaboration with the AIM SOFIE experiment revealing a correlation between the rate of dust impacts on *Wind* and AIM observations of meteoric smoke. *Wind*'s vital contributions to dust detection are expected to continue for the foreseeable future.

Wind has passed through the lunar wake on 10 separate occasions at varying distances from the surface of the moon. *Wind*'s modern instrumentation (compared to the pioneering missions that passed through the lunar wake) helped researchers to show that the moon, an unmagnetized body, produced a wake and that the plasma-body interaction was kinetic, not fluid-like. Although more recent experiments have improved our understanding of the lunar-plasma environment, *Wind*'s contributions were groundbreaking at the time.

Wind observations showed evidence of locally energized electrons to 100s of keV associated with magnetic reconnection in the geomagnetic tail. These observations led to entirely new ideas of particle energization in reconnection events and altered our understanding of magnetic reconnection. *Wind* also helped advance our understanding of reconnection in the solar wind showing that the exhaust regions can extend to >1,800

R_E from the diffusion region. Again, these results were only obtained by leveraging *Wind*'s unique orbits and highly accurate instrumentation.

Wind also played a pivotal role in radiation belt physics, specifically on the topics of waves and particle lifetimes. *Wind*'s ability to accurately measure high cadence time series electric and magnetic fields allowed for some of the first statistical studies of large amplitude whistler waves in the radiation belts. These modes are thought to be critical for particle energization and loss from these regions. The waves were found to be orders of magnitude larger in amplitude than previously thought and caused a dramatic shift in our understanding of particle lifetimes in the radiation belts that was used to justify several primary science objectives for NASA's *Van Allen Probes* mission.

Wind made major advances in the study of foreshocks as well. First *Wind* showed the spatial extent of the terrestrial foreshock was much larger than previously thought, that is, increased from ~200 R_E to >3,000 R_E. *Wind* observations also led to the discovery of a new TIFP called a foreshock cavity. the first to show that TIFPs can locally generate their own mini-foreshocks, which led to a whole new field of study and the later discovery that TIFPs can locally generate relativistic electrons. Given that TIFPs are thought to play a critical role in particle dynamics and global dynamics of both the bow shock and magnetosphere, understanding them is critical for space weather predictions and magnetospheric dynamics.

The diverse, redundant, and accurate array of instruments on *Wind* have led to major advances in our understanding of kinetic-scale instabilities and waves. This combined with the longevity of continuous measurements has even allowed researchers to tease out otherwise impossibly subtle features to reveal the importance of both Coulomb collisions and instabilities in the evolution of the solar wind. The longevity also helped researchers reduce the signal-to-noise ratio enough to test numerous previously inaccessible theories to find that, for instance, predictions that most solar wind VDFs are unstable. In short, *Wind*'s instrumentation and longevity have been critical to advancing our understanding of kinetic-scale instabilities and waves affecting multiple fields of study.

Not only has *Wind* greatly advanced our understanding of the comparatively coherent phenomena of instabilities, but also our understanding of plasma turbulence. Long-term measurements in the solar wind provided the first opportunity to perform statistics across multiple solar cycles. *Wind* has revealed that the scale at which bulk motions of the plasma convert and mix into random thermal motions of the constituent particles depends on the magnetization of the plasma and the ability of the slow solar wind to support a "1/f" range. *Wind* has also shown that solar wind turbulence is anisotropic, consistent with critical balance theory, and has improved our understanding of the location of the so called spectral break. Given the importance of turbulence to the evolution of the solar wind and inaccessible astrophysical plasmas, the advancements made by *Wind* observations should not be understated.

As previously mentioned, the long-term baseline of solar wind observations makes *Wind* a perfect platform for statistical studies. As such, *Wind* played a pivotal role in our understanding of the importance of collisional effects on the evolution of the solar wind plasma. This is surprising given that the plasma is, at best, weakly collisional near Earth. *Wind* also performed the first statistically significant, long-term study of the $\left(T_e / T_s\right)_{tot}$ ratio, a parameter critical for testing numerous theories from instabilities to turbulence to spectral inversion in astrophysics. *Wind* showed novel relationships between the relative abundance between protons and alpha-particles and the solar wind speed and sunspot number.

Wind has made critical contributions to our understanding of IP collisionless shock waves. Studies using *Wind* have improved our understanding of energy dissipation mechanisms, particle energization mechanisms, energetic particle sources, and shock evolution through remote detection. *Wind* studies have also shown that the structure of low Mach number, low plasma beta, quasi-perpendicular shocks are not laminar as originally theorized. In fact, the electromagnetic magnetosonic-whistler precursor waves have amplitudes exceeding the shock ramp amplitude, thus containing the largest magnetic field gradients in the shock. As previously discussed, *Wind* also showed that TIFP can generate their own mini-foreshock within the larger terrestrial ion foreshock. All of these advances have reignited interest in collisionless shock waves and improved our understanding of their dynamics and the importance of kinetic phenomena within.

Studies of ICMEs have made major strides in the decades since *Wind*'s launch. We now know that most IP shocks near Earth are caused by ICMEs, and have a better understanding of the magnetic structure of ICMEs and their space weather impacts because of *Wind*. *Wind* also made the first measurements of extremely cold (~1 eV), collisionally mediated electrons within an ICME, something that is not possible with any other current space mission. *Wind* has also made advances in the study of CIRs/SIRs confirming that they are efficient at particle energization even when they do not yet exhibit a collisionless shock near Earth.

Wind made the first in situ measurements of ultra-heavy ions in SEP events with atomic numbers between 34 and 82. *Wind* also discovered, through long-term statistical analysis, that the weakest solar flares are associated with the strongest SEP enhancements. These measurements were made by instrumentation that are currently unique to *Wind* for near Earth missions.

Remote radio measurements from *Wind* have also led to numerous advances in understanding solar phenomena. Prior to the launch of *Wind*, there were virtually no observations of solar radio emissions between ~2–15 MHz, that is, ~2–10 R_s from the Sun center. *Wind* found that the occurrence of type II bursts depends on the rate of the fast and wide CMEs that generate type II bursts, not on typical solar activity indices like the sunspot number. Type II bursts are important because they can be used to help predict SEP events and the arrival times of ICME shocks, both critical space weather phenomena. *Wind* made some of the first in situ measurements of the electron beams generating type III bursts and was the first to measure type VI bursts down to ~7.5 MHz. No other near-Earth mission has the accuracy, sensitivity, and capabilities of *Wind* for radio measurements.

The *Wind* mission is perhaps best known as a solar wind monitor but it also has one of the most diverse arrays of instrument suites. For a majority of the mission, *Wind* provided the only observations of kinetic phenomena in the solar wind, and *Wind* is still the only mission to provide comprehensive, high-cadence plasma measurements across multiple solar cycles. *Wind* continues to provide continuous low-frequency solar radio observations, which are a critical part of space weather monitoring. In summary, the list of accomplishments and advances made by the *Wind* mission are extensive. Its contribution to multiple areas of research cannot be over stated and it continues to operate nominally even after 26+ years of service. With the launch of PSP and SolO and future missions, the importance of *Wind* is only expected to grow, not diminish. For this reason and the numerous listed and unlisted above, *Wind* is a very special and critical spacecraft.

Appendix A: Definitions and Notation

This appendix lists the symbols/notation used throughout.

one-variable statistics

- $X_{min} \equiv$ minimum
- $X_{max} \equiv$ maximum
- $\bar{X} \equiv$ mean
- $\tilde{X} \equiv$ median
- $X_{5\%} \equiv$ fifth percentile
- $X_{25\%} \equiv$ 25th percentile
- $X_{75\%} \equiv$ 75th percentile
- $X_{95\%} \equiv$ 95th percentile
- $\sigma \equiv$ standard deviation
- $\sigma^2 \equiv$ variance

Fundamental parameters

- $\varepsilon_o \equiv$ permittivity of free space
- $\mu_o \equiv$ permeability of free space
- $c \equiv$ speed of light in vacuum [km s^{-1}] $= \left(\varepsilon_o \ \mu_o\right)^{-1/2}$
- $k_B \equiv$ the Boltzmann constant [J K^{-1}]
- $e \equiv$ the fundamental charge [C]

Plasma parameters

- $\mathbf{B}_o$ ≡ quasi-static magnetic field vector [nT] with magnitude B_o
- ns ≡ the number density [cm−3] of species s
- ms ≡ the mass [kg] of species s
- Zs ≡ the charge state of species s
- qs = Zs e ≡ the charge [C] of species s
- ρm = ∑smsns ≡ total mass density [kg cm−3]
- γs ≡ polytropic index or ratio of specific heats [N/A] of species s
- Ts,j ≡ the scalar temperature [eV] of the jth component of species s, j = ∥, ⊥, or tot where ∥(⊥) is parallel(perpendicular) with respect to Bo (see Equation A1a)
- Ps,j = ns kB $T_{s,j}$ ≡ the partial thermal pressure [eV cm^{-3}] of the jth component of species s
- $P_{t,j} = \sum_s P_{s,j}$ ≡ the total pressure [eV cm^{-3}] of the jth component, summed over all species
- $V_{Ts,j}$ ≡ the most probable thermal speed [km s^{-1}] of a one-dimensional velocity distribution (see Equation A1b)
- $\Omega_{cs} = 2\,\pi\, f_{cs}$ ≡ the angular cyclotron frequency [rad s^{-1}] (see Equation A1c)
- $\omega_{ps} = 2\,\pi\, f_{ps}$ ≡ the angular plasma frequency [rad s^{-1}] (see Equation A1d)
- $\Omega_{lh} = 2\,\pi\sqrt{f_{ce}\; f_{ci}}$ ≡ the angular lower hybrid resonance frequency [rad s^{-1}]
- $\Omega_{uh} = 2\,\pi\sqrt{f_{ce}^2 + f_{pe}^2}$ ≡ the angular upper hybrid resonance frequency [rad s^{-1}]
- λ_{De} ≡ the electron Debye length [m] (see Equation A1e)
- ρ_{cs} ≡ the thermal gyroradius [km] (see Equation A1f) of species s
- λ_s ≡ the inertial length [km] (see Equation A1g) of species s
- $\beta_{s,j}$ ≡ the plasma beta [N/A] of the jth component of species s (see Equation A1h)
- V_A ≡ the Alfvén speed [km s^{-1}] (see Equation A1i)
- C_s ≡ the sound or ion-acoustic sound speed [km s^{-1}] (see Equation A1j)
- V_f ≡ the fast mode speed [km s^{-1}] (see Equation A1l)
- θ_{Bn} ≡ the shock normal angle, that is, the acute reference angle between $\langle \mathbf{B}_o \rangle_{up}$ and the shock normal unit vector [deg]
- $\langle | U_{shn} | \rangle_j$ ≡ the jth region average shock normal speed [km s^{-1}] in the shock rest frame (i.e., the speed of the flow relative to the shock)
- $\langle M_A \rangle_j = \langle | U_{shn} | \rangle_j \,/\, \langle V_A \rangle_j$ ≡ the jth region average Alfvénic Mach number [N/A]
- $\langle M_f \rangle_j = \langle | U_{shn} | \rangle_j \,/\, \langle V_f \rangle_j$ ≡ the jth region average fast mode Mach number [N/A]
- R_E ≡ mean equatorial radius of Earth (~6,378 km)
- R_L ≡ mean equatorial radius of Earth's moon (~1,737 km)
- R_s ≡ mean solar radius (~695,700 km)
- σ_c ≡ normalized cross-helicity, a quantified measure of the imbalance in plasma turbulence (see Equation A1m)
- $\mathbf{z}^{\pm} = \delta\mathbf{v} \pm \delta\mathbf{b}$ ≡ Elsasser variables [km s^{-1}], where $\delta\mathbf{v}$ and $\delta\mathbf{b}$ are the velocity and magnetic field fluctuations, the latter being normalized by $\sqrt{\mu_o n_i M_i}$ to make it akin to an Alfvénic fluctuation speed

where multiple parameters are given in the following equations:

$$T_{s,tot} = \frac{1}{3}\left(T_{s,\parallel} + 2\,T_{s,\perp}\right) \tag{A1a}$$

$$V_{Ts,j} = \sqrt{\frac{2\,k_B\,T_{s,j}}{m_s}} \tag{A1b}$$

$$\Omega_{cs} = \frac{q_s\,B_o}{m_s} \tag{A1c}$$

$$\omega_{ps} = \sqrt{\frac{n_s\,q_s^2}{\varepsilon_o\,m_s}} \tag{A1d}$$

$$\lambda_{De} = \frac{V_{Te,tot}}{\sqrt{2}\ \omega_{pe}} = \sqrt{\frac{\varepsilon_o\ \varepsilon_o\ k_B\ T_{e,tot}}{n_e\ e^2}} \tag{A1e}$$

$$\rho_{cs} = \frac{V_{Ts,tot}}{\Omega_{cs}} \tag{A1f}$$

$$\lambda_s = \frac{c}{\omega_{ps}} \tag{A1g}$$

$$\beta_{s,j} = \frac{2\ \mu_o n_s k_B T_{s,j}}{B_o^2} \tag{A1h}$$

$$V_A = \frac{B_o}{\sqrt{\mu_o n_i M_i}} \tag{A1i}$$

$$C_s^2 = \frac{\partial P}{\partial \rho_m} = \frac{\sum_s \gamma_s P_s}{P_s} \rho_m \tag{A1j}$$

$$2\ V_f^2 = \left(C_s^2 + V_A^2\right) \tag{A1k}$$

$$+ \sqrt{\left(C_s^2 - V_A^2\right)^2 + 4\ C_s^2 V_A^2 \sin^2 \theta_{Bn}} \tag{A1l}$$

$$\sigma_c = 2 \frac{\langle \delta \mathbf{v} \cdot \delta \mathbf{b} \rangle}{\langle \delta \mathbf{v}^2 + \delta \mathbf{b}^2 \rangle} \tag{A1m}$$

Appendix B: Instability and Wave Definitions and Summary

In this appendix, we briefly summarize some of the most commonly investigated kinetic plasma instabilities and waves in the IPM to provide context and reference for the reader. Although not all of these are discussed in Section 3.7.2, *Wind* data have been used to examine each of these instabilities in multiple different regions of space. Therefore, we provide the comprehensive list for reference. We use the phrase "driven unstable" to mean the free energy was sufficiently above the growth threshold for the electric or magnetic fluctuations to grow in amplitude. The instabilities and/or waves are as follows in no particular order:

- **Firehose Instability:** The firehose mode can be driven unstable by temperature anisotropies (i.e., $T_{s,\perp} < T_{s,\|}$) in both electrons (Gary & Nishimura, 2003) and ions (Bale et al., 2009; Gary et al., 1976; Hellinger et al., 2006; Maruca et al., 2012). These are not typically observed with in situ time series data but more so inferred by statistical trends limiting $T_{s,\perp}/T_{s,\|}$.
    - **Electron Firehose Instability:** The electron firehose mode can be both resonant and nonresonant with the electrons (Gary & Nishimura, 2003). It either propagates along $\mathbf{B}_o$ and is left-hand polarized (with respect to $\mathbf{B}_o$), or it is nonpropagating (i.e., the real part of its frequency is zero) with $\mathbf{k}$ oblique to $\mathbf{B}_o$ and nearly linearly polarized.
    - **Ion Firehose Instability:** The ion firehose mode can be both resonant and nonresonant with the ions but can only experience a nonresonant, cyclotron-like interaction with the electrons (Gary et al., 1998). The mode is right-hand polarized (with respect to $\mathbf{B}_o$) and the wave vector is oriented nearly along $\mathbf{B}_o$ in the linear regime but can become oblique when nonlinear.

- **Mirror Modes**: The mirror mode can be driven unstable by temperature anisotropies (i.e., $T_{s,\perp} > T_{s,\|}$) in both electrons (Gary & Karimabadi, 2006) and ions (Chen et al., 2016; Gary et al., 1976; Hellinger et al., 2006). In the linear stage mirror modes are purely growing modes, that is, the real part of their frequency is zero so they do not propagate. They also show an anti-correlation between δB and δB. In the nonlinear regime, the mirror mode can propagate and $\mathbf{k}$ can be obliquely oriented with respect to $\mathbf{B}_o$. In linear kinetic theory, mirror modes are always oblique and only in fluid theories is $\mathbf{k}$ exactly orthogonal to $\mathbf{B}_o$. In time series they are usually seen as local decreases in the magnitude of $\mathbf{B}_o$ and less commonly as enhancements.
  - **Electron Mirror Mode:** The electron mirror mode is a nonpropagating mode with wave vector oriented obliquely to $\mathbf{B}_o$ and has $k\ c/\omega_{pe} < 1$.
  - **Ion Mirror Mode:** The ion mirror mode is a nonpropagating mode with wave vector oriented obliquely to $\mathbf{B}_o$ and has $k\ \rho_{cp} < 1$.
- **ICWs:** Electromagnetic ion cyclotron waves (EMIC), ion cyclotron waves (ICWs), proton cyclotron waves (PCWs), or Alfvén/ion cyclotron (AIC) waves are linear or left-hand polarized (with respect to $\mathbf{B}_o$) modes that propagate small angles to $\mathbf{B}_o$. They have rest frame frequencies below the local f_{cp} in the solar wind and typically satisfy $k\ c/\omega_{pp} \sim 0.2$–$0.6$ (He, Wang, et al., 2015; He, Pei, et al., 2015; Wicks et al., 2016). They can be driven unstable by temperature anisotropies (Gary et al., 1976) or ion beams (Gary et al., 1981; Wicks et al., 2016). These waves can reach amplitudes in excess of > 10 mV/m and > 2 nT in the solar wind.
- **LHWs:** Electrostatic (or electromagnetic) lower hybrid waves (or lower hybrid drift or lower hybrid drift instability) are typically linearly polarized electrostatic (i.e., $\mathbf{k} \times \mathbf{B}_o = 0$) waves propagating perpendicular to $\mathbf{B}_o$. When obliquely propagating, they become a right-hand circularly polarized electromagnetic mode and lie on the same branch of the dispersion relation as fast/magnetosonic-whistler mode waves (Davidson & Gladd, 1975; Huba & Wu, 1976; Lemons & Gary, 1978; Marsch & Chang, 1983; Wu et al., 1983, 1984). The typical free energy sources include but are not limited to electric currents (Lemons & Gary, 1978), gradient drifts (Davidson & Gladd, 1975; Huba & Wu, 1976; Lemons & Gary, 1978), the modified two-stream instability (Wu et al., 1983, 1984), and/or heat flux carrying electrons (Marsch & Chang, 1983). In time series in situ data these waves look like modulated sine waves in the perpendicular electric field for the electrostatic version and much less well defined electric and magnetic fluctuations when electromagnetic (Walker et al., 2008; Wilson III, Koval, Szabo, et al., 2013). The electrostatic fluctuations tend to remain below the local lower hybrid resonance frequency, $f_{lh} = \sqrt{f_{ce}\ f_{ci}}$, while the electromagnetic fluctuations can extend to well above f_{lh} (Walker et al., 2008; Wilson III, Koval, Szabo, et al., 2013). These waves can reach amplitudes in excess of >30 mV/m and >20 nT in space plasmas.
- **Magnetosonic-whistler Waves**: These are the electromagnetic version of electrostatic LHWs discussed above and are sometimes called electromagnetic lower hybrid waves, whistler precursors, "1 Hz waves" and/or ULF waves in the terrestrial foreshock. They are part of the MHD fast mode branch of the dispersion relation. They are right-hand polarized (with respect to $\mathbf{B}_o$), obliquely propagating modes with wave normal angles satisfying $10° \lesssim \theta_{kB} \lesssim 60°$, wavenumbers satisfying $0.02 \lesssim k\ \rho_{ce} \lesssim 3.0$, spacecraft frame frequencies near 1 AU satisfying 0.01 Hz $\lesssim f_{sc} \lesssim$ 7.0 Hz, and rest frame frequencies near 1 AU satisfying $0.01 \lesssim \frac{f_{rest}}{f_{cp}} \lesssim 38$ (Wilson, Koval, Szabo, et al., 2013; Wilson, 2016; Wilson et al., 2017).

  The instabilities responsible for radiating these modes can be driven unstable by shock-reflected ions (Wilson et al., 2012; Wu et al., 1983) and/or heat heat flux carrying electrons (Marsch & Chang, 1983; Verscharen, Chandran, et al., 2019). These modes can also be directly radiated through a process called dispersive radiation (Krasnoselskikh et al., 2002; Tidman & Northrop, 1968; Wilson et al., 2009, 2017), whereby the temporally and spatially varying magnetic fields and currents in the nonlinearly steepening collisionless shock ramp radiate electromagnetic fluctuations on the fast/magnetosonic-whistler branch of the dispersion relation. They are observed with in situ time series data as modulated sine waves at low amplitudes and can exhibit soliton-like pulsations at large amplitudes (Wilson et al., 2012; Wilson, Koval, Szabo, et al., 2013; Wilson, Koval, Sibeck, et al., 2013; Wilson et al., 2017). These waves can reach amplitudes in excess of > 30 mV/m and >20 nT in space plasmas.

- **Whistler Waves:** Electromagnetic whistler mode waves (or whistler waves or whistlers or lion roars or chorus or hiss) are right-hand polarized with respect to $\mathbf{B}_o$ and dispersive (i.e., phase speed depends upon the wavenumber) (Hull et al., 2012; Santolík et al., 2003, 2014). They are radiated by instabilities driven unstable by the temperature anisotropy of hot electrons or heat flux carrying electrons (Tong et al., 2019; Vasko et al., 2019; Verscharen, Chandran, et al., 2019; Wilson et al., 2009, 2020a; Wilson, Koval, Szabo, et al., 2013). They tend to have rest frame frequencies satisfying $\omega_{lh} \ll \omega < \omega_{ce}$ and wavenumbers satisfying $k\, c/\omega_{pe} \sim 0.2$–$1.0$ or $k\, \rho_{ce} \sim 0.2$–0.8 (Stansby et al., 2016; Wilson III, Koval, Szabo, et al., 2013). These waves can reach amplitudes in excess of $>$ 300 mV/m and $>$8 nT in space plasmas.
- **ESWs:** Electrostatic solitary waves (or BGK phase space holes or electron/ion holes or solitary waves) are linearly polarized electrostatic structures that exhibit a bipolar(unipolar) electric field pulse parallel (perpendicular) to $\mathbf{B}_o$ with $\lambda \gtrsim 2\, \pi\, \lambda_{De}$ (Bale, Kellogg, Larson, et al., 1998; Breneman et al., 2013; Cattell et al., 2003, 2005; Franz et al., 2005; Malaspina et al., 2013; Vasko et al., 2018; Wilson et al., 2007, 2010). They can propagate along the quasi-static magnetic field at fractions of V_{Te} (Cattell et al., 2005; Franz et al., 2005) or obliquely to the field and at much lower speeds (Vasko et al., 2018). These waves can reach amplitudes in excess of $>$1,000 mV/m in space plasmas.
- **IAWs:** Electrostatic ion acoustic waves (or ion sound waves) are linearly polarized (parallel to $\mathbf{B}_o$) electrostatic (i.e., $\mathbf{k} \times \mathbf{B}_o = 0$) waves with $\lambda \gtrsim 2\, \pi\, \lambda_{De}$ (Breneman et al., 2013; Fuselier & Gurnett, 1984; Gurnett, Neubauer, & Schwenn, 1979; Gurnett, Marsch, et al., 1979; Wilson et al., 2007, 2010). The time series present as symmetric (about zero) electric field oscillations in the form of modulated sine waves with spacecraft frame frequencies near 1 AU satisfying few 100 Hz $\lesssim f_{sc} \lesssim$ 10 kHz. Near collisionless shock waves in space plasmas, these waves can reach amplitudes in excess of $>$ 300 mV/m.
- **ECDI:** The electron cyclotron drift instability (Forslund et al., 1970, 1972) or beam cyclotron instability (Lampe, Manheimer, et al., 1971; Lampe, McBride, et al., 1971) or electrostatic electron-ion streaming instability (Wong, 1970) occurs upstream of collisionless shocks due to the relative drift between incident electrons and shock-reflected ions (Forslund et al., 1970; Muschietti & Lembège, 2013, 2017). They are observed as electrostatic fluctuations with mixtures of IAW and electron cyclotron harmonics. That is, the power spectrum shows a broad acoustic spectrum expected for IAWs and superposed are integer and/or half-integer harmonics of f_{ce}. The polarizations shown in hodogram plots can look like "tadpoles" or "tear drops." The time series present as asymmetric (about zero) electric field oscillations in both the parallel and perpendicular (with respect to $\mathbf{B}_o$) components (Breneman et al., 2013; Wilson et al., 2010). These waves can reach amplitudes in excess of $>$300 mV/m in space plasmas.
- **Langmuir Waves:** Langmuir waves can be both linearly (electrostatic) and elliptically (electromagnetic) polarized and are driven unstable by electron beams (e.g., "bump-on-tail" instability). The time series signature is a modulated sine wave with spacecraft frame frequencies near f_{pe} (Bale et al., 1996, 1997; Bale, Kellogg, Goetz, & Monson, 1998; Kellogg, Monson, et al., 1996; Malaspina & Ergun, 2008; Malaspina et al., 2011). In space plasmas, they are often large amplitude with some in excess of $>$500 mV/m.

Table C1
A Selection of Wind Databases First Published Between 2013 and 2020

Year	Title	Citation & URL
2020	*Wind* WAVES TDSF Dataset	Wilson (2020) https://doi.org/10.5281/zenodo.3911205
2020	Supplement to: Electron energy partition across interplanetary Shocks: III. Analysis	Wilson et al. (2020b) https://doi.org/10.5281/zenodo.3627284
2020	Radial Evolution of Coronal Mass Ejections Between MESSENGER, & Venus Express, STEREO, and L1: Catalog and Analysis	Salman et al. (2020) https://doi.org/10.1029/2019JA027084
2019	Supplement to: Electron energy partition across interplanetary shocks	Wilson et al. (2019c) https://doi.org/10.5281/zenodo.2875806

Table C1
Continued

Year	Title	Citation & URL
2019	A Catalog of Type II radio bursts observed by *Wind*/WAVES and their Statistical Properties	Gopalswamy, Mäkelä, and Yashiro (2019) https://cdaw.gsfc.nasa.gov/CME_list/radio/waves_type2.html
2018	A database of small-scale magnetic flux ropes in the solar wind from *Wind* spacecraft measurements	Hu et al. (2018) https://doi.org/10.1088/1742–6596/1100/1/012012
2018	*Wind* ICME Catalog	Nieves-Chinchilla et al. (2018) https://wind.nasa.gov/ICMEindex.php
2018	The *Wind*/EPACT Proton Event Catalog	Miteva et al. (2018) http://www.stil.bas.bg/SEPcatalog/
2017	The KONUS-*Wind* GRB Catalog with known Redshifts	Tsvetkova et al. (2017) http://www.ioffe.ru/LEA/zGRBs/triggered/
2017	Interactive Multi-instrument Database of Solar Flares	Sadykov et al. (2017) https://solarflare.njit.edu
2016	The 2nd KONUS-*Wind* Catalog of sGRBs	Svinkin et al. (2016) http://www.ioffe.ru/LEA/shortGRBs/Catalog/
2016	*Wind* Dust Impact Database	Malaspina and Wilson (2016) https://cdaweb.gsfc.nasa.gov/index.html/
2014	Catalog of High-Speed Solar Wind Streams during Solar Cycle 23	Xystouris et al. (2014) https://doi.org/10.1007/s11207-013-0355-z
2014	KONUS-*Wind* Solar Flares	Pal'shin et al. (2014) http://www.ioffe.ru/LEA/Solar/
2013	Interplanetary Network Localizations of sGRBs	Pal'shin et al. (2013) https://doi.org/10.1088/0067-0049/207/2/38

Appendix C: Wind Databases

This appendix provides a single reference table listing the databases relying upon *Wind* databases created between 2013 to 2020. The limited scope of Table C1 is partly for brevity's sake and partly due to the difficulty in documenting/referencing older databases (e.g., nonfunctional URLs and/or a lack of a working DOI).

Glossary

AE-Index An index designed to provide a global, quantitative measure of auroral zone magnetic activity produced by enhanced ionospheric currents.

Alpha-particle A doubly charged ion that is the nucleus of a ^{4}He atom.

Astronomical Unit Roughly the distance between the Earth and sun called 1 AU. Originally it was defined as the average distance between the two bodies but was defined as exactly 149,597,870,700 m (or ~149.6 million kilometers or ~92.96 million miles) in 2012.

Bow Shock Shock wave standing upstream of a obstacle/piston in an incident, supersonic flow. In a plasma, this only occurs upstream of magnetized planetary bodies.

Carrington rotation An approximate time scale over which the photosphere (i.e., optical surface of the Sun) at low latitudes rotates through 2π radians. Richard C. Carrington determined this rate watching sun spots in the 1850s and arrived at a sidereal rotation period of ~23.38 days (1 day = 86,400 s). Since sidereal rotation is relative to fixed stars and Earth orbits the sun, a Carrington rotation observed from Earth is ~27.2753 days.

Collisionless Shock A shock wave where the ramp region, or region of sharpest parameter gradients, spatial scale is orders of magnitude smaller than the mean free Coulomb collisional path. Anecdotally, the mean free path of a thermal proton near Earth is roughly 1 AU while the typical shock ramp thickness only several kilometers to a few tens of kilometers.

Coronal Hole Regions in which the magnetic field lines do not connect back to the solar surface but rather are directed outward into the IPM.

Coronal Mass Ejection Eruptions of plasma from the solar corona that are some of the largest (energetically) phenomena in the solar system. When moving out though the IPM, they are called interplanetary coronal mass ejections or ICMEs.

Corotating Interaction Region The compressed plasma region that corotates with the Sun formed along the leading edge of a fast solar wind stream from a coronal hole as it interacts with preceding slower solar wind. Some reseachers require that the CIR is observed at least twice to distinguish it from a "stream interaction region" (SIR). Shock waves can develop along the CIR boundaries, usually beyond 1 AU, mostly due to the expansion speed of the CIR relative to the ambient plasma. This becomes more favorable at larger heliocentric distances.

Cyclotron Frequency The rate at which a charged particle orbits a magnetic field. It is also called the gyrofrequency.

Cyclotron Resonance Condition where an electric field oscillates at the same rate as the particle gyrofrequency in the particle guiding center rest frame resulting in energy gain/loss, depending upon whether the oscillations are damping/growing.

Critical Balance A conjecture of turbulence models in which the linear and nonlinear timescales of the system remain comparable at all scales in the inertial range.

Debye Length The maximum distance any single charged particle's electric field can influence other charged particles in a plasma. This is often referred to in terms of the electrostatic screening or shielding because for scales larger than the Debye length, only wave and convective electric fields tend to persist.

Dispersion Relation The function that defines the relationship between the frequency and wavenumber, that is, $\omega = \omega\left(\mathbf{k}\right)$.

Dispersive Radiation The process through which an electromagnetic emission is generated due to temporally and spatially varying currents with the fluctuation frequencies having an explicit dependence upon the wavenumber. These phenomena typically occur in the magnetic ramp of collisionless shocks, which are nonlinearly steepened fast/magnetosonic-whistler waves. Thus, the radiated waves are on the fast/magnetosonic-whistler branch of the dispersion relation.

Dispersive Wave Any fluctuation that has an explicit wavenumber dependence in its frequency, that is, $\omega = \omega\left(\mathbf{k}\right)$.

Disruption Scale The spatial scale at which the reconnection timescale becomes faster than the turbulent eddy timescale resulting in a reconnection dominated Cascade Range.

Dissipation Range The range of scales in a turbulent medium where dissipation dominates over the energy cascade, usually at the smallest scales. Note that this term has become less relevant and been replaced by just kinetic range.

Dust Dust here refers to particles ranging in size from nanometers to several micrometers (microns) originating either with the interplanetary medium (IPD) or from the interstellar medium (ISD).

Dst Index The Disturbance Storm-Time (Dst) index is a measure of space weather, specifically measuring the strength of the ring current of ions around the Earth's equatorial region in the magnetosphere.

Eddy Turnover Time Approximate time scale necessary for a fluid vortex, or eddy, to rotate about its axis of symmetry.

Energetic Storm Particles An enhancement in the energetic particle intensity, typically at energies of tens of keV to ~10 MeV, in the vicinity of an interplanetary shock, usually attributed to local particle acceleration by the shock.

Eulerian Decorrelation Time Timescale over which turbulent fluctuations remain correlated in the Eulerian frame of reference.

Fast Radio Burst These are bright, millisecond-scale radio flashes of currently unconfirmed origin. Some recent observations suggest that magnetars may be the most likely source candidates. They are likely associated with or caused by some cataclysmic astrophysical event as the estimated power associated with them can exceed 10^{35} J s^{-1} or 10^{42} erg s^{-1}, that is, the total solar output for $\sim$3 days.

Foreshock Region upstream of a shock wave in communication with the shock wave through electromagnetic waves and/or backstreaming particles.

Gamma Rays These are photons with energies $>$100 keV. There is no distinct cutoff between gamma rays and x-rays, but they are typically distinguished by their source. X-rays tend to be emitted by accelerating electrons and gamma rays from nuclear processes.

Gamma Ray Burst The brightest electromagnetic events known to occur in the universe, occurring transiently from the collapse of massive stars or coalescence of compact objects (e.g., two neutron stars or a neutron star-black hole merger). They consist of an initial flash of gamma-rays lasting from tens of milliseconds to minutes followed by a longer duration "afterglow" at radio and optical wavelengths.

Giant Flare These are of greater apparent intensity than gamma ray bursts and are very rare, averaging once per decade.

Ground Level Enhancement Solar particle events that extend to sufficiently high ($\sim$GeV) energies that they produce secondary particles in the atmosphere that are detected by ground-based neutron monitors.

Gyrophase The angular description of a particle's gyro orbit about the magnetic field.

Gyroradius The orbital distance of a charged particle's motion about a magnetic field. It is also called the Larmor radius.

Halo Orbit A periodic trajectory around a gravitational Lagrange point that consists of a subset of Lissajous orbits where all three components share the same periodicity.

Heliosphere Region of space dominated by the sun's solar wind bounded by its interaction with the interstellar medium.

Heliospheric Current Sheet The surface that separates the two solar magnetic polarities or hemispheres of the heliosphere.

Inertial Length The distance covered by the speed of light in vacuum during one plasma oscillation. This is also called the skin depth.

Inertial Range The range of scales in a turbulent medium in which the inertial forces dominate resulting in the proposed cascade of energy from larger to smaller scales.

Interplanetary Coronal Mass Ejection A structure in the solar wind observed remotely or in situ formed of material associated with a coronal mass ejection.

Interplanetary Magnetic Field The magnetic field permeating the IPM.

Interplanetary Shock Shock wave propagating in the IPM are generated by either corotating/stream interaction regions or interplanetary coronal mass ejections.

Kinetic Instability Similar to plasma instability defined below, it is a mechanism through which a plasma converts some free energy source into electromagnetic fluctuations. The difference between kinetic and plasma instabilities is that the former specifically refers to features in the VDFs while the latter also encompasses fluid-like instabilities.

Kinetic Range The range of scales in a turbulent plasma comparable to or smaller than the plasma kinetic scales, for example, particle gyroradii, inertial lengths, etc.

Lagrange Point Region of space with a local minimum in the gravitational potential caused between at least two large masses (e.g., Earth and sun).

Landau Resonance Condition where a longitudinal electric field oscillates along the same direction as a particle's velocity at such a rate as to allow the particle to gain/lose energy by effectively "surfing" on the electric potential gradients of the oscillating field. The gain/loss depends upon whether the oscillations are damping/growing much like cyclotron resonance.

Lissajous Orbit A quasi-periodic trajectory around a gravitational Lagrange point. Often, two of the three spatial coordinates of the orbit are stable and coupled to each other while the third is periodically independent.

Magnetar These are rare, young, and isolated neutron stars with extremely strong magnetic fields that can reach up to 10^{11} T or 10^{15} G. These have been confirmed to be the source of SGRs and are a possible candidate source for fast radio bursts.

Magnetic Cloud A structure in an interplanetary coronal mass ejection characterized by an enhanced magnetic field that rotates through a large angle, usually interpreted as evidence for a magnetic flux rope, and low plasma beta.

Magnetic Island Region of space wherein all magnetic field lines are closed either in two- or three-dimensions.

Magnetic Reconnection The process of of a change in the topology of a magnetic field through the destruction of magnetic flux and subsequent conversion to particle kinetic energy.

Magnetohydrodynamics The approximation that the plasma can be represented as a single species fluid model which is scale-invariant. It is often abbreviated as MHD.

Magnetosheath Region between the bow shock and magnetosphere where plasma flow is decelerated and deflected around the magnetosphere of the planetary body.

Magnetosphere Region of space surrounding a magnetized planetary body separated/protected from the incident solar wind by the body's magnetic field.

Magnetotail Region of magnetosphere on opposite side of solar wind incident flow, where the field has been stretched due to the asymmetric pressure (i.e., ram pressure) exerted on the planetary body's magnetic field combined with dayside reconnecting field lines being dragged into the nightside region.

Normal Mode The natural or preferred frequency and wavelength of fluctuations/oscillations of a medium/system.

Phase Space The region in which all possible states of a system can be expressed. In plasma physics and/or kinetic theory, this is usually limited to position and momentum coordinates.

Plasma An ionized gas that exhibits a collective behavior similar to a fluid and is governed by long-range interactions/forces.

Plasma Frequency The fastest rate at which a collection of charged particles can oscillate in the absence of an external driving force. The oscillation is typically considered in the absence of a magnetic field because the frequency only depends upon the charged species density and charge state.

Plasma Instability The mechanism through which a plasma converts some free energy source into electromagnetic fluctuations.

Quasi-perpendicular(parallel) Shock Denoting collisionless shock waves with shock normal angles often considered to be $\geq 45°(<45°)$.

Radiation Belts A region of space surrounding magnetized planetary bodies that contains particles that are much more energetic than in the surrounding medium. The particles are trapped and perform three types of orbital motions: gyration about the magnetic field, bouncing between the two magnetic poles, and drifting around the magnetized planetary body. At Earth, these regions are sometimes called the Van Allen radiation belts or Van Allen belts after their discoverer James Van Allen.

Ring Current An electric current carried by particles on trapped, longitudinal orbits about the Earth near the geomagnetic equator at altitudes of $\sim$3–8 R_E. The particles involved are primarily ions (mostly protons and singly ionized oxygen) with energies $\sim$10–200 keV.

Shock Normal Angle The angle between the upstream magnetic field vector and the outward shock normal unit vector.

Shock Wave A stable discontinuity arising from a nonlinearly steepened compressional wave that has reached a balance between steepening and energy dissipation.

Solar Energetic Particles Temporary enhancements of suprathermal ($\gtrsim$10 keV) to relativistic ($\sim$few GeV) particles following energetic solar events (e.g., flares and coronal mass ejections) that last from hours to several days and include protons, electrons and heavy ions.

Soft Gamma Repeater These are strongly magnetized Galactic neutron stars that emit large bursts of X-rays and gamma-rays at irregular intervals.

Solar Exclusion Zone Region of sky about solar disk where solar radio emissions cause sufficient interference with spacecraft communications to prevent telemetry signal locks.

Solar Flare An abrupt and intense enhancement in ultraviolet to gamma ray electromagnetic radiation from a localized region on the sun. On rare occasions for strong flares, the enhanced, localized emission can occur in the visible frequency range too.

Solar Wind A stream of plasma propagating away from the Sun. It is primarily comprised of electrons, protons, and alpha-particles (and heavier ions), is not in thermal or thermodynamic equilibrium, and flows supersonically.

Stream Interaction Region A corotating interaction region (CIR) that need not be observed on two solar rotations. Also used interchangably with CIR.

Structure Function A statistical measure to describe the typical fluctuation amplitudes as a function of scale in a turbulent medium; a conditioned structure function is a structure function constructed from a selected subset of the turbulent fluctuations.

Suprathermal Particles with kinetic energies above the thermal energy of the medium.

Sustained Gamma Ray Emission A continuum at gamma ray frequencies caused by pion-decay due to interaction with >300 MeV protons.

Taylor's Hypothesis The assumption that any variation in a moving flow is propagating at a speed much slower than the bulk flow of the fluid, thus allowing one to convert time series data into spatial scales.

Taylor Microscale A fundamental scale in a turbulent medium characterizing the spatial size of fluctuation gradients.

Thermal Equilibrium Condition where the particle constituents of a medium are in equipartition of energy (i.e., all have the same temperature) but there can be finite heat fluxes present.

Thermodynamic Equilibrium Condition where the particle constituents of a medium are in equipartition of energy (i.e., all have the same temperature) and there are no heat fluxes present.

Transient Ion Foreshock Phenomena These are large-scale (~1,000 to > 30,000 km), solitary [~5–10 per day and transient] structures with durations of tens of seconds to several minutes. They are driven by instabilities caused by the backstreaming particles forming the foreshock.

Trans-iron Elements These are elements on the periodic table at higher proton number than iron, that is, more than 26 protons.

Turbulence A process in fluids or plasmas characterized by chaotic broadband fluctuations which is modeled by a cascade of energy, usually from large injection scales to small dissipation scales.

Type II Burst A class of solar radio emissions caused by nonthermal electrons accelerated by CME-driven shock waves. They are characterized by their slow frequency drift (i.e., few 100s of kHz per hour) versus time, which is a tracer of the shock speed and the electron number density upstream of the shock.

Type III Burst A class of solar radio emissions caused by nonthermal electrons accelerated during a solar eruption streaming out along the IMF. They are characterized by their fast frequency drift (i.e., MHz per minute) versus time, which is a tracer of the gradient in the interplanetary electron number density.

Type III Storm A class of solar radio emissions caused by nonthermal electrons streaming along local magnetic fields in active regions, but outside of flare or CME eruption sites. They are characterized by broadband (>few MHz), very short duration (i.e., $\lesssim$1–2 min) emissions that occur in rapid succession (typically > 10 per hour).

Type IV Burst A class of solar radio emissions caused by nonthermal electrons trapped in the post-eruption arcades (i.e., half-loop-like arches of intense magnetic field connecting to active regions on the solar surface) in/around a solar flare or CME eruption site. They are characterized by a broadband frequency emission in the several to >10 MHz range, sometimes showing a U-shaped frequency-time profile.

Velocity Distribution Function A function that defines the probability density of particles in phase space. An example is the Maxwell-Boltzmann velocity distribution function.

X-line The region within a magnetic reconnection site of an intense current sheet where magnetic flux is being destroyed, changing the field topology.

X-rays Photons with energies in the range ~124 eV to ~124 keV. These are split into hard and soft ranges, with hard being photons with energies $\gtrsim$5–10 keV.

Acronyms

ACE	Advanced Composition Explorer
ADS	Astrophysics Data System
AE–Index	Auroral Electrojet Index
AIM	Aeronomy of Ice in the Mesosphere
APE	Alpha-Proton-Electron telescope, part of *Wind* EPACT/ELITE
ARTEMIS	Acceleration, Reconnection, Turbulence, and Electrodynamics of the Moon's Interaction with the Sun
AU	Astronomical Unit
CAP	Command and Attitude Processor
CDAWeb	Coordinated Data Analysis Web
CIR	Corotating Interaction Region
CME	Coronal Mass Ejection
DH	Decametric-hectometer
DSCOVR	|Deep Space Climate Observatory
DTR	Digital Tape Recorder
EESA	Electron Electrostatic Analyzer, part of *Wind*3DP
ECDI	Electron Cyclotron Drift Instability
ELITE	Electron-Isotope Telescope system, part of *Wind*EPACT
EPACT	Energetic Particles: Acceleration, Composition, and Transport, the APE-ELITE-IT-LEMT-STEP instrument suite on *Wind* known as EPACT
ESA	ElectroStatic Analyzer European Space Agency
ESA	ElectroStatic Analyzer European Space Agency
ESP	Energetic Storm Particle
ESW	Electrostatic Solitary Wave
eV	electron volt
FC	Faraday Cup, e.g., *Wind*/SWE
FOT	Flight Operations Team
FRB	Fast Radio Burst
GCN	Gamma-ray Coordinates Network
GeV	Giga-electron volt
GF	SGR Giant Flare
GGS	Global Geospace Science
GLE	Ground Level Enhancement
GRB	Gamma Ray Burst
GSE	Geocentric Solar Ecliptic
GSFC	Goddard Space Flight Center
HCS	Heliospheric Current Sheet
HK	House Keeping, i.e., type of engineering data for spacecraft and instruments
HSO	Heliophysics System Observatory
IAW	electrostatic Ion Acoustic Wave
ICME	Interplanetary Coronal Mass Ejection
ICW	Ion Cyclotron Wave
IMAP	Interstellar MApping Probe
IMF	Interplanetary Magnetic Field
INTEGRAL	INTErnational Gamma-Ray Astrophysics Laboratory
IP	Interplanetary
IPD	Interplanetary Dust
IPM	Interplanetary Medium
IPN	Interplanetary GRB Network
ISD	Interstellar Dust
ISTP	International Solar-Terrestrial Physics
IT	Isotope Telescope, part of *Wind* EPACT/ELITE

keV	kilo-electron volt
KONUS	Gamma-Ray Spectrometer, i.e., the *Wind* KONUS instrument
LEMT	Low Energy Matrix Telescopes, part of *Wind* EPACT
LHW	Lower Hybrid Wave
LIGO	Laser Interferometer Gravitational-Wave Observatory
MASS	high-resolution MASS spectrometer, part of *Wind* SMS
MeV	Mega-electron volt
MFI	Magnetic Field Investigation, *Wind* MFI
NASA	National Aeronautics and Space Administration
PESA	Ion (Proton) ESA, part of *Wind* 3DP
PSP	*Parker Solar Probe*
SEP	Solar Energetic Particle
SGR	Soft Gamma Repeater
SGRE	Sustained Gamma–ray Emission
SIR	Stream Interaction Region
SMS	Solar Wind and Suprathermal Ion Composition Experiment, i.e., the SWICS–MASS–STICS instrument suite on *Wind* known as SMS
SOFIE	Solar Occultation For Ice Experiment
SoHO	Solar and Heliospheric Observatory mission
SolO	*Solar Orbiter* mission
SPDF	Space Physics Data Facility
sps	samples per second
SSN	Sunspot number
SST	Solid–State (semi–conductor detector) Telescope
STEP	SupraThermal Energetic Particle Telescope, part of *Wind* EPACT
STICS	SupraThermal Ion Composition Spectrometer, part of *Wind* SMS
Strahl (detector)	electron strahl sensor in *Wind* SWE instrument suite
SWE	Solar Wind Experiment, i.e., the VEIS–Strahl–FC instrument suite on *Wind* known as SWE
SWICS	Solar Wind Ion Composition Spectrometer, part of *Wind* SMS
STEREO	Solar Terrestrial Relations Observatory
THEMIS	Time History of Events and Macroscale Interactions during Substorms
TDS	Time Domain Sampler, part of *Wind* WAVES
TGRS	Transient Gamma–Ray Spectrometer, i.e., the *Wind* TGRS experiment
TIFP	Transient Ion Foreshock Phenomena
TNR	Thermal Noise Receiver, part of *Wind* WAVES
TUA	Tape Unit A
TUB	Tape Unit B
VDF	Velocity Distribution Function
VEIS	Vector Ion–Electron Spectrometers, part of *Wind* SWE

Data Availability Statement

The *Wind* shock database can be found at: https://www.cfa.harvard.edu/shocks/wi_data/ Analysis software for *Wind* data (Wilson, 2021) can be found at: https://github.com/lynnbwilsoniii/wind_3dp_pros, and open-sourced calibration software (Wilson et al., 2021) at: https://github.com/lynnbwilsoniii/Wind_Decom_Code Nearly all *Wind* data are publicly available at: https://cdaweb.gsfc.nasa.gov If not directly available through SPDF/CDAWeb, then data can be accessed indirectly from the *Wind* webpage at: https://wind.nasa.gov

Acknowledgments

Lynn B. Wilson was partially supported by *Wind* MO&DA grants and a Heliophysics Innovation Fund (HIF) grant. Alexandra L. Brosius was supported by NASA Grant 80NSSC20M0189. Christopher H. K. Chen was supported by STFC Ernest Rutherford Fellowship ST/N003748/2 and STFC Consolidated Grant ST/T00018X/1. Daniel Verscharen was supported by STFC Ernest Rutherford Fellowship ST/P003826/1 and STFC Consolidated Grant ST/S000240/1.Ian G. Richardson was partially supported by NASA programs NNH19ZDA001N-HSR and NNH19ZDA001N-LWS. Noe Lugaz was partially supported by NASA Grant 80NSSC19K0831. The authors thank D.L. Turner, M. Henderson, and G. Reeves for useful discussions of the radiation belts. Alexandra L. Brosius was grateful to Robert Candey for insightful discussions about the OPEN program and the GSFC Laboratory for Extraterrestrial Physics. The authors thank the Harvard Smithsonian Center for Astrophysics and the NASA SPDF/CDAWeb team for the interplanetary shock analysis and the *Wind* plasma and magnetic field data, respectively. The authors thank Carlos A. Perez Alanis for providing Figure 13. The authors thank Andrea Verdini for providing Figure 11. The authors thank Don V. Reames for providing Figure 17.

References

Abbott, B. P., Abbott, R., Abbott, T. D., Abraham, S., Acernese, F., Ackley, K., et al. (2019). Search for gravitational-wave signals associated with gamma-ray bursts during the second observing run of advanced LIGO and advanced virgo. *Astrophysical Journal*, *886*(1), 75. https://doi.org/10.3847/1538-4357/ab4b48

Acuña, M. H., Ogilvie, K. W., Baker, D. N., Curtis, S. A., Fairfield, D. H., & Mish, W. H. (1995).The global geospace science program and its investigations. *Space Science Reviews*, *71*, 5–21. https://doi.org/10.1007/BF00751323

Adrian, M. L., Viñas, A. F., Moya, P. S., & Wendel, D. E. (2016). Solar wind magnetic fluctuations and electron non-thermal temperature anisotropy: Survey of wind-SWE-VEIS observations. *The Astrophysical Journal*, *833*, 49. https://doi.org/10.3847/1538-4357/833/1/49

Agapitov, O., Mourenas, D., Artemyev, A., Hospodarsky, G., & Bonnell, J. W. (2019). Time scales for electron quasi-linear diffusion by lower-band chorus waves: The effects of ω_{pe}/Ω_{ce} dependence on geomagnetic activity. *Geophysical Research Letters*, *46*, 6178–6187. https://doi.org/10.1029/2019GL083446

Agapitov, O. V., Dudok de Wit, T., Mozer, F. S., Bonnell, J. W., Drake, J. F., Malaspina, D., et al. (2020). Sunward-propagating Whistler Waves Collocated with Localized Magnetic Field Holes in the Solar Wind: Parker Solar Probe Observations at 35.7 R_s Radii. *The Astrophysical Journal Letters*, *891*(1), L20. https://doi.org/10.3847/2041-8213/ab799c

Aguilar-Rodriguez, E., Gopalswamy, N., MacDowall, R., Yashiro, S., & Kaiser, M. I. (2005). A study of the drift rate of type ii radio bursts at different wavelengths. In B. Fleck, T. H. Zurbuchen, & H. Lacoste, (Eds.), Solar wind 11/soho 16, connecting sun and heliosphere (Vol. 592, p. 393). European Space Agency.

Ala-Mathi, M., Ruohotie, J., Good, S. W., Kilpua, E. K. J., & Lugaz, N. (2020). Spatial coherence of interplanetary coronal mass ejection sheaths at 1 AU. *Journal of Geophysical Research: Space Physics*, *125*, e2020JA028002. https://doi.org/10.1029/2020JA028002

Al-Haddad, N., Nieves-Chinchilla, T., Savani, N. P., Lugaz, N., & Roussev, I. I. (2018). Fitting and reconstruction of thirteen simple coronal mass ejections. *Solar Physics*, *293*, 73. https://doi.org/10.1007/s11207-018-1288-3

Al-Haddad, N., Nieves-Chinchilla, T., Savani, N. P., Möstl, C., Marubashi, K., Hidalgo, M. A., et al. (2013). Magnetic field configuration models and reconstruction methods for interplanetary coronal mass ejections. *Solar Physics*, *284*, 129–149. https://doi.org/10.1007/s11207-013-0244-5

Allen, R. C., Lario, D., Odstrcil, D., Ho, G. C., Jian, L. K., Cohen, C. M. S., et al. (2020). Solar wind streams and stream interaction regions observed by the parker solar probe with corresponding observations at 1 AU. *The Astrophysical Journal - Supplement Series*, *246*(2), 36. https://doi.org/10.3847/1538-4365/ab578f

Alterman, B. L., & Kasper, J. C. (2019). Helium variation across two solar cycles reveals a speed-dependent phase lag. *The Astrophysical Journal Letters*, *879*(1), L6. https://doi.org/10.3847/2041-8213/ab2391

Alterman, B. L., Kasper, J. C., Stevens, M. L., & Koval, A. (2018). A comparison of alpha particle and proton beam differential flows in collisionally young solar wind. *The Astrophysical Journal*, *864*, 112. https://doi.org/10.3847/1538-4357/aad23f

Alves, M. V., Echer, E., & Gonzalez, W. D. (2006). Geoeffectiveness of corotating interaction regions as measured by Dst index. *Journal of Geophysical Research*, *111*, A07S05. https://doi.org/10.1029/2005JA011379

Aptekar, R. L., Butterworth, P. S., Cline, T. L., Frederiks, D. D., Golenetskii, S. V., Il'Inskii, V. N., et al. (2002). General properties of recurrent bursts from SGRs. *Memorie della Societa Astronomica Italiana*, *73*, 485–490.

Aptekar, R. L., Frederiks, D. D., Golenetskii, S. V., Ilynskii, V. N., Mazets, E. P., Panov, V. N., et al. (1995). Konus-W gamma-ray burst experiment for the GGS wind spacecraft. *Space Science Reviews*, *71*, 265–272. https://doi.org/10.1007/BF00751332

Baker, D. N., & Kanekal, S. G. (2008). Solar cycle changes, geomagnetic variations, and energetic particle properties in the inner magnetosphere. *Journal of Atmospheric and Solar-Terrestrial Physic*, *70*(2–4), 195–206. https://doi.org/10.1016/j.jastp.2007.08.031

Bale, S. D., Burgess, D., Kellogg, P. J., Goetz, K., Howard, R. L., & Monson, S. J. (1996). Phase coupling in Langmuir wave packets: Possible evidence of three-wave interactions in the upstream solar wind. *Geophysical Research Letters*, *23*, 109–112. https://doi.org/10.1029/95GL03595

Bale, S. D., Burgess, D., Kellogg, P. J., Goetz, K., & Monson, S. J. (1997). On the amplitude of intense Langmuir waves in the terrestrial electron foreshock. *Journal of Geophysical Research*, *102*, 11281–11286. https://doi.org/10.1029/97JA00938

Bale, S. D., Hull, A., Larson, D. E., Lin, R. P., Muschietti, L., Kellogg, P. J., et al. (2002). Electrostatic turbulence and debye-scale structures associated with electron thermalization at collisionless shocks. *The Astrophysical Journal*, *575*, L25–L28. https://doi.org/10.1086/342609

Bale, S. D., Kasper, J. C., Howes, G. G., Quataert, E., Salem, C., & Sundkvist, D. (2009). Magnetic fluctuation power near proton temperature anisotropy instability thresholds in the solar wind. *Physical Review Letters*, *103*, 211101. https://doi.org/10.1103/PhysRevLett.103.211101

Bale, S. D., Kellogg, P. J., Goetz, K., & Monson, S. J. (1998). Transverse z-mode waves in the terrestrial electron foreshock. *Geophysical Research Letters*, *25*, 9–12. https://doi.org/10.1029/97GL03493

Bale, S. D., Kellogg, P. J., Larson, D. E., Lin, R. P., Goetz, K., & Lepping, R. P. (1998). Bipolar electrostatic structures in the shock transition region: Evidence of electron phase space holes. *Geophysical Research Letters*, *25*, 2929–2932. https://doi.org/10.1029/98GL02111

Bale, S. D., Pulupa, M., Salem, C., Chen, C. H. K., & Quataert, E. (2013). Electron heat conduction in the solar wind: Transition from Spitzer-Härm to the collisionless limit. *The Astrophysical Journal Letters*, *769*, L22. https://doi.org/10.1088/2041-8205/769/2/L22

Bale, S. D., Reiner, M. J., Bougeret, J.-L., Kaiser, M. L., Krucker, S., Larson, D. E., & Lin, R. P. (1999). The source region of an interplanetary type II radio burst. *Geophysical Research Letters*, *26*, 1573–1576. https://doi.org/10.1029/1999GL900293

Barnes, C. W., & Simpson, J. A. (1976). Evidence for interplanetary acceleration of nucleons in corotating interaction regions. *The Astrophysical Journal Letters*, *210*, L91–L96. https://doi.org/10.1086/182311

Bavassano, B., Pietropaolo, E., & Bruno, R. (1998). Cross-helicity and residual energy in solar wind turbulence: Radial evolution and latitudinal dependence in the region from 1 to 5 AU. *Journal of Geophysical Research*, *103*, 6521–6530. https://doi.org/10.1029/97JA03029

Berdichevsky, D., Thejappa, G., Fitzenreiter, R. J., Lepping, R. L., Yamamoto, T., Kokubun, S., et al. (1999). Widely spaced wave-particle observations during GEOTAIL and wind magnetic conjunctions in the Earth's ion foreshock with near-radial interplanetary magnetic field. *Journal of Geophysical Research*, *104*, 463–482. https://doi.org/10.1029/1998JA900018

Berdichevsky, D. B., Farrugia, C. J., Thompson, B. J., Lepping, R. P., Reames, D. V., Kaiser, M. L., et al. (2002). Halo-coronal mass ejections near the 23rd solar minimum: Lift-off, inner heliosphere, and in situ (1 AU) signatures. *Annales Geophysicae*, *20*, 891–916. https://doi.org/10.5194/angeo-20-891-2002

Bochenek, C. D., Ravi, V., Belov, K. V., Hallinan, G., Kocz, J., Kulkarni, S. R., & McKenna, D. L. (2020). A fast radio burst associated with a Galactic magnetar. *Nature*, *587*(7832), 59–62. https://doi.org/10.1038/s41586-020-2872-x

Boldyrev, S. (2006).Spectrum of magnetohydrodynamic turbulence. *Physical Review Letters*, *96*(11), 115002. https://doi.org/10.1103/PhysRevLett.96.115002

Boldyrev, S., Chen, C. H. K., Xia, Q., & Zhdankin, V. (2015). Spectral breaks of alfvénic turbulence in a collisionless plasma. *The Astrophysical Journal*, *806*, 238. https://doi.org/10.1088/0004-637X/806/2/238

Boldyrev, S., & Perez, J. C. (2012). Spectrum of Kinetic-Alfvén turbulence. *The Astrophysical Journal Letters*, *758*(2), L44. https://doi.org/10.1088/2041-8205/758/2/L44

Boldyrev, S., Perez, J. C., Borovsky, J. E., & Podesta, J. J. (2011). Spectral scaling laws in magnetohydrodynamic turbulence simulations and in the solar wind. *The Astrophysical Journal Letters*, *741*, L19. https://doi.org/10.1088/2041-8205/741/1/L19

Borovsky, J. E. (2008). Flux tube texture of the solar wind: Strands of the magnetic carpet at 1 AU?. *Journal of Geophysical Research*, *113*, A08110. https://doi.org/10.1029/2007JA012684

Borovsky, J. E., Delzanno, J. L., Valdivia, J. A., Moya, P. S., Stepanova, M., Birn, J., et al. (2020). Outstanding questions in magnetospheric plasma physics: The pollenzo view. *The Journal of Atmospheric and Solar-Terrestrial Physics*, *208*, 105377. https://doi.org/10.1016/j.jastp.2020.105377

Borovsky, J. E., & Denton, M. H. (2009). Relativistic-electron dropouts and recovery: A superposed epoch study of the magnetosphere and the solar wind. *Journal of Geophysical Research*, *114*, 2201. https://doi.org/10.1029/2008JA013128

Bosqued, J. M., Lormant, N., Rème, H., d'Uston, C., Lin, R. P., Anderson, K. A., et al. (1996). Moon-solar wind interaction: First results from the WIND/3DP experiment. *Geophysical Research Letters*, *23*, 1259–1262. https://doi.org/10.1029/96GL00303

Bothmer, V., & Schwenn, R. (1994). Eruptive prominences as sources of magnetic clouds in the solar wind. *Space Science Reviews*, *70*, 215–220. https://doi.org/10.1007/BF00777872

Bothmer, V., & Schwenn, R. (1996). Signatures of fast CMEs in interplanetary space. *Advances in Space Research*, *17*, 319–322. https://doi.org/10.1016/0273-1177(95)00593-4

Bougeret, J. L., Fainberg, J., & Stone, R. G. (1984). Interplanetary radio storms. I - Extension of solar active regions through the interplanetary medium. *Astronomy & Astrophysics*, *136*, 255–262.

Bougeret, J.-L., Kaiser, M. L., Kellogg, P. J., Manning, R., Goetz, K., Monson, S. J., et al. (1995). Waves: The radio and plasma wave investigation on the wind spacecraft. *Space Science Reviews*, *71*, 231–263. https://doi.org/10.1007/BF00751331

Bougeret, J.-L., Zarka, P., Caroubalos, C., Karlický, M., Leblanc, Y., Maroulis, D., et al. (1998). A shock associated (SA) radio event and related phenomena observed from the base of the solar corona to 1 AU. *Geophysical Research Letters*, *25*, 2513–2516. https://doi.org/10.1029/98GL50563

Bourouaine, S., Verscharen, D., Chandran, B. D. G., Maruca, B. A., & Kasper, J. C. (2013). Limits on alpha particle temperature anisotropy and differential flow from kinetic instabilities: Solar wind observations. *The Astrophysical Journal Letters*, *777*, L3. https://doi.org/10.1088/2041-8205/777/1/L3

Bowen, T. A., Badman, S., Hellinger, P., & Bale, S. D. (2018). Density fluctuations in the solar wind driven by Alfvén wave parametric decay. *The Astrophysical Journal Letters*, *854*, L33. https://doi.org/10.3847/2041-8213/aaabbe

Breneman, A. W., Cattell, C. A., Kersten, K., Paradise, A., Schreiner, S., Kellogg, P. J., et al. (2013). STEREO and Wind observations of intense cyclotron harmonic waves at the Earth's bow shock and inside the magnetosheath. *Journal of Geophysical Research: Space Physics*, *118*, 7654–7664. https://doi.org/10.1002/2013JA019372

Broiles, T. W., Desai, M. I., & McComas, D. J. (2012). Formation, shape, and evolution of magnetic structures in CIRs at 1 AU. *Journal of Geophysical Research*, *117*, 3102. https://doi.org/10.1029/2011JA017288

Bruno, R., & Carbone, V. (2013). The solar wind as a turbulence laboratory. *Living Reviews in Solar Physics*, *10*, 2. https://doi.org/10.12942/lrsp-2013-2

Bruno, R., D'Amicis, R., Bavassano, B., Carbone, V., & Sorriso-Valvo, L. (2007). Magnetically dominated structures as an important component of the solar wind turbulence. *Annales Geophysicae*, *25*, 1913–1927. https://doi.org/10.5194/angeo-25-1913-2007

Bruno, R., Telloni, D., Sorriso-Valvo, L., Marino, R., De Marco, R., & D'Amicis, R. (2019). The low-frequency break observed in the slow solar wind magnetic spectra. *Astronomy & Astrophysics*, *627*, A96. https://doi.org/10.1051/0004-6361/201935841

Bruno, R., & Trenchi, L. (2014). Radial dependence of the frequency break between fluid and kinetic scales in the solar wind fluctuations. *The Astrophysical Journal Letters*, *787*(2), L24. https://doi.org/10.1088/2041-8205/787/2/L24

Burlaga, L., Fitzenreiter, R., Lepping, R., Ogilvie, K., Szabo, A., Lazarus, A., et al. (1998). A magnetic cloud containing prominence material—January 1997. *Journal of Geophysical Research*, *103*, 277. https://doi.org/10.1029/97JA02768

Burlaga, L., Sittler, E., Mariani, F., & Schwenn, R. (1981). Magnetic loop behind an interplanetary shock: Voyager, Helios, and IMP 8 observations. *Journal of Geophysical Research*, *86*, 6673–6684. https://doi.org/10.1029/JA086iA08p06673

Burlaga, L. F. (1988). Magnetic clouds and force-free fields with constant alpha. *Journal of Geophysical Research*, *93*, 7217–7224. https://doi.org/10.1029/JA093iA07p07217

Burlaga, L. F., Plunkett, S. P., & Cyr, S. O. C. (2002). Successive CMEs and complex ejecta. *Journal of Geophysical Research*, *107*(A10), 1266. https://doi.org/10.1029/2001JA000255

Cairns, I. H., Lobzin, V. V., Donea, A., Tingay, S. J., McCauley, P. I., Oberoi, D., et al. (2018). Low altitude solar magnetic reconnection, type III solar radio bursts, and X-ray emissions. *Scientific Reports*, *8*, 1676. https://doi.org/10.1038/s41598-018-19195-3

Cane, H. V. (2003). Near-relativistic solar electrons and type III radio bursts. *The Astrophysical Journal*, *598*, 1403–1408. https://doi.org/10.1086/379007

Cane, H. V., & Erickson, W. C. (2003). Energetic particle propagation in the inner heliosphere as deduced from low-frequency (¡100 kHz) observations of type III radio bursts. *Journal of Geophysical Research*, *108*(A5), 1203. https://doi.org/10.1029/2002JA009488

Cane, H. V., Erickson, W. C., & Prestage, N. P. (2002). Solar flares, type III radio bursts, coronal mass ejections, and energetic particles. *Journal of Geophysical Research*, *107*(A10), 1315. https://doi.org/10.1029/2001JA000320

Cane, H. V., Stone, R. G., Fainberg, J., Stewart, R. T., Steinberg, J. L., & Hoang, S. (1981).Radio evidence for shock acceleration of electrons in the solar corona. *Geophysical Research Letters*, *8*, 1285–1288. https://doi.org/10.1029/GL008i012p01285

Caprioli, D., & Spitkovsky, A. (2014). Simulations of ion acceleration at non-relativistic shocks. I. acceleration efficiency. *The Astrophysical Journal*, *783*, 91. https://doi.org/10.1088/0004-637X/783/2/91

Carrington, R. C. (1859). Description of a singular appearance seen in the sun on September 1, 1859. *Monthly Notices of the Royal Astronomical Society*, *20*, 13–15. https://doi.org/10.1093/mnras/20.1.13

Cattell, C., Dombeck, J., Wygant, J., Drake, J. F., Swisdak, M., Goldstein, M. L., et al. (2005). Cluster observations of electron holes in association with magnetotail reconnection and comparison to simulations. *Journal of Geophysical Research*, *110*, 1211. https://doi.org/10.1029/2004JA010519

Cattell, C., Neiman, C., Dombeck, J., Crumley, J., Wygant, J., Kletzing, C. A., et al. (2003). Large amplitude solitary waves in and near the Earth's magnetosphere, magnetopause and bow shock: Polar and Cluster observations. *Nonlinear Processes in Geophysics*, *10*, 13–26

Cattell, C., Wygant, J. R., Goetz, K., Kersten, K., Kellogg, P. J., von Rosenvinge, T., et al. (2008). Discovery of very large amplitude whistler-mode waves in Earth's radiation belts. *Geophysical Research Letters*, *35*, 1105. https://doi.org/10.1029/2007GL032009

Cattell, C. A., Breneman, A., Goetz, K., Kellogg, P. J., Kersten, K., Wygant, J. R., et al. (2012). Large-amplitude whistler waves and electron acceleration in the Earth's radiation belts: A review of STEREO and wind observations. In D. Summers, I. R. Mann, D. N. Baker, & M. Schulz, (Eds.), Dynamics of the Earth's radiation belts and inner magnetosphere (Vol. 199, pp. 41–51). American Geophysical Union. https://doi.org/10.1029/2012GM001322

Chen, C. H. K. (2016). Recent progress in astrophysical plasma turbulence from solar wind observations. *Journal of Plasma Physics*, *82*(6), 535820602. https://doi.org/10.1017/S0022377816001124

Chen, C. H. K., Bale, S. D., Salem, C. S., & Maruca, B. A. (2013). Residual energy spectrum of solar wind turbulence. *The Astrophysical Journal*, *770*, 125. https://doi.org/10.1088/0004-637X/770/2/125

Chen, C. H. K., Leung, L., Boldyrev, S., Maruca, B. A., & Bale, S. D. (2014). Ion-scale spectral break of solar wind turbulence at high and low beta. *Geophysical Research Letters*, *41*, 8081–8088. https://doi.org/10.1002/2014GL062009

Chen, C. H. K., Mallet, A., Schekochihin, A. A., Horbury, T. S., Wicks, R. T., & Bale, S. D. (2012). Three-dimensional structure of solar wind turbulence. *The Astrophysical Journal*, *758*(2), 120. https://doi.org/10.1088/0004-637X/758/2/120

Chen, C. H. K., Matteini, L., Schekochihin, A. A., Stevens, M. L., Salem, C. S., Maruca, B. A., et al. (2016). Multi-species measurements of the firehose and mirror instability thresholds in the solar wind. *The Astrophysical Journal Letters*, *825*, L26. https://doi.org/10.3847/2041-8205/825/2/L26

Chen, J. H., Schwadron, N. A., Möbius, E., & Gorby, M. (2015). Modeling interstellar pickup ion distributions in corotating interaction regions inside 1 AU. *Journal of Geophysical Research: Space Physics*, *120*, 9269–9280. https://doi.org/10.1002/2014JA020939

Chen, L.-J., Wang, S., Wilson, L. B., Schwartz, S., Bessho, N., Moore, T., et al. (2018). Electron bulk acceleration and thermalization at Earth's quasiperpendicular bow shock. *Physical Review Letters*, *120*(22), 225101. https://doi.org/10.1103/PhysRevLett.120.225101

CHIME/FRB Collaboration, Andersen, B. C., Bandura, K. M., Bhardwaj, M., Bij, A., Boyce, M. M., et al. (2020). A bright millisecond-duration radio burst from a Galactic magnetar. *Nature*, *587*(7832), 54–58. https://doi.org/10.1038/s41586-020-2863-y

Chotoo, K., Schwadron, N. A., Mason, G. M., Zurbuchen, T. H., Gloeckler, G., Posner, A., et al. (2000). The suprathermal seed population for corotating interaction region ions at 1 AU deduced from composition and spectra of H^+, He^{++}, and He^+ observed on Wind. *Journal of Geophysical Research*, *105*, 23107–23122. https://doi.org/10.1029/1998JA000015

Clack, D., Kasper, J. C., Lazarus, A. J., Steinberg, J. T., & Farrell, W. M. (2004). Wind observations of extreme ion temperature anisotropies in the lunar wake. *Geophysical Research Letters*, *310*, L06812. https://doi.org/10.1029/2003GL018298

Cline, T. L., Hurley, K. C., Barthelmy, S., Butterworth, P., Feroci, M., Frontera, F., et al. (2001). The IPN I: From the Past to the Future. In E. Costa, F. Frontera, & J. Hjorth, (Eds.), *Gamma-ray bursts in the afterglow era* (p. 375). Springer. https://doi.org/10.1007/10853853_102

Cliver, E. W., Kahler, S. W., Kazachenko, M., & Shimojo, M. (2019). The disappearing solar filament of 2013 September 29 and its large associated proton event: Implications for particle acceleration at the sun. *The Astrophysical Journal*, *877*(1), 11. https://doi.org/10.3847/1538-4357/ab0e03

Cliver, E. W., Nitta, N. V., Thompson, B. J., & Zhang, J. (2004). Coronal shocks of November 1997 revisited: The Cme type II timing problem. *Solar Physics*, *225*, 105–139. https://doi.org/10.1007/s11207-004-3258-1

Cohen, C. M. S. (2006). *Observations of Energetic Storm Particles: An Overview, Geophysical Monograph Series*. Washington, DC: American Geophysical Union. https://doi.org/10.1029/165GM26

Corona-Romero, P., Gonzalez-Esparza, J. A., & Aguilar-Rodriguez, E. (2013). Propagation of fast coronal mass ejections and shock waves associated with type II radio-burst emission: An analytic study. *Solar Physics*, *285*, 391–410. https://doi.org/10.1007/s11207-012-0103-9

Cremades, H., Iglesias, F. A., Cyr, S. O. C., Xie, H., Kaiser, M. L., & Gopalswamy, N. (2015). Low-frequency type-II radio detections and coronagraph data employed to describe and forecast the propagation of 71 CMEs/shocks. *Solar Physics*, *290*, 2455–2478. https://doi.org/10.1007/s11207-015-0776-y

Dasso, S., Nakwacki, M. S., Démoulin, P., & Mandrini, C. H. (2007). Progressive transformation of a flux rope to an ICME. comparative analysis using the direct and fitted expansion methods. *Solar Physics*, *244*, 115–137. https://doi.org/10.1007/s11207-007-9034-2

Davidson, R. C., & Gladd, N. T. (1975). Anomalous transport properties associated with the lower-hybrid-drift instability. *Physics of Fluids*, *18*, 1327–1335. https://doi.org/10.1063/1.861021

Del Zanna, G., Aulanier, G., Klein, K. L., & Török, T. (2011). A single picture for solar coronal outflows and radio noise storms. *Astronomy & Astrophysics*, *526*, A137. https://doi.org/10.1051/0004-6361/201015231

Démoulin, P., Dasso, S., & Janvier, M. (2013). Does spacecraft trajectory strongly affect detection of magnetic clouds?. *Astronomy & Astrophysics*, *550*, A3. https://doi.org/10.1051/0004-6361/201220535

Démoulin, P., Dasso, S., Janvier, M., & Lanabere, V. (2019). Re-analysis of Lepping's fitting method for magnetic clouds: Lundquist fit reloaded. *Solar Physics*, *294*(12), 172. https://doi.org/10.1007/s11207-019-1564-x

Démoulin, P., Janvier, M., & Dasso, S. (2016). Magnetic flux and helicity of magnetic clouds. *Solar Physics*, *291*, 531–557. https://doi.org/10.1007/s11207-015-0836-3

de Nolfo, G. A., Bruno, A., Ryan, J. M., Dalla, S., Giacalone, J., Richardson, I. G., et al. (2019). Comparing long-duration gamma-ray flares and high-energy solar energetic particles. *The Astrophysical Journal*, *879*(2), 90. https://doi.org/10.3847/1538-4357/ab258f

Desai, M. I., Mason, G. M., Müller-Mellin, R., Korth, A., Mall, U., Dwyer, J. R., & von Rosenvinge, T. T. (2008). The spatial distribution of upstream ion events from the Earth's bow shock measured by ACE, Wind, and STEREO. *Journal of Geophysical Research*, *113*, A08103. https://doi.org/10.1029/2007JA012909

Domingo, V., Fleck, B., & Poland, A. I. (1995). The SOHO mission: An overview. *Solar Physics*, *162*, 1–37. https://doi.org/10.1007/BF00733425

Drake, J. F., Cassak, P. A., Shay, M. A., Swisdak, M., & Quataert, E. (2009). A magnetic reconnection mechanism for ion acceleration and abundance enhancements in impulsive flares. *The Astrophysical Journal Letters*, *700*, L16–L20. https://doi.org/10.1088/0004-637X/700/1/L16

Drake, J. F., & Swisdak, M. (2012). Ion heating and acceleration during magnetic reconnection relevant to the corona. *Space Science Reviews*, *172*(1–4), 227–240. https://doi.org/10.1007/s11214-012-9903-3

Drake, J. F., Swisdak, M., Che, H., & Shay, M. A. (2006). Electron acceleration from contracting magnetic islands during reconnection. *Nature*, *443*, 553–556. https://doi.org/10.1038/nature05116

Ebert, R. W., Desai, M. I., Dayeh, M. A., & Mason, G. M. (2012). Helium ion anisotropies in corotating interaction regions at 1 AU. *The Astrophysical Journal Letters*, *754*, L30. https://doi.org/10.1088/2041-8205/754/2/L30

Ergun, R. E., Larson, D., Lin, R. P., McFadden, J. P., Carlson, C. W., Anderson, K. A., et al. (1998). Wind spacecraft observations of solar impulsive electron events associated with solar type III radio bursts. *The Astrophysical Journal*, *503*, 435. https://doi.org/10.1086/305954

Escoubet, C. P., Schmidt, R., & Goldstein, M. L. (1997). Cluster—Science and mission overview. *Space Science Reviews*, *79*, 11–32. https://doi.org/10.1023/A:1004923124586

Fainberg, J., & Stone, R. G. (1970). Type III solar radio burst storms observed at low frequencies. *Solar Physics*, *15*(1), 222–233. https://doi.org/10.1007/BF00149487

Farrell, W. M., Fitzenreiter, R. J., Owen, C. J., Byrnes, J. B., Lepping, R. P., Ogilvie, K. W., & Neubauer, F. (1996). Upstream ULF waves and energetic electrons associated with the lunar wake: Detection of precursor activity. *Geophysical Research Letters*, *23*, 1271–1274. https://doi.org/10.1029/96GL01355

Farrell, W. M., Kaiser, M. L., & Steinberg, J. T. (1997). Electrostatic instability in the central lunar wake: A process for replenishing the plasma void?. *Geophysical Research Letters*, *24*, 1135–1138. https://doi.org/10.1029/97GL00878

Farrell, W. M., Kaiser, M. L., Steinberg, J. T., & Bale, S. D. (1998). A simple simulation of a plasma void: Applications to Wind observations of the lunar wake. *Journal of Geophysical Research*, *1032*, 23653–23660. https://doi.org/10.1029/97JA03717

Farrugia, C. J., Berdichevsky, D. B., Möstl, C., Galvin, A. B., Leitner, M., Popecki, M. A., et al. (2011). Multiple, distant (40°) in situ observations of a magnetic cloud and a corotating interaction region complex. *The Journal of Atmospheric and Solar-Terrestrial Physics*, *73*, 1254–1269. https://doi.org/10.1016/j.jastp.2010.09.011

Farrugia, C. J., Burlaga, L. F., Osherovich, V. A., Richardson, I. G., Freeman, M. P., Lepping, R. P., & Lazarus, A. J. (1993). A study of an expanding interplanetary magnetic cloud and its interaction with the Earth's magnetosphere: The interplanetary aspect. *Journal of Geophysical Research*, *98*, 7621–7632. https://doi.org/10.1029/92JA02349

Farrugia, C. J., Matsui, H., Kucharek, H., Torbert, R. B., Smith, C. W., Jordanova, V. K., et al. (2005). Interplanetary coronal mass ejection and ambient interplanetary magnetic field correlations during the Sun-Earth connection events of October-November 2003. *Journal of Geophysical Research*, *110*, A09S13. https://doi.org/10.1029/2004JA010968

Farrugia, C. J., Sandholt, P. E., Moen, J., & Arnoldy, R. L. (1998). Unusual features of the January 1997 magnetic cloud and their effect on optical dayside auroral signatures. *Geophysical Research Letters*, *25*, 3051–3054. https://doi.org/10.1029/98GL01226

Filwett, R. J., Desai, M. I., Dayeh, M. A., & Broiles, T. W. (2017). Source population and acceleration location of suprathermal heavy ions in corotating interaction regions. *The Astrophysical Journal*, *838*, 23. https://doi.org/10.3847/1538-4357/aa5ca9

Fishman, G. J. (1995). Gamma-ray bursts: An overview. *Publications of the Astronomical Society of the Pacific*, *107*, 1145. https://doi.org/10.1086/133672

Fishman, G. J., & Meegan, C. A. (1995). Gamma-ray bursts. *The Annual Review of Astronomy and Astrophysics*, *33*, 415–458. https://doi.org/10.1146/annurev.aa.33.090195.002215

Fisk, L. A., & Lee, M. A. (1980). Shock acceleration of energetic particles in corotating interaction regions in the solar wind. *The Astrophysical Journal*, *237*, 620–626. https://doi.org/10.1086/157907

Forslund, D., Morse, R., Nielson, C., & Fu, J. (1972). Electron cyclotron drift instability and turbulence. *Physics of Fluids*, *15*, 1303–1318. https://doi.org/10.1063/1.1694082

Forslund, D. W., Morse, R. L., & Nielson, C. W. (1970). Electron cyclotron drift instability. *Physical Review Letters*, *25*, 1266–1270. https://doi.org/10.1103/PhysRevLett.25.1266

Forsyth, R. J., & Marsch, E. (1999). Solar origin and interplanetary evolution of stream interfaces. *Space Science Reviews*, *89*, 7–20. https://doi.org/10.1023/A:1005235626013

Fox, N. J., Velli, M. C., Bale, S. D., Decker, R., Driesman, A., Howard, R. A., et al. (2015). The solar probe plus mission: Humanity's first visit to our star. *Space Science Reviews*. https://doi.org/10.1007/s11214-015-0211-6

Franz, H., Sharer, P., Ogilvie, K., & Desch, M. (1998). Wind nominal mission performance and extended mission design. In *Aiaa/aas astrodynamics specialist conference and exhibit*. Retrieved from https://arc.aiaa.org/doi/abs/10.2514/6.1998-4467

Franz, J. R., Kintner, P. M., Pickett, J. S., & Chen, L.-J. (2005). Properties of small-amplitude electron phase-space holes observed by Polar. *Journal of Geophysical Research*, *110*, 9212. https://doi.org/10.1029/2005JA011095

Fränz, M., & Harper, D. (2002). Heliospheric coordinate systems. *Planet Space Science*, *50*(2), 217–233. https://doi.org/10.1016/S0032-0633(01)00119-2

Frederiks, D., Svinkin, D., Tsvetkova, A., Aptekar, R., Golenetskii, S., Kozlova, A., et al. (2019). GRB observations with Konus-WIND experiment. *Memorie della Societa Astronomica Italiana*, *90*(1–2), 67–70.

Frederiks, D. D., Golenetskii, S. V., Palshin, V. D., Aptekar, R. L., Ilyinskii, V. N., Oleinik, F. P., et al. (2007). Giant flare in SGR 1806-20 and its Compton reflection from the Moon. *Astronomy Letters*, *33*, 1–18. https://doi.org/10.1134/S106377370701001X

Fuselier, S. A., & Gurnett, D. A. (1984). Short wavelength ion waves upstream of the Earth's bow shock. *Journal of Geophysical Research*, *89*, 91–103. https://doi.org/10.1029/JA089iA01p00091

Gary, S. P. (1993). *Theory of space plasma Microinstabilities*. Cambridge University Press

Gary, S. P., Gosling, J. T., & Forslund, D. W. (1981). The electromagnetic ion beam instability upstream of the Earth's bow shock. *Journal of Geophysical Research*, *86*, 6691–6696. https://doi.org/10.1029/JA086iA08p06691

Gary, S. P., Jian, L. K., Broiles, T. W., Stevens, M. L., Podesta, J. J., & Kasper, J. C. (2016). Ion-driven instabilities in the solar wind: Wind observations of 19 March 2005. *Journal of Geophysical Research: Space Physics*, *121*, 30–41. https://doi.org/10.1002/2015JA021935

Gary, S. P., & Karimabadi, H. (2006). Linear theory of electron temperature anisotropy instabilities: Whistler, mirror, and Weibel. *Journal of Geophysical Research*, *111*, 11224. https://doi.org/10.1029/2006JA011764

Gary, S. P., Li, H., O'Rourke, S., & Winske, D. (1998). Proton resonant firehose instability: Temperature anisotropy and fluctuating field constraints. *Journal of Geophysical Research*, *103*, 14567–14574. https://doi.org/10.1029/98JA01174

Gary, S. P., Montgomery, M. D., Feldman, W. C., & Forslund, D. W. (1976). Proton temperature anisotropy instabilities in the solar wind. *Journal of Geophysical Research*, *81*, 1241–1246. https://doi.org/10.1029/JA081i007p01241

Gary, S. P., & Nishimura, K. (2003). Resonant electron firehose instability: Particle-in-cell simulations. *Physics of Plasmas*, *10*, 3571–3576. https://doi.org/10.1063/1.1590982

Gary, S. P., Scime, E. E., Phillips, J. L., & Feldman, W. C. (1994). The whistler heat flux instability: Threshold conditions in the solar wind. *Journal of Geophysical Research*, *99*, 23391–23399. https://doi.org/10.1029/94JA02067

Glesener, L., & Fleishman, G. D. (2018). Electron acceleration and jet-facilitated escape in an M-class solar flare on 2002 August 19. *The Astrophysical Journal*, *867*, 84. https://doi.org/10.3847/1538-4357/aacefe

Gloeckler, G., Balsiger, H., Bürgi, A., Bochsler, P., Fisk, L. A., Galvin, A. B., et al. (1995). The solar wind and suprathermal ion composition investigation on the wind spacecraft. *Space Science Reviews*, *71*, 79–124. https://doi.org/10.1007/BF00751327

Goldreich, P., & Sridhar, S. (1995). Toward a theory of interstellar turbulence. II. Strong Alfvenic turbulence. *The Astrophysical Journal*, *438*, 763. https://doi.org/10.1086/175121

Good, S. W., Kilpua, E. K. J., LaMoury, A. T., Forsyth, R. J., Eastwood, J. P., & Möstl, C. (2019). Self-similarity of ICME flux ropes: Observations by radially aligned spacecraft in the inner heliosphere. *Journal of Geophysical Research: Space Physics*, *124*, 4960–4982. https://doi.org/10.1029/2019JA026475

Gopalswamy, N. (2004a). Interplanetary radio bursts. In D. E. Gary & C. U. Keller, (Eds.), Astrophysics and space science library (Vol. 314, p. 305). Springer. https://doi.org/10.1007/1-4020-2814-8_15

Gopalswamy, N. (2004b). Recent advances in the long-wavelength radio physics of the Sun. *Planetary and Space Science*, *52*, 1399–1413. https://doi.org/10.1016/j.pss.2004.09.016

Gopalswamy, N. (2006). Properties of interplanetary coronal mass ejections. *Space Science Reviews*, *124*(1–4), 145–168. https://doi.org/10.1007/s11214-006-9102-1

Gopalswamy, N. (2011). Coronal mass ejections and solar radio emissions. In H. O. Rucker, W. S. Kurth, P. Louarn, & G. Fischer, (Eds.), *Planetary, solar and heliospheric radio emissions (pre vii)* (pp. 325–342) Austrian Academy of Sciences Press.

Gopalswamy, N. (2016). *Low-frequency radio bursts and space weather*. arXiv e-prints. arXiv:1605.02218

Gopalswamy, N., Aguilar-Rodriguez, E., Yashiro, S., Nunes, S., Kaiser, M. L., & Howard, R. A. (2005).Type II radio bursts and energetic solar eruptions. *Journal of Geophysical Research*, *110*, A12S07. https://doi.org/10.1029/2005JA011158

Gopalswamy, N., Akiyama, S., Mäkelä, P., Yashiro, S., & Cairns, I. H. (2016). *On the directivity of low-frequency type IV radio bursts*. arXiv e-prints. arXiv:1605.02223

Gopalswamy, N., Akiyama, S., Yashiro, S., Michalek, G., Xie, H., & Mäkelä, P. (2020). *Effect of the Weakened heliosphere in solar cycle 24 on the properties of coronal mass ejections*. arXiv e-prints. arXiv:2007.08291

Gopalswamy, N., Kaiser, M. L., Lepping, R. P., Kahler, S. W., Ogilvie, K., Berdichevsky, D., et al. (1998). Origin of coronal and interplanetary shocks - A new look with WIND spacecraft data. *Journal of Geophysical Research*, *103*, 307. https://doi.org/10.1029/97JA02634

Gopalswamy, N., Kaiser, M. L., Thompson, B. J., Burlaga, L. F., Szabo, A., Vourlidas, A., et al. (2000). Radio-rich solar eruptive events. *Geophysical Research Letters*, *27*, 1427. https://doi.org/10.1029/1999GL003665

Gopalswamy, N., & Mäkelä, P. (2010). Long-duration low-frequency type III bursts and solar energetic particle events. *The Astrophysical Journal*, *721*, L62–L66. https://doi.org/10.1088/2041-8205/721/1/L62

Gopalswamy, N., & Mäkelä, P. (2011). Low-frequency type III radio bursts and solar energetic particle events. *Central European Astrophysical Bulletin*, *35*, 71–82.

Gopalswamy, N., Mäkelä, P., Akiyama, S., Yashiro, S., Xie, H., & Thakur, N. (2018). Sun-to-earth propagation of the 2015 June 21 coronal mass ejection revealed by optical, EUV, and radio observations. *The Journal of Atmospheric and Solar-Terrestrial Physics*, *179*, 225–238. https://doi.org/10.1016/j.jastp.2018.07.013

Gopalswamy, N., Mäkelä, P., Akiyama, S., Yashiro, S., Xie, H., Thakur, N., & Kahler, S. W. (2015). Large solar energetic particle events associated with filament eruptions outside of active regions. *The Astrophysical Journal*, *806*, 8. https://doi.org/10.1088/0004-637X/806/1/8

Gopalswamy, N., Mäkelä, P., & Yashiro, S. (2019). A catalog of type II radio bursts observed by Wind/WAVES and their statistical properties. *Sun and Geosphere*, *14*, 111–121. https://doi.org/10.31401/SunGeo.2019.02.03

Gopalswamy, N., Mäkelä, P., Yashiro, S., Lara, A., Akiyama, S., & Xie, H. (2019). On the shock source of sustained gamma-ray emission from the sun. *Journal of Physics: Conference Series*, *1332*. https://doi.org/10.1088/1742-6596/1332/1/012004

Gopalswamy, N., Mäkelä, P., Yashiro, S., Lara, A., Xie, H., Akiyama, S., & MacDowall, R. J. (2018). Interplanetary type II radio bursts from Wind/WAVES and sustained gamma-ray emission from Fermi/LAT: Evidence for shock source. *The Astrophysical Journal Letters*, *868*, L19. https://doi.org/10.3847/2041-8213/aaef36

Gopalswamy, N., Mäkelä, P., Yashiro, S., Thakur, N., Akiyama, S., & Xie, H. (2017). A hierarchical relationship between the fluence spectra and CME kinematics in large solar energetic particle events: A radio perspective. *Journal of Physics Conference Series*, *900*, 012009. https://doi.org/10.1088/1742-6596/900/1/012009

Gopalswamy, N., Xie, H., Yashiro, S., Akiyama, S., Mäkelä, P., & Usoskin, I. G. (2012). Properties of ground level enhancement events and the associated solar eruptions during solar cycle 23. *Space Science Reviews*, *171*, 23–60. https://doi.org/10.1007/s11214-012-9890-4

Gopalswamy, N., Yashiro, S., Kaiser, M. L., Howard, R. A., & Bougeret, J. L. (2001). Characteristics of coronal mass ejections associated with long-wavelength type II radio bursts. *Journal of Geophysical Research*, *106*(A12), 29219–29230. https://doi.org/10.1029/2001JA000234

Gopalswamy, N., Yashiro, S., Thakur, N., Mäkelä, P., Xie, H., & Akiyama, S. (2016). The 2012 July 23 backside eruption: An extreme energetic particle event? *The Astrophysical Journal*, *833*, 216. https://doi.org/10.3847/1538-4357/833/2/216

Gopalswamy, N., Yashiro, S., Xie, H., Akiyama, S., & Mäkelä, P. (2015). Properties and geoeffectiveness of magnetic clouds during solar cycles 23 and 24. *Journal of Geophysical Research: Space Physics*, *120*, 9221–9245. https://doi.org/10.1002/2015JA021446

Gordley, L. L., Hervig, M. E., Fish, C., Russell, I., James, M., Bailey, S., Cook, J., et al. (2009).The solar occultation for ice experiment. *The Journal of Atmospheric and Solar-Terrestrial Physics*, *71*(3–4), 300–315. https://doi.org/10.1016/j.jastp.2008.07.012

Gosling, J. T. (2007). Observations of magnetic reconnection in the turbulent high-speed solar wind. *The Astrophysical Journal*, *671*, L73–L76. https://doi.org/10.1086/524842

Gosling, J. T. (2010). Magnetic reconnection in the Solar Wind: An update. *Twelfth International Solar Wind Conference*, *1216*, 188–193. https://doi.org/10.1063/1.3395833

Gosling, J. T. (2011). Magnetic reconnection in the solar wind. *Space Science Reviews*, *104*. https://doi.org/10.1007/s11214-011-9747-2

Gosling, J. T., Bame, S. J., McComas, D. J., & Phillips, J. L. (1990). Coronal mass ejections and large geomagnetic storms. *Geophysical Research Letters*, *17*, 901–904. https://doi.org/10.1029/GL017i007p00901

Gosling, J. T., Eriksson, S., Blush, L. M., Phan, T. D., Luhmann, J. G., McComas, D. J., et al. (2007). Five spacecraft observations of oppositely directed exhaust jets from a magnetic reconnection X-line extending $> 4.26 \times 10^6$ km in the solar wind at 1 AU. *Geophysical Research Letters*, *342*, L20108. https://doi.org/10.1029/2007GL031492

Gosling, J. T., Eriksson, S., Phan, T. D., Larson, D. E., Skoug, R. M., & McComas, D. J. (2007). Direct evidence for prolonged magnetic reconnection at a continuous x-line within the heliospheric current sheet. *Geophysical Research Letters*, *340*, 6102. https://doi.org/10.1029/2006GL029033

Gosling, J. T., Phan, T. D., Lin, R. P., & Szabo, A. (2007). Prevalence of magnetic reconnection at small field shear angles in the solar wind. *Geophysical Research Letters*, *341*, 15110. https://doi.org/10.1029/2007GL030706

Gosling, J. T., & Szabo, A. (2008). Bifurcated current sheets produced by magnetic reconnection in the solar wind. *Journal of Geophysical Research*, *113*, A10103. https://doi.org/10.1029/2008JA013473

Grandin, M., Aikio, A. T., & Kozlovsky, A. (2019). Properties and geoeffectiveness of solar wind high-speed streams and stream interaction regions during solar cycles 23 and 24. *Journal of Geophysical Research: Space Physics*, *124*, 3871–3892. https://doi.org/10.1029/2018JA026396

Grappin, R., Leorat, J., & Pouquet, A. (1983). Dependence of MHD turbulence spectra on the velocity field-magnetic field correlation. *Astronomy & Astrophysics*, *126*, 51–58.

Guiriec, S., Gehrels, N., McEnery, J., Kouveliotou, C., & Hartmann, D. H. (2017). Photospheric emission in the joint GBM and Konus prompt spectra of GRB 120323A. *The Astrophysical Journal*, *846*, 138. https://doi.org/10.3847/1538-4357/aa81c2

Gurnett, D. A., Marsch, E., Pilipp, W., Schwenn, R., & Rosenbauer, H. (1979). Ion acoustic waves and related plasma observations in the solar wind. *Journal of Geophysical Research*, *84*, 2029–2038. https://doi.org/10.1029/JA084iA05p02029

Gurnett, D. A., Neubauer, F. M., & Schwenn, R. (1979). Plasma wave turbulence associated with an interplanetary shock. *Journal of Geophysical Research*, *84*, 541–552. https://doi.org/10.1029/JA084iA02p00541

Haggerty, D. K., & Roelof, E. C. (2002). Impulsive near-relativistic solar electron events: Delayed injection with respect to solar electromagnetic emission. *The Astrophysical Journal*, *579*, 841–853. https://doi.org/10.1086/342870

Halekas, J. S., Angelopoulos, V., Sibeck, D. G., Khurana, K. K., Russell, C. T., Delory, G. T., et al. (2011). First results from ARTEMIS, a new two-spacecraft lunar mission: Counter-streaming plasma populations in the lunar wake. *Space Science Reviews*, *95*. https://doi.org/10.1007/s11214-010-9738-8

Halekas, J. S., & Brain, D. A., (2015). Moon's plasma wake. In Moon's plasma wake. A. Keiling C. M. Jackman & P. A. Delamere (Eds.), *Magnetotails in the Solar System*, Geophysical Monograph Series (Vol. 207, pp. 149–167). American Geophysical Union. https://doi.org/10.1002/9781118842324.ch9

Halekas, J. S., Saito, Y., Delory, G. T., & Farrell, W. M. (2011). New views of the lunar plasma environment. *Planetary and Space Science*, *59*(14), 1681–1694. https://doi.org/10.1016/j.pss.2010.08.011

Halford, A. J., McGregor, S. L., Murphy, K. R., Millan, R. M., Hudson, M. K., Woodger, L. A., et al. (2015). BARREL observations of an ICME-shock impact with the magnetosphere and the resultant radiation belt electron loss. *Journal of Geophysical Research: Space Physics*, *120*, 2557–2570. https://doi.org/10.1002/2014JA020873

Harten, R., & Clark, K. (1995).). The design features of the GGS wind and polar spacecraft. *Space Science Reviews*, *71*, 23–40. https://doi.org/10.1007/BF00751324

He, J., Pei, Z., Wang, L., Tu, C., Marsch, E., Zhang, L., & Salem, C. (2015). Sunward propagating Alfvén waves in association with sunward drifting proton beams in the solar wind. *The Astrophysical Journal*, *805*, 176. https://doi.org/10.1088/0004-637X/805/2/176

He, J., Wang, L., Tu, C., Marsch, E., & Zong, Q. (2015). Evidence of Landau and cyclotron resonance between protons and kinetic waves in solar wind turbulence. *The Astrophysical Journal Letters*, *800*, L31. https://doi.org/10.1088/2041-8205/800/2/L31

He, J., Wang, Y., & Sorriso-Valvo, L. (2019). Unified quantitative description of solar wind turbulence intermittency in both inertial and kinetic ranges. *The Astrophysical Journal*, *873*(1), 80. https://doi.org/10.3847/1538-4357/ab03d0

Hellinger, P., & Trávníček, P. (2006). Parallel and oblique proton fire hose instabilities in the presence of alpha/proton drift: Hybrid simulations. *Journal of Geophysical Research*, *111*, A01107. https://doi.org/10.1029/2005JA011318

Hellinger, P., Trávníček, P., Kasper, J. C., & Lazarus, A. J. (2006). Solar wind proton temperature anisotropy: Linear theory and WIND/SWE observations. *Geophysical Research Letters*, *330*, L09101. https://doi.org/10.1029/2006GL025925

Hellinger, P., & Trávníček, P. M. (2014). Solar wind protons at 1 AU: Trends and bounds, constraints and correlations. *The Astrophysical Journal Letters*, *784*, L15. https://doi.org/10.1088/2041-8205/784/1/L15

Hervig, M. E., Brooke, J. S. A., Feng, W., Bardeen, C. G., & Plane, J. M. C. (2017). Constraints on meteoric smoke composition and meteoric influx using SOFIE observations with models. *Journal of Geophysical Research: Atmospheres*, *122*, 13495–13505. https://doi.org/10.1002/2017JD027657

Hervig, M. E., Siskind, D. E., Bailey, S. M., Merkel, A. W., DeLand, M. T., & Russell, J. M. (2019). The missing solar cycle response of the polar summer mesosphere. *Geophysical Research Letters*, *46*, 10132–10139. https://doi.org/10.1029/2019GL083485

Hesse, M., & Cassak, P. A. (2020). Magnetic reconnection in the space sciences: Past, present, and future. *Journal of Geophysical Research: Space Physics*, *125*, e2018JA025935. https://doi.org/10.1029/2018JA025935

Hidalgo, M. A., Cid, C., Medina, J., & Viñas, A. F. (2000). A new model for the topology of magnetic clouds in the solar wind. *Solar Physics*, *194*, 165–174.

Hidalgo, M. A., & Nieves-Chinchilla, T. (2012). A global magnetic topology model for magnetic clouds. *The Astrophysical Journal*, *748*, 109. https://doi.org/10.1088/0004-637X/748/2/109

Hidalgo, M. A., Nieves-Chinchilla, T., & Cid, C. (2002). Elliptical cross-section model for the magnetic topology of magnetic clouds. *Geophysical Research Letters*, *29*(13), 1637. https://doi.org/10.1029/2001GL013875

Hietala, H., Agueda, N., Andréeová, K., Vainio, R., Nylund, S., Kilpua, E. K. J., & Koskinen, H. E. J. (2011). In situ observations of particle acceleration in shock-shock interaction. *Journal of Geophysical Research*, *116*, 10105. https://doi.org/10.1029/2011JA016669

Hietala, H., Sandroos, A., & Vainio, R. (2012). Particle acceleration in shock-shock interaction: Model to data comparison. *The Astrophysical Journal Letters*, *751*, L14. https://doi.org/10.1088/2041-8205/751/1/L14

Hillaris, A., Bouratzis, C., & Nindos, A. (2016). Interplanetary type IV bursts. *Solar Physics*, *291*, 2049–2069. https://doi.org/10.1007/s11207-016-0946-6

Ho, G. C., Hamilton, D. C., Gloeckler, G., & Bochsler, P. (2000). Enhanced solar wind $^3\mathrm{He}^{2+}$ associated with coronal mass ejections. *Geophysical Research Letters*, *27*, 309–312. https://doi.org/10.1029/1999GL003660

Hoang, S., Maksimovic, M., Bougeret, J.-L., Reiner, M. J., & Kaiser, M. L. (1998). Wind-Ulysses source location of radio emissions associated with the January 1997 Coronal Mass Ejection. *Geophysical Research Letters*, *25*, 2497–2500. https://doi.org/10.1029/98GL00571

Horaites, K., Boldyrev, S., Krasheninnikov, S. I., Salem, C., Bale, S. D., & Pulupa, M. (2015). Self-similar theory of thermal conduction and application to the solar wind. *Physical Review Letters*, *114*(24), 245003. https://doi.org/10.1103/PhysRevLett.114.245003

Horaites, K., Boldyrev, S., & Medvedev, M. V. (2019). Electron strahl and halo formation in the solar wind. *Monthly Notices of the Royal Astronomical Society*, *484*, 2474–2481. https://doi.org/10.1093/mnras/sty3504

Horbury, T. S., Forman, M., & Oughton, S. (2008). Anisotropic scaling of magnetohydrodynamic turbulence. *Physical Review Letters*, *101*(17), 175005. https://doi.org/10.1103/PhysRevLett.101.175005

Horne, R. B., Thorne, R. M., Glauert, S. A., Albert, J. M., Meredith, N. P., & Anderson, R. R. (2005). Timescale for radiation belt electron acceleration by whistler mode chorus waves. *Journal of Geophysical Research*, *110*(A3), A03225. https://doi.org/10.1029/2004JA010811

Howes, G. G., Bale, S. D., Klein, K. G., Chen, C. H. K., Salem, C. S., & TenBarge, J. M. (2012). The slow-mode nature of compressible wave power in solar wind turbulence. *The Astrophysical Journal Letters*, *753*, L19. https://doi.org/10.1088/2041-8205/753/1/L19

Huba, J. D., & Wu, C. S. (1976). Effects of a magnetic field gradient on the lower hybrid drift instability. *Physics of Fluids*, *19*, 988–994. https://doi.org/10.1063/1.861594

Hu, Q., & Sonnerup, B. U. Ö. (2001). Reconstruction of magnetic flux ropes in the solar wind. *Geophysical Research Letters*, *28*, 467–470. https://doi.org/10.1029/2000GL012232

Hu, Q., & Sonnerup, B. U. Ö. (2002). Reconstruction of magnetic clouds in the solar wind: Orientations and configurations. *Journal of Geophysical Research*, *107*, 1142. https://doi.org/10.1029/2001JA000293

Hu, Q., Zheng, J., & Chen, Y. (2018). A database of small-scale magnetic flux ropes in the solar wind from Wind spacecraft measurements. *Journal of Physics Conference Series*, *1100*, 012012. https://doi.org/10.1088/1742-6596/1100/1/012012

Hull, A. J., Muschietti, L., Le Contel, O., Dorelli, J. C., & Lindqvist, P. A. (2020). MMS observations of intense whistler waves within Earth's supercritical bow shock: Source mechanism and impact on shock structure and plasma transport. *Journal of Geophysical Research: Space Physics*, *125*, e27290. https://doi.org/10.1029/2019JA027290

Hull, A. J., Muschietti, L., Oka, M., Larson, D. E., Mozer, F. S., Chaston, C. C., et al. (2012). Multiscale whistler waves within Earth's perpendicular bow shock. *Journal of Geophysical Research*, *117*, 12104. https://doi.org/10.1029/2012JA017870

Hurley, K., Atteia, J.-L., Crew, G., Ricker, G., Doty, J., Monnelly, G., et al. (2003). HETE-II and the Interplanetary Network. In G. R. Ricker & R. K. Vanderspek, (Eds.), Gamma-ray burst and afterglow astronomy 2001: A workshop celebrating the first year of the hete mission (Vol. 662, pp. 42–44). American Institute of Physics. https://doi.org/10.1063/1.1579296

Hurley, K., Cline, T., Mitrofanov, I., Mazets, E., Golenetskii, S., Frontera, F., et al. (2003). The Current Performance of the Third Interplanetary Network. In G. R. Ricker & R. K. Vanderspek, (Eds.), Gamma-ray burst and afterglow astronomy 2001: A workshop celebrating the first year of the hete mission (Vol. 662, pp. 473–476). American Institute of Physics. https://doi.org/10.1063/1.1579405

Hurley, K., Golenetskii, S., Aptekar, R., Mazets, E., Pal'Shin, V., Frederiks, D., et al. (2011). The Third Interplanetary Network. In J. E. McEnery, J. L. Racusin, & N. Gehrels, (Eds.), AIP Conference Proceedings (Vol. 1358, pp. 385–388). American Institute of Physics. https://doi.org/10.1063/1.3621810

Hurley, K., Rowlinson, A., Bellm, E., Perley, D., Mitrofanov, I. G., Golovin, D. V., et al. (2010). A new analysis of the short-duration, hard-spectrum GRB 051103, a possible extragalactic soft gamma repeater giant flare. *Monthly Notices of the Royal Astronomical Society*, *403*, 342–352. https://doi.org/10.1111/j.1365-2966.2009.16118.x

Illing, R. M. E., & Hundhausen, A. J. (1985). Observation of a coronal transient from 1.2 to 6 solar radii. *Journal of Geophysical Research*, *90*, 275–282. https://doi.org/10.1029/JA090iA01p00275

Janvier, M., Dasso, S., Démoulin, P., Masías-Meza, J. J., & Lugaz, N. (2015). Comparing generic models for interplanetary shocks and magnetic clouds axis configurations at 1 AU. *Journal of Geophysical Research: Space Physics*, *120*, 3328–3349. https://doi.org/10.1002/2014JA020836

Janvier, M., Winslow, R. M., Good, S., Bonhomme, E., Démoulin, P., Dasso, S., et al. (2019). Generic magnetic field intensity profiles of interplanetary coronal mass ejections at Mercury, Venus, and Earth from superposed epoch analyses. *Journal of Geophysical Research: Space Physics*, *124*, 812–836. https://doi.org/10.1029/2018JA025949

Jaynes, A. N., Baker, D. N., Singer, H. J., Rodriguez, J. V., Loto'aniu, T. M., Ali, A. F., et al. (2015). Source and seed populations for relativistic electrons: Their roles in radiation belt changes. *Journal of Geophysical Research: Sapce Physics*, *120*, 7240–7254. https://doi.org/10.1002/2015JA021234

Jian, L. K., Russell, C. T., Luhmann, J. G., & Galvin, A. B. (2018). STEREO observations of interplanetary coronal mass ejections in 2007-2016. *The Astrophysical Journal*, *855*, 114. https://doi.org/10.3847/1538-4357/aab189

Jian, L. K., Russell, C. T., Luhmann, J. G., Galvin, A. B., & MacNeice, P. J. (2009). Multi-spacecraft observations: Stream interactions and associated structures. *Solar Physics*, *259*, 345–360. https://doi.org/10.1007/s11207-009-9445-3

Jian, L., Russell, C. T., Luhmann, J. G., & Skoug, R. M. (2006). Properties of stream interactions at one AU during 1995–2004. *Solar Physics*, *239*, 337–392. https://doi.org/10.1007/s11207-006-0132-3

Kahler, S. W., Krucker, S., & Szabo, A. (2011). Solar energetic electron probes of magnetic cloud field line lengths. *Journal of Geophysical Research*, *116*, 1104. https://doi.org/10.1029/2010JA015328

Kaiser, M. L. (2003). Solar radio emissions at solar maximum: Interplanetary perspective. *Advances in Space Research*, *32*, 461–465. https://doi.org/10.1016/S0273-1177(03)00330-2

Kaiser, M. L., Reiner, M. J., Gopalswamy, N., Howard, R. A., Cyr, S. O. C., Thompson, B. J., & Bougeret, J.-L. (1998). Type II radio emissions in the frequency range from 1-14 MHz associated with the April 7, 1997 solar event. *Geophysical Research Letters*, *25*, 2501–2504. https://doi.org/10.1029/98GL00706

Kasper, J. C., & Klein, K. G. (2019). Strong preferential ion heating is limited to within the solar Alfvén surface. *The Astrophysical Journal Letters*, *877*(2), L35. https://doi.org/10.3847/2041-8213/ab1de5

Kasper, J. C., Klein, K. G., Weber, T., Maksimovic, M., Zaslavsky, A., Bale, S. D., et al. (2017). A zone of preferential ion heating extends tens of solar radii from the sun. *The Astrophysical Journal*, *849*, 126. https://doi.org/10.3847/1538-4357/aa84b1

Kasper, J. C., Lazarus, A. J., & Gary, S. P. (2002). Wind/SWE observations of firehose constraint on solar wind proton temperature anisotropy. *Geophysical Research Letters*, *29*, 1839. https://doi.org/10.1029/2002GL015128

Kasper, J. C., Lazarus, A. J., & Gary, S. P. (2008). Hot solar-wind helium: Direct evidence for local heating by Alfvén-cyclotron dissipation. *Physical Review Letters*, *101*, 261103-+. https://doi.org/10.1103/PhysRevLett.101.261103

Kasper, J. C., Lazarus, A. J., Gary, S. P., & Szabo, A. (2003). Solar wind temperature anisotropies. In M. Velli, R. Bruno, F. Malara, & B. Bucci, (Eds.), Solar Wind Ten (Vol. 679, pp. 538–541). American Institute of Physics. https://doi.org/10.1063/1.1618653

Kasper, J. C., Lazarus, A. J., Steinberg, J. T., Ogilvie, K. W., & Szabo, A. (2006). Physics-based tests to identify the accuracy of solar wind ion measurements: A case study with the Wind Faraday Cups. *Journal of Geophysical Research*, *111*, A03105. https://doi.org/10.1029/2005JA011442

Kasper, J. C., Maruca, B. A., Stevens, M. L., & Zaslavsky, A. (2013). Sensitive test for ion-cyclotron resonant heating in the solar wind. *Physical Review Letters*, *110*(9), 091102. https://doi.org/10.1103/PhysRevLett.110.091102

Kasper, J. C., Stevens, M. L., Korreck, K. E., Maruca, B. A., Kiefer, K. K., Schwadron, N. A., & Lepri, S. T. (2012). Evolution of the relationships between helium abundance, minor ion charge state, and solar wind speed over the solar cycle. *The Astrophysical Journal*, *745*, 162. https://doi.org/10.1088/0004-637X/745/2/162

Kasper, J. C., Stevens, M. L., Lazarus, A. J., Steinberg, J. T., & Ogilvie, K. W. (2007). Solar wind helium abundance as a function of speed and heliographic latitude: Variation through a solar cycle. *The Astrophysical Journal*, *660*, 901–910. https://doi.org/10.1086/510842

Kellogg, P. J. (2017). Note on the Pantellini et al. process for dust impact signals on spacecraft. *Journal of Geophysical Research: Space Physics*, *122*, 63–70. https://doi.org/10.1002/2016JA023073

Kellogg, P. J., Cattell, C. A., Goetz, K., Monson, S. J., & Wilson, L. B., III. (2011). Large amplitude whistlers in the magnetosphere observed with Wind-Waves. *Journal of Geophysical Research*, *116*, 9224. https://doi.org/10.1029/2010JA015919

Kellogg, P. J., Goetz, K., & Monson, S. J. (2016). Dust impact signals on the wind spacecraft. *Journal of Geophysical Research: Space Physics*, *121*, 966–991. https://doi.org/10.1002/2015JA021124

Kellogg, P. J., Goetz, K., & Monson, S. J. (2018). Sign of the dust impact-antenna coupling cloud. *Journal of Geophysical Research: Space Physics*, *123*, 3273–3276. https://doi.org/10.1029/2017JA025173

Kellogg, P. J., Goetz, K., Monson, S. J., & Bale, S. D. (1999). A search for Langmuir solitons in the Earth's foreshock. *Journal of Geophysical Research*, *104*, 6751–6758. https://doi.org/10.1029/1999JA900021

Kellogg, P. J., Goetz, K., Monson, S. J., Bougeret, J.-L., Manning, R., & Kaiser, M. L. (1996). Observations of plasma waves during a traversal of the moon's wake. *Geophysical Research Letters*, *23*, 1267–1270. https://doi.org/10.1029/96GL00376

Kellogg, P. J., Monson, S. J., Goetz, K., Howard, R. L., Bougeret, J.-L., & Kaiser, M. L. (1996). Early wind observations of bow shock and foreshock waves. *Geophysical Research Letters*, *23*, 1243–1246. https://doi.org/10.1029/96GL01067

Kersten, K., Cattell, C. A., Breneman, A., Goetz, K., Kellogg, P. J., Wygant, J. R., et al. (2011). Observation of relativistic electron microbursts in conjunction with intense radiation belt whistler-mode waves. *Geophysical Research Letters*, *38*, 8107.

Kilpua, E., Koskinen, H. E. J., & Pulkkinen, T. I. (2017). Coronal mass ejections and their sheath regions in interplanetary space. *Living Reviews in Solar Physics*, *14*, 5. https://doi.org/10.1007/s41116-017-0009-6

Kilpua, E. K. J., Balogh, A., von Steiger, R., & Liu, Y. D. (2017). Geoeffective properties of solar transients and stream interaction regions. *Space Science Reviews*, *212*, 1271–1314. https://doi.org/10.1007/s11214-017-0411-3

Kilpua, E. K. J., Lee, C. O., Luhmann, J. G., & Li, Y. (2011). Interplanetary coronal mass ejections in the near-Earth solar wind during the minimum periods following solar cycles 22 and 23. *Annales Geophysicae*, *29*, 1455–1467. https://doi.org/10.5194/angeo-29-1455-2011

King, J. H., & Papitashvili, N. E. (2005). Solar wind spatial scales in and comparisons of hourly Wind and ACE plasma and magnetic field data. *Journal of Geophysical Research*, *110*, A02104. https://doi.org/10.1029/2004JA010649

Klassen, A., Bothmer, V., Mann, G., Reiner, M. J., Krucker, S., Vourlidas, A., & Kunow, H. (2002). Solar energetic electron events and coronal shocks. *Astronomy & Astrophysics*, *385*, 1078–1088. https://doi.org/10.1051/0004-6361:20020205

Klebesadel, R. W., Strong, I. B., & Olson, R. A. (1973). Observations of gamma-ray bursts of cosmic origin. *The Astrophysical Journal Letters*, *182*, L85. https://doi.org/10.1086/181225

Klein, K. G., Alterman, B. L., Stevens, M. L., Vech, D., & Kasper, J. C. (2018). Majority of solar wind intervals support ion-driven instabilities. *Physical Review Letters*, *120*(20), 205102. https://doi.org/10.1103/PhysRevLett.120.205102

Klein, K. G., Howes, G. G., TenBarge, J. M., Bale, S. D., Chen, C. H. K., & Salem, C. S. (2012). Using synthetic spacecraft data to interpret compressible fluctuations in solar wind turbulence. *The Astrophysical Journal*, *755*, 159. https://doi.org/10.1088/0004-637X/755/2/159

Klein, K.-L., Tziotziou, K., Zucca, P., Valtonen, E., Vilmer, N., Malandraki, O. E., et al. (2018). X-Ray, Radio and SEP Observations of Relativistic Gamma-Ray Events. In O. E. Malandraki, & N. B. Crosby, (Eds.), Solar Particle Radiation Storms Forecasting and Analysis (Vol. 444, pp. 133–155). Springer. https://doi.org/10.1007/978-3-319-60051-2_8

Kouveliotou, C., Strohmayer, T., Hurley, K., van Paradijs, J., Finger, M. H., Dieters, S., et al. (1999). Discovery of a magnetar associated with the soft gamma repeater SGR 1900+14. *The Astrophysical Journal*, *510*, L115–L118. https://doi.org/10.1086/311813

Koval, A., & Szabo, A. (2010). Multispacecraft observations of interplanetary shock shapes on the scales of the Earth's magnetosphere. *Journal of Geophysical Research*, *115*, 12105. https://doi.org/10.1029/2010JA015373

Krasnoselskikh, V. V., Lembège, B., Savoini, P., & Lobzin, V. V. (2002). Nonstationarity of strong collisionless quasiperpendicular shocks: Theory and full particle numerical simulations. *Physics of Plasmas*, *9*, 1192–1209. https://doi.org/10.1063/1.1457465

Krucker, S., Larson, D. E., Lin, R. P., & Thompson, B. J. (1999). On the origin of impulsive electron events observed at 1 AU. *The Astrophysical Journal*, *519*, 864–875. https://doi.org/10.1086/307415

Krupar, V., Szabo, A., Maksimovic, M., Kruparova, O., Kontar, E. P., Balmaceda, L. A., et al. (2020). Density fluctuations in the solar wind based on type III radio bursts observed by parker solar probe. *The Astrophysical Journal—Supplement Series*, *246*(2), 57. https://doi.org/10.3847/1538-4365/ab65bd

Kubicka, M., Möstl, C., Amerstorfer, T., Boakes, P. D., Feng, L., Eastwood, J. P., & Törmänen, O. (2016). Prediction of geomagnetic storm strength from inner heliospheric in situ observations. *The Astrophysical Journal*, *833*(2), 255. https://doi.org/10.3847/1538-4357/833/2/255

Lampe, M., Manheimer, W. M., McBride, J. B., Orens, J. H., Shanny, R., & Sudan, R. N. (1971). Nonlinear development of the beam-cyclotron instability. *Physical Review Letters*, *26*, 1221–1225. https://doi.org/10.1103/PhysRevLett.26.1221

Lampe, M., McBride, J. B., Orens, J. H., & Sudan, R. N. (1971). On the theory of the beam cyclotron instability in plasmas. *Physics Letters A*, *35*, 129–130. https://doi.org/10.1016/0375-9601(71)90583-4

Lanabere, V., Dasso, S., Démoulin, P., Janvier, M., Rodriguez, L., & Masías-Meza, J. J. (2020). Magnetic twist profile inside magnetic clouds derived with a superposed epoch analysis. *Astronomy & Astrophysics*, *635*, A85. https://doi.org/10.1051/0004-6361/201937404

Lario, D., Ho, G. C., Decker, R. B., Roelof, E. C., Desai, M. I., & Smith, C. W. (2003). ACE observations of energetic particles associated with transient interplanetary shocks. In M. Velli, R. Bruno, F. Malara, & B. Bucci, (Eds.), *Proceedings of 10th international solar wind conference* (Vol. *679*, pp. 640–643). https://doi.org/10.1063/1.1618676

Larson, D. E., Lin, R. P., McTiernan, J. M., McFadden, J. P., Ergun, R. E., McCarthy, M., et al. (1997). Tracing the topology of the October 18-20, 1995, magnetic cloud with ˜0.1-10^2 keV electrons. *Geophysical Research Letters*, *24*, 1911–1914. https://doi.org/10.1029/97GL01878

Larson, D. E., Lin, R. P., & Steinberg, J. (2000). Extremely cold electrons in the January 1997 magnetic cloud. *Geophysical Research Letters*, *27*, 157–160. https://doi.org/10.1029/1999GL003632

Laurenza, M., Cliver, E. W., Hewitt, J., Storini, M., Ling, A. G., Balch, C. C., & Kaiser, M. L. (2009). A technique for short-term warning of solar energetic particle events based on flare location, flare size, and evidence of particle escape. *Space Weather*, *70*, S04008. https://doi.org/10.1029/2007SW000379

Lavraud, B., Gosling, J. T., Rouillard, A. P., Fedorov, A., Opitz, A., Sauvaud, J.-A., et al. (2009). Observation of a complex solar wind reconnection exhaust from spacecraft separated by over 1800 R_E. *Solar Physics*, *256*, 379–392. https://doi.org/10.1007/s11207-009-9341-x

Leamon, R. J., Matthaeus, W. H., Smith, C. W., Zank, G. P., Mullan, D. J., & Oughton, S. (2000). MHD-driven kinetic dissipation in the solar wind and corona. *The Astrophysical Journal*, *537*(2), 1054–1062. https://doi.org/10.1086/309059

Leamon, R. J., Smith, C. W., Ness, N. F., Matthaeus, W. H., & Wong, H. K. (1998). Observational constraints on the dynamics of the interplanetary magnetic field dissipation range. *Journal of Geophysical Research*, *103*, 4775. https://doi.org/10.1029/97JA03394

Leblanc, Y., Dulk, G. A., Cairns, I. H., & Bougeret, J.-L. (2000). Type II fixed on boards flare continuum in the corona and solar wind. *Journal of Geophysical Research*, *105*, 18215–18224. https://doi.org/10.1029/1999JA000429

Lemons, D. S., & Gary, S. P. (1978). Current-driven instabilities in a laminar perpendicular shock. *Journal of Geophysical Research*, *83*, 1625–1632. https://doi.org/10.1029/JA083iA04p01625

Lepping, R. P., Acũna, M. H., Burlaga, L. F., Farrell, W. M., Slavin, J. A., Schatten, K. H., et al. (1995). The wind magnetic field investigation. *Space Science Reviews*, *71*, 207–229. https://doi.org/10.1007/BF00751330

Lepping, R. P., Berdichevsky, D. B., Szabo, A., Arqueros, C., & Lazarus, A. J. (2003). Profile of an average magnetic cloud at 1 au for the quiet solar phase: Wind observations. *Solar Physics*, *212*, 425–444.

Lepping, R. P., Berdichevsky, D. B., & Wu, C.-C. (2017). Average magnetic field magnitude profiles of wind magnetic clouds as a function of closest approach to the clouds' axes and comparison to model. *Solar Physics*, *292*, 27. https://doi.org/10.1007/s11207-016-1040-9

Lepping, R. P., Berdichevsky, D. B., Wu, C. C., Szabo, A., Narock, T., Mariani, F., et al. (2006). A summary of WIND magnetic clouds for years 1995-2003: Model-fitted parameters, associated errors and classifications. *Annales Geophysicae*, *24*(1), 215–245. https://doi.org/10.5194/angeo-24-215-2006

Lepping, R. P., Burlaga, L. F., Szabo, A., Ogilvie, K. W., Mish, W. H., Vassiliadis, D., et al. (1997). The Wind magnetic cloud and events of October 18-20, 1995: Interplanetary properties and as triggers for geomagnetic activity. *Journal of Geophysical Research*, *102*, 14049–14064. https://doi.org/10.1029/97JA00272

Lepping, R. P., Jones, J. A., & Burlaga, L. F. (1990). Magnetic field structure of interplanetary magnetic clouds at 1 AU. *Journal of Geophysical Research*, *95*, 11957–11965. https://doi.org/10.1029/JA095iA08p11957

Lepping, R. P., Narock, T. W., & Chen, H. (2007). Comparison of magnetic field observations of an average magnetic cloud with a simple force free model: The importance of field compression and expansion. *Annales Geophysicae*, *25*, 2641–2648.

Lepping, R. P., Wu, C.-C., & Berdichevsky, D. B. (2005). Automatic identification of magnetic clouds and cloud-like regions at 1 AU: Occurrence rate and other properties. *Annales Geophysicae*, *23*, 2687–2704. https://doi.org/10.5194/angeo-23-2687-2005

Lepping, R. P., Wu, C.-C., Berdichevsky, D. B., & Ferguson, T. (2008). Estimates of magnetic cloud expansion at 1 AU. *Annales Geophysicae*, *26*, 1919–1933. https://doi.org/10.5194/angeo-26-1919-2008

Lepping, R. P., Wu, C.-C., Berdichevsky, D. B., & Kay, C. (2018). Magnetic field magnitude modification for a force-free magnetic cloud model. *Solar Physics*, *293*, 162. https://doi.org/10.1007/s11207-018-1383-5

Lepping, R. P., Wu, C. C., Berdichevsky, D. B., & Szabo, A. (2011). Magnetic clouds at/near the 2007 - 2009 solar minimum: Frequency of occurrence and some unusual properties. *Solar Physics*, *274*(1–2), 345–360. https://doi.org/10.1007/s11207-010-9646-9

Lepping, R. P., Wu, C.-C., Berdichevsky, D. B., & Szabo, A. (2018). Wind magnetic clouds for the period 2013 - 2015: Model fitting, types, associated shock waves, and comparisons to other periods. *Solar Physics*, *293*, 65. https://doi.org/10.1007/s11207-018-1273-x

Lepping, R. P., Wu, C. C., Berdichevsky, D. B., & Szabo, A. (2020). Model fitting of wind magnetic clouds for the period 2004 - 2006. *Solar Physics*, *295*(6), 83. https://doi.org/10.1007/s11207-020-01630-2

Lepping, R. P., Wu, C.-C., Gopalswamy, N., & Berdichevsky, D. B. (2008). Average thickness of magnetosheath upstream of magnetic clouds at 1 AU versus solar longitude of source. *Solar Physics*, *248*, 125–139. https://doi.org/10.1007/s11207-007-9111-6

Li, W., Thorne, R. M., Bortnik, J., Baker, D. N., Reeves, G. D., Kanekal, S. G., et al. (2015). Solar wind conditions leading to efficient radiation belt electron acceleration: A superposed epoch analysis. *Geophysical Research Letters*, *42*, 6906–6915. https://doi.org/10.1002/2015GL065342

Li, Y., Luhmann, J. G., & Lynch, B. J. (2018). Magnetic clouds: Solar cycle dependence, sources, and geomagnetic impacts. *Solar Physics*, *293*, 135. https://doi.org/10.1007/s11207-018-1356-8

Lin, R. P., Anderson, K. A., Ashford, S., Carlson, C., Curtis, D., Ergun, R., et al. (1995). A three-dimensional plasma and energetic particle investigation for the wind spacecraft. *Space Science Reviews*, *71*, 125–153. https://doi.org/10.1007/BF00751328

Liu, X., Yue, J., Wang, W., Xu, J., Zhang, Y., Li, J., et al. (2018). Responses of lower thermospheric temperature to the 2013 St. Patrick's Day geomagnetic storm. *Geophysical Research Letters*, *45*, 4656–4664. https://doi.org/10.1029/2018GL078039

Liu, Y. D., Luhmann, J. G., Lugaz, N., Möstl, C., Davies, J. A., Bale, S. D., & Lin, R. P. (2013). On Sun-to-Earth propagation of coronal mass ejections. *The Astrophysical Journal*, *769*(1), 45. https://doi.org/10.1088/0004-637X/769/1/45

Lotko, W., Smith, R. H., Zhang, B., Ouellette, J. E., Brambles, O. J., & Lyon, J. G. (2014). Ionospheric control of magnetotail reconnection. *Science*, *345*, 184–187. https://doi.org/10.1126/science.1252907

Lugaz, N., Farrugia, C. J., Winslow, R. M., Al-Haddad, N., Galvin, A. B., Nieves-Chinchilla, T., et al. (2018). On the spatial coherence of magnetic ejecta: Measurements of coronal mass ejections by multiple spacecraft longitudinally separated by 0.01 au. *The Astrophysical Journal Letters*, *864*, L7. https://doi.org/10.3847/2041-8213/aad9f4

Lugaz, N., Manchester, W. B., IV, Roussev, I. I., Tóth, G., & Gombosi, T. I. (2007). Numerical investigation of the homologous coronal mass ejection events from active region 9236. *The Astrophysical Journal*, *659*, 788–800. https://doi.org/10.1086/512005

Lugaz, N., Winslow, R. M., & Farrugia, C. J. (2020). Evolution of a long-duration coronal mass ejection and its sheath region between Mercury and Earth on 9-14 July 2013. *Journal of Geophysical Research: Space Physics*, *125*, e27213. https://doi.org/10.1029/2019JA027213

Lundquist, S. (1951). On the stability of magneto-hydrostatic fields. *Physical Review*, *83*, 307–311. https://doi.org/10.1103/PhysRev.83.307

Lysenko, A. L., Altyntsev, A. T., Meshalkina, N. S., Zhdanov, D., & Fleishman, G. D. (2018). Statistics of "cold" early impulsive solar flares in X-ray and microwave domains. *The Astrophysical Journal*, *856*, 111. https://doi.org/10.3847/1538-4357/aab271

MacDowall, R. J., Lara, A., Manoharan, P. K., Nitta, N. V., Rosas, A. M., & Bougeret, J. L. (2003). Long-duration hectometric type III radio bursts and their association with solar energetic particle (SEP) events. *Geophysical Research Letters*, *30*, 8018. https://doi.org/10.1029/2002GL016624

MacDowall, R. J., Richardson, I. G., Hess, R. A., & Thejappa, G. (2009). Re-examining the correlation of complex solar type III radio bursts and solar energetic particles. In N. Gopalswamy & D. F. Webb, (Eds.), Iau symposium (Vol. 257, pp. 335–340). https://doi.org/10.1017/S1743921309029512

Mäkelä, P., Gopalswamy, N., & Akiyama, S. (2018).Direction-finding analysis of the 2012 July 6 type II solar radio burst at low frequencies. *The Astrophysical Journal*, *867*, 40. https://doi.org/10.3847/1538-4357/aae2b6

Malandraki, O. E., & Crosby, N. B. (2018). Solar energetic particles and space weather: Science and applications. In O. E. Malandraki, & N. B. Crosby, (Eds.), Solar Particle Radiation Storms Forecasting and Analysis (Vol. 444, pp. 1–26). Springer. https://doi.org/10.1007/978-3-319-60051-2_1

Malaspina, D. M., Cairns, I. H., & Ergun, R. E. (2011). Dependence of Langmuir wave polarization on electron beam speed in type III solar radio bursts. *Geophysical Research Letters*, *38*, L13101. https://doi.org/10.1029/2011GL047642

Malaspina, D. M., & Ergun, R. E. (2008). Observations of three-dimensional Langmuir wave structure. *Journal of Geophysical Research*, *113*, 12108. https://doi.org/10.1029/2008JA013656

Malaspina, D. M., Halekas, J., Berčič, L., Larson, D., Whittlesey, P., Bale, S. D., et al. (2020). Plasma waves near the electron cyclotron frequency in the near-sun solar wind. *The Astrophysical Journal—Supplement Series*, *246*(2), 21. https://doi.org/10.3847/1538-4365/ab4c3b

Malaspina, D. M., Horányi, M., Zaslavsky, A., Goetz, K., Wilson, L. B., & Kersten, K. (2014). Interplanetary and interstellar dust observed by the Wind/WAVES electric field instrument. *Geophysical Research Letters*, *41*, 266–272. https://doi.org/10.1002/2013GL058786

Malaspina, D. M., Newman, D. L., Wilson, L. B., III, Goetz, K., Kellogg, P. J., & Kersten, K. (2013). Electrostatic solitary waves in the solar wind: Evidence for instability at solar wind current sheets. *Journal of Geophysical Research: Space Physics*, *118*, 591–599

Malaspina, D. M., O'Brien, L. E., Thayer, F., Sternovsky, Z., & Collette, A. (2015). Revisiting STEREO interplanetary and interstellar dust flux and mass estimates. *Journal of Geophysical Research: Space Physics*, *120*, 6085–6100. https://doi.org/10.1002/2015JA021352

Malaspina, D. M., & Wilson, L. B., III (2016). A database of interplanetary and interstellar dust detected by the Wind spacecraft. *Journal of Geophysical Research: Space Physics*, *121*, 9369–9377. https://doi.org/10.1002/2016JA023209

Mangeney, A. (2001). Intermittency in the solar wind turbulence and the haar wavelet transform. In B. Warmbein, (Ed.), Sheffield space plasma meeting: Multipoint measurements versus theory (Vol. 492, p. 53). Eurpoean Space Agency.

Mann, G., Classen, H. T., Keppler, E., & Roelof, E. C. (2002). On electron acceleration at CIR related shock waves. *Astronomy & Astrophysics*, *391*, 749–756. https://doi.org/10.1051/0004-6361:20020866

Mann, I., Nouzák, L., Vaverka, J., Antonsen, T., Fredriksen, Å., Issautier, K., et al. (2019). Dust observations with antenna measurements and its prospects for observations with Parker Solar Probe and Solar Orbiter. *Annales Geophysicae*, *37*(6), 1121–1140. https://doi.org/10.5194/angeo-37-1121-2019

Mann, I. R., Ozeke, L. G., Murphy, K. R., Claudepierre, S. G., Turner, D. L., Baker, D. N., et al. (2016). Explaining the dynamics of the ultra-relativistic third Van Allen radiation belt. *Nature Physics*, *12*, 978–983. https://doi.org/10.1038/nphys3799

Markovskii, S. A., Vasquez, B. J., & Smith, C. W. (2015). Statistical analysis of the magnetic helicity signature of the solar wind turbulence at 1 AU. *The Astrophysical Journal*, *806*, 78. https://doi.org/10.1088/0004-637X/806/1/78

Maroulis, D., Dumas, G., Bougeret, J. L., Caroubalos, C., & Poquérusse, M. (1993). The digital system ARTEMIS for real-time processing of radio transient emissions in the solar corona. *Solar Physics*, *147*, 359–375. https://doi.org/10.1007/BF00690725

Marsch, E. (2006). Kinetic physics of the solar corona and solar wind. *Living Reviews in Solar Physics*, *3*, 1–+

Marsch, E., & Chang, T. (1983). Electromagnetic lower hybrid waves in the solar wind. *Journal of Geophysical Research*, *88*, 6869–6880. https://doi.org/10.1029/JA088iA09p06869

Marubashi, K. (1986). Structure of the interplanetary magnetic clouds and their solar origins. *Advances in Space Research*, *6*, 335–338. https://doi.org/10.1016/0273-1177(86)90172-9

Marubashi, K. (2000). Physics of interplanetary magnetic flux ropes: Toward prediction of geomagnetic storms. *Advances in Space Research*, *26*(1), 55–66. https://doi.org/10.1016/S0273-1177(99)01026-1

Maruca, B. A., Bale, S. D., Sorriso-Valvo, L., Kasper, J. C., & Stevens, M. L. (2013). Collisional thermalization of hydrogen and helium in solar-wind plasma. *Physical Review Letters*, *111*(24), 241101. https://doi.org/10.1103/PhysRevLett.111.241101

Maruca, B. A., & Kasper, J. C. (2013). Improved interpretation of solar wind ion measurements via high-resolution magnetic field data. *Advances in Space Research*, *52*, 723–731. https://doi.org/10.1016/j.asr.2013.04.006

Maruca, B. A., Kasper, J. C., & Bale, S. D. (2011). What are the relative roles of heating and cooling in generating solar wind temperature anisotropies?. *Physical Review Letters*, *107*, 201101. https://doi.org/10.1103/PhysRevLett.107.201101

Maruca, B. A., Kasper, J. C., & Gary, S. P. (2012). Instability-driven limits on helium temperature anisotropy in the solar wind: observations and linear vlasov analysis. *The Astrophysical Journal*, *748*, 137. https://doi.org/10.1088/0004-637X/748/2/137

Mason, G. M., Desai, M. I., Mall, U., Korth, A., Bucik, R., von Rosenvinge, T. T., & Simunac, K. D. (2009). In situ observations of CIRs on STEREO, wind, and ACE during 2007 - 2008. *Solar Physics*, *256*, 393–408. https://doi.org/10.1007/s11207-009-9367-0

Mason, G. M., Mazur, J. E., Dwyer, J. R., Reames, D. V., & von Rosenvinge, T. T. (1997). New spectral and abundance features of interplantary heavy ions in corotating interaction regions. *The Astrophysical Journal*, *486*, L149. https://doi.org/10.1086/310845

Mason, G. M., von Steiger, R., Decker, R. B., Desai, M. I., Dwyer, J. R., Fisk, L. A., et al. (1999). Origin, injection, and acceleration of CIR particles: Observations report of working group 6. *Space Science Reviews*, *89*, 327–367. https://doi.org/10.1023/A:1005278214143

Matsui, H., Farrugia, C. J., & Torbert, R. B. (2002). Wind-ACE solar wind correlations, 1999: An approach through spectral analysis. *Journal of Geophysical Research*, *107*(A11), 1355. https://doi.org/10.1029/2002JA009251

Matthaeus, W. H., Dasso, S., Weygand, J. M., Kivelson, M. G., & Osman, K. T. (2010). Eulerian decorrelation of fluctuations in the interplanetary magnetic field. *The Astrophysical Journal*, *721*, L10–L13. https://doi.org/10.1088/2041-8205/721/1/L10

Matthaeus, W. H., Dasso, S., Weygand, J. M., Milano, L. J., Smith, C. W., & Kivelson, M. G. (2005). Spatial correlation of solar-wind turbulence from two-point measurements. *Physical Review Letters*, *95*, 231101. https://doi.org/10.1103/PhysRevLett.95.231101

Matthaeus, W. H., Weygand, J. M., & Dasso, S. (2016). Ensemble space-time correlation of plasma turbulence in the solar wind. *Physical Review Letters*, *116*(24), 245101. https://doi.org/10.1103/PhysRevLett.116.245101

Mazelle, C., Le Quéau, D., & Meziane, K. (2000). Nonlinear wave-particle interaction upstream from the Earth's bow shock. *Nonlinear Processes in Geophysics*, *7*, 185–190

Mazets, E. P., Aptekar, R. L., Cline, T. L., Frederiks, D. D., Goldsten, J. O., Golenetskii, S. V., et al. (2008). A giant flare from a soft gamma repeater in the andromeda galaxy (M31). *The Astrophysical Journal*, *680*, 545–549. https://doi.org/10.1086/587955

McComas, D. J., Christian, E. R., Schwadron, N. A., Fox, N., Westlake, J., Allegrini, F., et al. (2018). Interstellar mapping and acceleration probe (IMAP): A new NASA mission. *Space Science Reviews*, *214*(8), 116. https://doi.org/10.1007/s11214-018-0550-1

McFadden, J. P., Carlson, C. W., Larson, D., Ludlam, M., Abiad, R., Elliott, B., et al. (2008). The THEMIS ESA plasma instrument and inflight calibration. *Space Science Reviews*, *141*, 277–302. https://doi.org/10.1007/s11214-008-9440-2

McFadden, J. P., Phan, T. D., Carlson, C. W., Angelopoulos, V., Glassmeier, K.-H., & Auster, U. (2008). Structure of the subsolar magnetopause regions during northward IMF: First results from THEMIS. *Geophysical Research Letters*, *351*, L17S09. https://doi.org/10.1029/2008GL033630

Mellott, M. M. (1985). Subcritical collisionless shock waves. In B. T. Tsurutani, & R. G. Stone, (Eds.), Collisionless shocks in the heliosphere: Reviews of current research (Vol. 35, pp. 131–140). Washington, DC: AGU. Retrieved from http://doi.org/10.1029/GM035p0131

Meziane, K., Hamza, A. M., Wilber, M., Lee, M. A., Mazelle, C., Lucek, E. A., & Hada, T. (2011). Specular refection at a non-stationary shock: A simple model. *Planetary and Space Science*, *59*, 495–501. https://doi.org/10.1016/j.pss.2010.10.016

Meziane, K., Hull, A. J., Hamza, A. M., & Lin, R. P. (2002). On the bow shock θ_{Bn} dependence of upstream 70 keV to 2 MeV ion fluxes. *Journal of Geophysical Research*, *107*(A9), 1243. https://doi.org/10.1029/2001JA005012

Meziane, K., Lin, R. P., Parks, G. K., Larson, D. E., Bale, S. D., Mason, G. M., et al. (1999). Evidence for acceleration of ions to ~1 MeV by adiabatic-like reflection at the quasi-perpendicular Earth's bow shock. *Geophysical Research Letters*, *26*, 2925–2928. https://doi.org/10.1029/1999GL900603

Meziane, K., Mazelle, C., D'Uston, C., Rème, H., Lin, R. P., Carlson, C. W., et al. (1997). Wind observation of gyrating-like ion distributions and low frequency waves upstream from the earth's bow shock. *Advances in Space Research*, *20*, 703–706. https://doi.org/10.1016/S0273-1177(97)00459-6

Meziane, K., Mazelle, C., Lin, R. P., Le Quéau, D., Larson, D. E., Parks, G. K., & Lepping, R. P. (2001). Three-dimensional observations of gyrating ion distributions far upstream from the Earth's bow shock and their association with low-frequency waves. *Journal of Geophysical Research*, *106*, 5731–5742. https://doi.org/10.1029/2000JA900079

Meziane, K., Wilber, M., Lin, R. P., & Parks, G. K. (2003). Gyrophase-restricted 100 keV-2 MeV ion beams near the foreshock boundary. *Geophysical Research Letters*, *30*(20), 200000. https://doi.org/10.1029/2003GL017592

Miteva, R., Samwel, S. W., & Costa-Duarte, M. V. (2018). The Wind/EPACT Proton Event Catalog (1996 - 2016). *Solar Physics*, *293*, 27. https://doi.org/10.1007/s11207-018-1241-5

Miteva, R., Samwel, S. W., & Krupar, V. (2017). Solar energetic particles and radio burst emission. *Journal of Space Weather and Space Climate*, *7*(27), A37. https://doi.org/10.1051/swsc/2017035

Morioka, A., Miyoshi, Y., Iwai, K., Kasaba, Y., Masuda, S., Misawa, H., & Obara, T. (2015). Solar micro-Type III burst storms and long dipolar magnetic field in the outer corona. *The Astrophysical Journal*, *808*(2), 191. https://doi.org/10.1088/0004-637X/808/2/191

Morioka, A., Miyoshi, Y., Masuda, S., Tsuchiya, F., Misawa, H., Matsumoto, H., et al. (2007). Micro-type III radio bursts. *The Astrophysical Journal*, *657*, 567–576. https://doi.org/10.1086/510507

Möstl, C., Miklenic, C., Farrugia, C. J., Temmer, M., Veronig, A., Galvin, A. B., et al. (2008). Two-spacecraft reconstruction of a magnetic cloud and comparison to its solar source. *Annales Geophysicae*, *26*, 3139–3152. https://doi.org/10.5194/angeo-26-3139-2008

Moullard, O., Burgess, D., Salem, C., Mangeney, A., Larson, D. E., & Bale, S. D. (2001). Whistler waves, Langmuir waves and single loss cone electron distributions inside a magnetic cloud: Observations. *Journal of Geophysical Research*, *106*, 8301–8314. https://doi.org/10.1029/2000JA900144

Müller, D., Cyr, S. O. C., Zouganelis, I., Gilbert, H. R., Marsden, R., Nieves-Chinchilla, T., et al. (2020). The Solar Orbiter mission. Science overview. *Astronomy & Astrophysics*, *642*, 31. https://doi.org/10.1051/0004-6361/202038467

Mulligan, T., Russell, C. T., Anderson, B. J., Lohr, D. A., Rust, D., Toth, B. A., et al. (1999). Intercomparison of NEAR and Wind interplanetary coronal mass ejection observations. *Journal of Geophysical Research*, *1042*, 28217–28224. https://doi.org/10.1029/1999JA900215

Mulligan, T., Russell, C. T., & Luhmann, J. G. (1998). Solar cycle evolution of the structure of magnetic clouds in the inner heliosphere. *Geophysical Research Letters*, *25*, 2959–2962. https://doi.org/10.1029/98GL01302

Muschietti, L., & Lembège, B. (2013). Microturbulence in the electron cyclotron frequency range at perpendicular supercritical shocks. *Journal of Geophysical Research: Space Physics*, *118*, 2267–2285. https://doi.org/10.1002/jgra.50224

Muschietti, L., & Lembège, B. (2017). Two-stream instabilities from the lower-hybrid frequency to the electron cyclotron frequency: Application to the front of quasi-perpendicular shocks. *Annales Geophysicae*, *35*, 1093–1112. https://doi.org/10.5194/angeo-35-1093-2017

Nakwacki, M. S., Dasso, S., Démoulin, P., Mandrini, C. H., & Gulisano, A. M. (2011). Dynamical evolution of a magnetic cloud from the Sun to 5.4 AU. *Astronomy & Astrophysics*, *535*, A52. https://doi.org/10.1051/0004-6361/201015853

Ness, N. F. (1972). Interaction of the solar wind with the moon. In *The interplanetary medium: Part ii of solar-terrestrial physics/1970* (pp. 159–205).

Neugebauer, M., & Giacalone, J. (2005). Multispacecraft observations of interplanetary shocks: Nonplanarity and energetic particles. *Journal of Geophysical Research*, *110*, A12106. https://doi.org/10.1029/2005JA011380

Neugebauer, M., Giacalone, J., Chollet, E., & Lario, D. (2006). Variability of low-energy ion flux profiles on interplanetary shock fronts. *Journal of Geophysical Research*, *111*, A12107. https://doi.org/10.1029/2006JA011832

Nieves-Chinchilla, T., Colaninno, R., Vourlidas, A., Szabo, A., Lepping, R. P., Boardsen, S. A., et al. (2012). Remote and in situ observations of an unusual Earth-directed coronal mass ejection from multiple viewpoints. *Journal of Geophysical Research*, *117*, 6106. https://doi.org/10.1029/2011JA017243

Nieves-Chinchilla, T., Jian, L. K., Balmaceda, L., Vourlidas, A., dos Santos, L. F. G., & Szabo, A. (2019). Unraveling the internal magnetic field structure of the Earth-directed interplanetary coronal mass ejections during 1995 - 2015. *Solar Physics*, *294*(7), 89. https://doi.org/10.1007/s11207-019-1477-8

Nieves-Chinchilla, T., Linton, M. G., Hidalgo, M. A., Vourlidas, A., Savani, N. P., Szabo, A., et al. (2016). A circular-cylindrical flux-rope analytical model for magnetic clouds. *The Astrophysical Journal*, *823*, 27. https://doi.org/10.3847/0004-637X/823/1/27

Nieves-Chinchilla, T., Vourlidas, A., Raymond, J. C., Linton, M. G., Al-haddad, N., Savani, N. P., et al. (2018). Understanding the internal magnetic field configurations of ICMEs using more than 20 years of wind observations. *Solar Physics*, *293*, 25. https://doi.org/10.1007/s11207-018-1247-z

Nishida, A. (1994). The Geotail mission. *Geophysical Research Letters*, *21*, 2871–2873. https://doi.org/10.1029/94GL01223

O'Brien, T. P., McPherron, R. L., Sornette, D., Reeves, G. D., Friedel, R., & Singer, H. J. (2001). Which magnetic storms produce relativistic electrons at geosynchronous orbit?. *Journal of Geophysical Research*, *106*(A8), 15533–15544. https://doi.org/10.1029/2001JA000052

Ogilvie, K. W., Chornay, D. J., Fritzenreiter, R. J., Hunsaker, F., Keller, J., Lobell, J., et al. (1995). SWE, A comprehensive plasma instrument for the wind spacecraft. *Space Science Reviews*, *71*, 55–77. https://doi.org/10.1007/BF00751326

Ogilvie, K. W., Coplan, M. A., Roberts, D. A., & Ipavich, F. (2007). Solar wind structure suggested by bimodal correlations of solar wind speed and density between the spacecraft SOHO and Wind. *Journal of Geophysical Research*, *112*, A08104. https://doi.org/10.1029/2007JA012248

Ogilvie, K. W., & Desch, M. D. (1997). The wind spacecraft and its early scientific results. *Advances in Space Research*, *20*, 559–568. https://doi.org/10.1016/S0273-1177(97)00439-0

Ogilvie, K. W., Steinberg, J. T., Fitzenreiter, R. J., Owen, C. J., Lazarus, A. J., Farrell, W. M., & Torbert, R. B. (1996). Observations of the lunar plasma wake from the WIND spacecraft on December 27, 1994. *Geophysical Research Letters*, *23*, 1255–1258. https://doi.org/10.1029/96GL01069

Øieroset, M., Lin, R. P., Phan, T. D., Larson, D. E., & Bale, S. D. (2002). Evidence for electron acceleration up to ~300 keV in the magnetic reconnection diffusion region of Earth's magnetotail. *Physical Review Letters*, *89*, 195001. https://doi.org/10.1103/PhysRevLett.89.195001

Øieroset, M., Phan, T. D., Fujimoto, M., Lin, R. P., & Lepping, R. P. (2001). In situ detection of collisionless reconnection in the Earth's magnetotail. *Nature*, *412*, 414–417. https://doi.org/10.1038/35086520

Oka, M., Otsuka, F., Matsukiyo, S., Wilson, III, L. B., Argall, M. R., Amano, T., et al. (2019). Electron scattering by low-frequency whistler waves at Earth's bow shock. *The Astrophysical Journal*, *886*(53), 11. https://doi.org/10.3847/1538-4357/ab4a81

Osman, K. T., Matthaeus, W. H., Hnat, B., & Chapman, S. C. (2012).Kinetic signatures and intermittent turbulence in the solar wind plasma. *Physical Review Letters*, *108*(26), 261103. https://doi.org/10.1103/PhysRevLett.108.261103

Oughton, E. J., Skelton, A., Horne, R. B., Thomson, A. W. P., & Gaunt, C. T. (2017). Quantifying the daily economic impact of extreme space weather due to failure in electricity transmission infrastructure. *Space Weather*, *15*(1), 65–83. https://doi.org/10.1002/2016SW001491

Owen, C. J., Lepping, R. P., Ogilvie, K. W., Slavin, J. A., Farrell, W. M., & Byrnes, J. B. (1996). The lunar wake at 6.8 R_L: WIND magnetic field observations. *Geophysical Research Letters*, *23*, 1263–1266. https://doi.org/10.1029/96GL01354

Owens, A., Baker, R., Cline, T. L., Gehrels, N., Jermakian, J., Nolan, T., et al. (1995). A high-resolution GE spectrometer for gamma-ray burst astronomy. *Space Science Reviews*, *71*, 273–296. https://doi.org/10.1007/BF00751333

Owens, M. J., Horbury, T. S., & Arge, C. N. (2010). Probing the large-scale topology of the heliospheric magnetic field using jovian electrons. *The Astrophysical Journal*, *714*(2), 1617–1623. https://doi.org/10.1088/0004-637X/714/2/1617

Pal'shin, V. D., Charikov, Y. E., Aptekar, R. L., Golenetskii, S. V., Kokomov, A. A., Svinkin, D. S., et al. (2014). Konus-wind and helicon-coronas-F observations of solar flares. *Geomagnetism and Aeronomy*, *54*, 943–948. https://doi.org/10.1134/S0016793214070093

Pal'shin, V. D., Hurley, K., Svinkin, D. S., Aptekar, R. L., Golenetskii, S. V., Frederiks, D. D., et al. (2013). Interplanetary network localizations of konus short gamma-ray bursts. *The Astrophysical Journal—Supplement Series*, *207*, 38. https://doi.org/10.1088/0067-0049/207/2/38

Park, J., Caprioli, D., & Spitkovsky, A. (2015). Simultaneous acceleration of protons and electrons at nonrelativistic quasiparallel collisionless shocks. *Physical Review Letters*, *114*(8), 085003. https://doi.org/10.1103/PhysRevLett.114.085003

Paschmann, G., Papamastorakis, I., Sckopke, N., Haerendel, G., Sonnerup, B. U. O., Bame, S. J., et al. (1979).Plasma acceleration at the earth's magnetopause - Evidence for reconnection. *Nature*, *282*, 243–246. https://doi.org/10.1038/282243a0

Petroff, E., Hessels, J. W. T., & Lorimer, D. R. (2019). Fast radio bursts. *Astronomy and Astrophysics Review*, *27*(4), 75. https://doi.org/10.1007/s00159-019-0116-6

Phan, T. D., Gosling, J. T., Davis, M. S., Skoug, R. M., Øieroset, M., Lin, R. P., et al. (2006). A magnetic reconnection X-line extending more than 390 Earth radii in the solar wind. *Nature*, *439*, 175–178. https://doi.org/10.1038/nature04393

Pitňa, A., Šafránková, J., Němeček, Z., Franci, L., Pi, G., & Montagud Camps, V. (2019). Characteristics of solar wind fluctuations at and below ion scales. *The Astrophysical Journal*, *879*(2), 82. https://doi.org/10.3847/1538-4357/ab22b8

Podesta, J. J., & Borovsky, J. E. (2010). Scale invariance of normalized cross-helicity throughout the inertial range of solar wind turbulence. *Physics of Plasmas*, *17*, 112905. https://doi.org/10.1063/1.3505092

Podesta, J. J., Roberts, D. A., & Goldstein, M. L. (2006). Power spectrum of small-scale turbulent velocity fluctuations in the solar wind. *Journal of Geophysical Research*, *111*, A10109. https://doi.org/10.1029/2006JA011834

Podesta, J. J., Roberts, D. A., & Goldstein, M. L. (2007). Spectral exponents of kinetic and magnetic energy spectra in solar wind turbulence. *The Astrophysical Journal*, *664*, 543–548. https://doi.org/10.1086/519211

Pohjolainen, S., & Talebpour Sheshvan, N. (2020). Cut-off features in interplanetary solar radio type IV emission. *Advances in Space Research*, *65*(6), 1663–1672. https://doi.org/10.1016/j.asr.2019.05.034

Pulupa, M., & Bale, S. D. (2008). Structure on interplanetary shock fronts: Type II radio burst source regions. *The Astrophysical Journal*, *676*, 1330–1337. https://doi.org/10.1086/526405

Raj, A., Phan, T., Lin, R. P., & Angelopoulos, V. (2002). Wind survey of high-speed bulk flows and field-aligned beams in the near-Earth plasma sheet. *Journal of Geophysical Research*, *107*, 1419. https://doi.org/10.1029/2001JA007547

Raymond, J. C., Thompson, B. J., Cyr, S. O. C., Gopalswamy, N., Kahler, S., Kaiser, M., et al. (2000). SOHO and radio observations of a CME shock wave. *Geophysical Research Letters*, *27*, 1439–1442. https://doi.org/10.1029/1999GL003669

Reames, D. V. (2000). Abundances of trans-iron elements in solar energetic particle events. *The Astrophysical Journal*, *540*, L111–L114. https://doi.org/10.1086/312886

Reames, D. V. (2012). Particle energy spectra at traveling interplanetary shock waves. *The Astrophysical Journal*, *757*, 93. https://doi.org/10.1088/0004-637X/757/1/93

Reames, D. V. (2017). *Solar Energetic Particles*, 932. https://doi.org/10.1007/978-3-319-50871-9

Reames, D. V. (2018).Corotating shock waves and the solar-wind source of energetic ion abundances: Power laws in a/q. *Solar Physics*, *293*, 144. https://doi.org/10.1007/s11207-018-1369-3

Reames, D. V., Cliver, E. W., & Kahler, S. W. (2014). Abundance enhancements in impulsive solar energetic-particle events with associated coronal mass ejections. *Solar Physics*, *289*, 3817–3841. https://doi.org/10.1007/s11207-014-0547-1

Reames, D. V., & Ng, C. K. (2004). Heavy-element abundances in solar energetic particle events. *The Astrophysical Journal*, *610*, 510–522. https://doi.org/10.1086/421518

Reiner, M. J., Fainberg, J., Kaiser, M. L., & Bougeret, J.-L. (2007). Circular polarization observed in interplanetary type III radio storms. *Solar Physics*, *241*, 351–370. https://doi.org/10.1007/s11207-007-0277-8

Reiner, M. J., & Kaiser, M. L. (1999). High-frequency type II radio emissions associated with shocks driven by coronal mass ejections. *Journal of Geophysical Research*, *1041*, 16979–16992. https://doi.org/10.1029/1999JA900143

Reiner, M. J., Kaiser, M. L., & Bougeret, J.-L. (2007). Coronal and interplanetary propagation of CME/shocks from radio, in situ and white-light observations. *The Astrophysical Journal*, *663*, 1369–1385. https://doi.org/10.1086/518683

Reiner, M. J., Kaiser, M. L., Fainberg, J., Desch, M. D., & Stone, R. G. (1996). 2f_p radio emission from the vicinity of the Earth's foreshock: WIND observations. *Geophysical Research Letters*, *23*, 1247. https://doi.org/10.1029/96GL00841

Reiner, M. J., Kaiser, M. L., Fainberg, J., & Stone, R. G. (1998). A new method for studying remote type II radio emissions from coronal mass ejection-driven shocks. *Journal of Geophysical Research*, *1032*, 29651–29664. https://doi.org/10.1029/98JA02614

Reiner, M. J., Kaiser, M. L., Karlický, M., Jiřička, K., & Bougeret, J.-L. (2001). Bastille day event: A radio perspective. *Solar Physics*, *204*, 121–137. https://doi.org/10.1023/A:1014225323289

Reiner, M. J., Kaiser, M. L., Plunkett, S. P., Prestage, N. P., & Manning, R. (2000). Radio tracking of a white-light coronal mass ejection from solar corona to interplanetary medium. *The Astrophysical Journal*, *529*, L53–L56. https://doi.org/10.1086/312446

Reiner, M. J., & MacDowall, R. J. (2015). Electron exciter speeds associated with interplanetary type III solar radio bursts. *Solar Physics*, *290*, 2975–3004. https://doi.org/10.1007/s11207-015-0779-8

Richardson, I. G., & Cane, H. V. (2004). The fraction of interplanetary coronal mass ejections that are magnetic clouds: Evidence for a solar cycle variation. *Geophysical Research Letters*, *311*, L18804. https://doi.org/10.1029/2004GL020958

Richardson, I. G., & Cane, H. V. (2010). Near-Earth interplanetary coronal mass ejections during solar cycle 23 (1996 - 2009): Catalog and summary of properties. *Solar Physics*, *264*, 189–237. https://doi.org/10.1007/s11207-010-9568-6

Richardson, I. G., Mays, M. L., & Thompson, B. J. (2018). Prediction of solar energetic particle event peak proton intensity using a simple algorithm based on CME speed and direction and observations of associated solar phenomena. *Space Weather*, *16*, 1862–1881. https://doi.org/10.1029/2018SW002032

Richardson, J. D., & Paularena, K. I. (2001). Plasma and magnetic field correlations in the solar wind. *Journal of Geophysical Research*, *106*(1), 239–252. https://doi.org/10.1029/2000JA000071

Ridnaia, A., Svinkin, D., Frederiks, D., Bykov, A., Popov, S., Aptekar, R., et al. (2020). A peculiar hard X-ray counterpart of a Galactic fast radio burst. *Nature Astronomy*. arXiv:2005.11178. (in press). https://doi.org/10.1038/s41550-020-01265-0

Riley, P., Baker, D., Liu, Y. D., Verronen, P., Singer, H., & Güdel, M. (2018). Extreme space weather events: From cradle to grave. *Space Science Reviews*, *214*(1), 21. https://doi.org/10.1007/s11214-017-0456-3

Roberg-Clark, G. T., Drake, J. F., Swisdak, M., & Reynolds, C. S. (2018). Wave generation and heat flux suppression in astrophysical plasma systems. *The Astrophysical Journal*, *867*, 154. https://doi.org/10.3847/1538-4357/aae393

Roberts, O. J., Veres, P., Baring, M. G., & Others (2021). Rapid spectral variability of a giant flare from a magnetar in NGC 253. *Nature*, *589*(7841), 207–210. https://doi.org/10.1038/s41586-020-03077-8

Roth, I., & Temerin, M. (1997). Enrichment of ^{3}He and Heavy Ions in Impulsive Solar Flares. *The Astrophysical Journal*, *477*(2), 940–957. https://doi.org/10.1086/303731

Ruffenach, A., Lavraud, B., Owens, M. J., Sauvaud, J.-A., Savani, N. P., Rouillard, A. P., et al. (2012). Multispacecraft observation of magnetic cloud erosion by magnetic reconnection during propagation. *Journal of Geophysical Research*, *117*, 9101. https://doi.org/10.1029/2012JA017624

Russell, I., James, M., Bailey, S. M., Gordley, L. L., Rusch, D. W., Horányi, M., Hervig, M. E., et al. (2009). The Aeronomy of Ice in the Mesosphere (AIM) mission: Overview and early science results. *The Journal of Atmospheric and Solar-Terrestrial Physics*, *71*(3–4), 289–299. https://doi.org/10.1016/j.jastp.2008.08.011

Sadykov, V. M., Kosovichev, A. G., Oria, V., & Nita, G. M. (2017). An interactive multi-instrument database of solar flares. *The Astrophysical Journal—Supplement Series*, *231*, 6. https://doi.org/10.3847/1538-4365/aa79a9

Šafránková, J., Němeček, Z., Němec, F., Verscharen, D., Chen, C. H. K., Ďurovcová, T., & Riazantseva, M. O. (2019). Scale-dependent polarization of solar wind velocity fluctuations at the inertial and kinetic scales. *The Astrophysical Journal*, *870*(1), 40. https://doi.org/10.3847/1538-4357/aaf239

Sagdeev, R. Z. (1966). Cooperative phenomena and shock waves in collisionless plasmas. *Reviews of Plasma Physics*, *4*, 23

Salem, C., Hubert, D., Lacombe, C., Bale, S. D., Mangeney, A., Larson, D. E., & Lin, R. P. (2003). Electron properties and coulomb collisions in the solar wind at 1 AU: Wind observations. *The Astrophysical Journal*, *585*, 1147–1157. https://doi.org/10.1086/346185

Salem, C., Mangeney, A., Bale, S. D., & Veltri, P. (2009). Solar wind magnetohydrodynamics turbulence: Anomalous scaling and role of intermittency. *The Astrophysical Journal*, *702*, 537–553. https://doi.org/10.1088/0004-637X/702/1/537

Salman, T. M., Winslow, R. M., & Lugaz, N. (2020). Radial evolution of coronal mass ejections between MESSENGER, Venus Express, STEREO, and L1: Catalog and analysis. *Journal of Geophysical Research: Space Physics*, *125*, e27084. https://doi.org/10.1029/2019JA027084

Santolík, O., Gurnett, D. A., Pickett, J. S., Parrot, M., & Cornilleau-Wehrlin, N. (2003). Spatio-temporal structure of storm-time chorus. *Journal of Geophysical Research: Space Physics*, *108*(A7), 1278. https://doi.org/10.1029/2002JA009791

Santolík, O., Kletzing, C. A., Kurth, W. S., Hospodarsky, G. B., & Bounds, S. R. (2014). Fine structure of large-amplitude chorus wave packets. *Geophysical Research Letters*, *41*, 293–299. https://doi.org/10.1002/2013GL058889

Santolík, O., Pickett, J. S., Gurnett, D. A., Menietti, J. D., Tsurutani, B. T., & Verkhoglyadova, O. (2010). Survey of Poynting flux of whistler mode chorus in the outer zone. *Journal of Geophysical Research*, *115*, A00F13. https://doi.org/10.1029/2009JA014925

Savani, N. P., Vourlidas, A., Szabo, A., Mays, M. L., Richardson, I. G., Thompson, B. J., et al. (2015). Predicting the magnetic vectors within coronal mass ejections arriving at Earth: 1. Initial architecture. *Space Weather*, *13*, 374–385. https://doi.org/10.1002/2015SW001171

Schiller, Q., Li, X., Blum, L., Tu, W., Turner, D. L., & Blake, J. B. (2014). A nonstorm time enhancement of relativistic electrons in the outer radiation belt. *Geophysical Research Letters*, *41*, 7–12. https://doi.org/10.1002/2013GL058485

Scholer, M., Ipavich, F. M., Gloeckler, G., Hovestadt, D., & Klecker, B. (1980). Upstream particle events close to the bow shock and 200 R_E upstream: ISEE-1 and ISEE-3 observations. *Geophysical Research Letters*, *7*, 73–76. https://doi.org/10.1029/GL007i001p00073

Share, G. H., Murphy, R. J., White, S. M., Tolbert, A. K., Dennis, B. R., Schwartz, R. A., et al. (2018). Characteristics of late-phase > 100 MeV gamma-ray emission in solar eruptive events. *The Astrophysical Journal*, *869*, 182. https://doi.org/10.3847/1538-4357/aaebf7

Shen, C., Chi, Y., Wang, Y., Xu, M., & Wang, S. (2017). Statistical comparison of the ICME's geoeffectiveness of different types and different solar phases from 1995 to 2014. *Journal of Geophysical Research: Space Physics*, *122*, 5931–5948. https://doi.org/10.1002/2016JA023768

Shodhan, S., Crooker, N. U., Kahler, S. W., Fitzenreiter, R. J., Larson, D. E., Lepping, R. P., et al. (2000). Counterstreaming electrons in magnetic clouds. *Journal of Geophysical Research*, *105*, 27261–27268. https://doi.org/10.1029/2000JA000060

Shu, F. H. (1992). Physics of Astrophysics (Vol. II). University Science Books.

Sibeck, D. G., Phan, T.-D., Lin, R., Lepping, R. P., & Szabo, A. (2002). Wind observations of foreshock cavities: A case study. *Journal of Geophysical Research*, *107*(A10), 1271. https://doi.org/10.1029/2001JA007539

Sibeck, D., Kudela, K., Mukai, T., Nemecek, Z., & Safrankova, J. (2004). Radial dependence of foreshock cavities: A case study. *Annales Geophysicae*, *22*, 4143–4151. https://doi.org/10.5194/angeo-22-4143-2004

Siscoe, G., Crooker, N. U., & Clauer, C. R. (2006). Dst of the Carrington storm of 1859. *Advances in Space Research*, *38*(2), 173–179. https://doi.org/10.1016/j.asr.2005.02.102

Smith, E. J., & Wolfe, J. H. (1976). Observations of interaction regions and corotating shocks between one and five AU: Pioneers 10 and 11. *Geophysical Research Letters*, *3*, 137–140. https://doi.org/10.1029/GL003i003p00137

Sonnerup, B. U. Ö. (1979). Magnetic field reconnection. *Solar System Plasma Physics*,*3*, 45–108.

Stansby, D., Horbury, T. S., Chen, C. H. K., & Matteini, L. (2016). Experimental determination of whistler wave dispersion relation in the solar wind. *The Astrophysical Journal Letters*, *829*, L16. https://doi.org/10.3847/2041-8205/829/1/L16

Sterken, V. J., Westphal, A. J., Altobelli, N., Malaspina, D., & Postberg, F. (2019). Interstellar dust in the solar system. *Space Science Reviews*, *215*(7), 32. https://doi.org/10.1007/s11214-019-0607-9

Stix, T. H. (1992). *Waves in plasmas*. Springer.

Stone, E. C., Frandsen, A. M., Mewaldt, R. A., Christian, E. R., Margolies, D., Ormes, J. F., & Snow, F. (1998). The advanced composition explorer. *Space Science Reviews*, *86*, 1–22. https://doi.org/10.1023/A:1005082526237

Svinkin, D., Frederiks, D., Hurley, K., Aptekar, R., & Others (2021). A bright γ-ray flare interpreted as a giant magnetar flare in NGC 253. *Nature*, *589*(7841), 211–213. https://doi.org/10.1038/s41586-020-03076-9

Svinkin, D. S., Frederiks, D. D., Aptekar, R. L., Golenetskii, S. V., Pal'shin, V. D., Oleynik, P. P., et al. (2016). The second Konus-wind catalog of short gamma-ray bursts. *The Astrophysical Journal—Supplement Series*, *224*, 10. https://doi.org/10.3847/0067-0049/224/1/10

Szabo, A., Larson, D., Whittlesey, P., Stevens, M. L., Lavraud, B., Phan, T., et al. (2020). The heliospheric current sheet in the inner heliosphere observed by the parker solar probe. *The Astrophysical Journal—Supplement Series*, *246*(2), 47. https://doi.org/10.3847/1538-4365/ab5dac

Takeuchi, T., Araki, T., Luehr, H., Rasmussen, O., Watermann, J., Milling, D. K., et al. (2000). Geomagnetic negative sudden impulse due to a magnetic cloud observed on May 13, 1995. *Journal of Geophysical Research*, *105*, 18835–18846. https://doi.org/10.1029/2000JA900055

Talebpour Sheshvan, N., & Pohjolainen, S. (2018). Visibility and origin of compact interplanetary radio Type IV bursts. *Solar Physics*, *293*, 148. https://doi.org/10.1007/s11207-018-1371-9

Temerin, M., & Roth, I. (1992). The Production of 3He and Heavy Ion Enrichments in 3He-rich Flares by Electromagnetic Hydrogen Cyclotron Waves. *The Astrophysical Journal Letters*, *391*, L105. https://doi.org/10.1086/186408

Tidman, D. A., & Northrop, T. G. (1968). Emission of plasma waves by the Earth's bow shock. *Journal of Geophysical Research*, *73*, 1543–1553. https://doi.org/10.1029/JA073i005p01543

Tong, Y., Vasko, I. Y., Pulupa, M., Mozer, F. S., Bale, S. D., Artemyev, A. V., & Krasnoselskikh, V. (2019).Whistler wave generation by halo electrons in the solar wind. *The Astrophysical Journal Letters*, *870*, L6. https://doi.org/10.3847/2041-8213/aaf734

Tsurutani, B. T., Gonzalez, W. D., Gonzalez, A. L. C., Guarnieri, F. L., Gopalswamy, N., Grande, M., et al. (2006).Corotating solar wind streams and recurrent geomagnetic activity: A review. *Journal of Geophysical Research*, *111*, A07S01. https://doi.org/10.1029/2005JA011273

Tsurutani, B. T., & Lin, R. P. (1985).Acceleration of >47 keV ions and >2 keV electrons by interplanetary shocks at 1 AU. *Journal of Geophysical Research*, *90*, 1–11. https://doi.org/10.1029/JA090iA01p00001

Tsvetkova, A., Frederiks, D., Golenetskii, S., Lysenko, A., Oleynik, P., Pal'shin, V., et al. (2017). The Konus-wind catalog of gamma-ray bursts with known redshifts. I. Bursts detected in the triggered mode. *The Astrophysical Journal*, *850*, 161. https://doi.org/10.3847/1538-4357/aa96af

Turner, D. L., Angelopoulos, V., Morley, S. K., Henderson, M. G., Reeves, G. D., Li, W., et al. (2014). On the cause and extent of outer radiation belt losses during the 30 September 2012 dropout event. *Journal of Geophysical Research: Space Physics*, *119*, 1530–1540. https://doi.org/10.1002/2013JA019446

Vandas, M., Fischer, S., Pelant, P., & Geranios, A. (1993).Evidence for a spheroidal structure of magnetic clouds. *Journal of Geophysical Research*, *98*, 21061–21070. https://doi.org/10.1029/93JA01749

Vandas, M., Geranios, A., & Romashets, E. (2009). On expansion of magnetic clouds in the solar wind. *Astrophysics and Space Sciences Transactions*, *5*, 35–38. https://doi.org/10.5194/astra-5-35-2009

Vasko, I. Y., Krasnoselskikh, V., Tong, Y., Bale, S. D., Bonnell, J. W., & Mozer, F. S. (2019). Whistler fan instability driven by strahl electrons in the solar wind. *The Astrophysical Journal Letters*, *871*, L29. https://doi.org/10.3847/2041-8213/ab01bd

Vasko, I. Y., Kuzichev, I. V., Artemyev, A. V., Bale, S. D., Bonnell, J. W., & Mozer, F. S. (2020). On quasi-parallel whistler waves in the solar wind. *Physics of Plasmas*, *27*(8). 082902. https://doi.org/10.1063/5.0003401

Vasko, I. Y., Mozer, F. S., Krasnoselskikh, V. V., Artemyev, A. V., Agapitov, O. V., Bale, S. D., et al. (2018). Solitary waves across supercritical quasi-perpendicular shocks. *Geophysical Research Letters*, *45*, 5809–5817. https://doi.org/10.1029/2018GL077835

Vech, D., Mallet, A., Klein, K. G., & Kasper, J. C. (2018). Magnetic reconnection may control the ion-scale spectral break of solar wind turbulence. *The Astrophysical Journal Letters*, *855*, L27. https://doi.org/10.3847/2041-8213/aab351

Velli, M., Harra, L. K., Vourlidas, A., Schwadron, N., Panasenco, O., Liewer, P. C., et al. (2020). Understanding the origins of the heliosphere: Integrating observations and measurements from Parker Solar Probe, Solar Orbiter and Other space and ground based observatories. *Astronomy & Astrophysics, 642*, A4. https://doi.org/10.1051/0004-6361/202038245

Verdini, A., Grappin, R., Alexandrova, O., Franci, L., Landi, S., Matteini, L., & Papini, E. (2019). Three-dimensional local anisotropy of velocity fluctuations in the solar wind. *Monthly Notices of the Royal Astronomical Society*, *486*(3), 3006–3018. https://doi.org/10.1093/mnras/stz1041

Verdini, A., Grappin, R., Alexandrova, O., & Lion, S. (2018). 3D anisotropy of solar wind turbulence, tubes, or ribbons?. *The Astrophysical Journal*, *853*, 85. https://doi.org/10.3847/1538-4357/aaa433

Verscharen, D., Bourouaine, S., & Chand ran, B. D. G. (2013). Instabilities driven by the drift and temperature anisotropy of alpha particles in the solar wind. *The Astrophysical Journal*, *773*(2), 163. https://doi.org/10.1088/0004-637X/773/2/163

Verscharen, D., Chandran, B. D. G., Jeong, S.-Y., Salem, C. S., Pulupa, M. P., & Bale, S. D. (2019). Self-induced scattering of strahl electrons in the solar wind. *The Astrophysical Journal*, *886*(2), 136. https://doi.org/10.3847/1538-4357/ab4c30

Verscharen, D., Chen, C. H. K., & Wicks, R. T. (2017).On kinetic slow modes, fluid slow modes, and pressure-balanced structures in the solar wind. *The Astrophysical Journal*, *840*, 106. https://doi.org/10.3847/1538-4357/aa6a56

Verscharen, D., Klein, K. G., & Maruca, B. A. (2019). The multi-scale nature of the solar wind. *Living Reviews in Solar Physics*, *16*(1), 5. https://doi.org/10.1007/s41116-019-0021-0

von Rosenvinge, T. T., Barbier, L. M., Karsch, J., Liberman, R., Madden, M. P., Nolan, T., et al. (1995). The Energetic Particles: Acceleration, Composition, and Transport (EPACT) investigation on the WIND spacecraft. *Space Science Reviews*, *71*, 155–206. https://doi.org/10.1007/BF00751329

Vršnak, B., Amerstorfer, T., Dumbović, M., Leitner, M., Veronig, A. M., Temmer, M., et al. (2019). Heliospheric evolution of magnetic clouds. *The Astrophysical Journal*, *877*(2), 77. https://doi.org/10.3847/1538-4357/ab190a

Vršnak, B., Aurass, H., Magdalenić, J., & Gopalswamy, N. (2001). Band-splitting of coronal and interplanetary type II bursts. I. Basic properties. *Astronomy & Astrophysics*, *377*, 321–329. https://doi.org/10.1051/0004-6361:20011067

Walker, S. N., Balikhin, M. A., Alleyne, H. S. C. K., Hobara, Y., André, M., & Dunlop, M. W. (2008). Lower hybrid waves at the shock front: A reassessment. *Annales Geophysicae*, *26*, 699–707

Wang, L., Krucker, S., Mason, G. M., Lin, R. P., & Li, G. (2016). The injection of ten electron/^{3}He-rich SEP events. *Astronomy & Astrophysics*, *585*, A119. https://doi.org/10.1051/0004-6361/201527270

Wang, L., Lin, R. P., & Krucker, S. (2011). Pitch-angle distributions and temporal variations of 0.3-300 keV solar impulsive electron events. *The Astrophysical Journal*, *727*, 121. https://doi.org/10.1088/0004-637X/727/2/121

Wang, L., Lin, R. P., Krucker, S., & Gosling, J. T. (2006). Evidence for double injections in scatter-free solar impulsive electron events. *Geophysical Research Letters*, *330*, L03106. https://doi.org/10.1029/2005GL024434

Wang, Y., Shen, C., Liu, R., Liu, J., Guo, J., Li, X., et al. (2018). Understanding the twist distribution inside magnetic flux ropes by anatomizing an interplanetary magnetic cloud. *Journal of Geophysical Research: Sapce Physics*, *123*, 3238–3261. https://doi.org/10.1002/2017JA024971

Webb, D. F. (1988). Erupting prominences and the geometry of coronal mass ejections. *Journal of Geophysical Research*, *93*, 1749–1758. https://doi.org/10.1029/JA093iA03p01749

Webb, D. F. (1998). CMEs and prominences and their evolution over the solar cycle (Review). In D. F. Webb, B. Schmieder, & D. M. Rust, (Eds.), *IAU Colloq. 167: New Perspectives on Solar Prominences*, Astronomical Society of the Pacific Conference Series (Vol. 150, p. 463). Astronomical Society of the Pacific.

Webb, D. F., Cliver, E. W., Crooker, N. U., Cry, O. C. S., & Thompson, B. J. (2000). Relationship of halo coronal mass ejections, magnetic clouds, and magnetic storms. *Journal of Geophysical Research*, *105*, 7491–7508. https://doi.org/10.1029/1999JA000275

Webb, D. F., Cliver, E. W., Gopalswamy, N., Hudson, H. S., & Cyr, S. O. C. (1998). The solar origin of the January 1997 coronal mass ejection, magnetic cloud and geomagnetic storm. *Geophysical Research Letters*, *25*, 2469–2472. https://doi.org/10.1029/98GL00493

Whipple, E., & Lancaster, H. (1995). International coordination of solar terrestrial science. *Space Science Reviews*, *71*(1–4), 41–54. https://doi.org/10.1007/BF00751325

Wicks, R. T., Alexander, R. L., Stevens, M. L., Wilson, L. B., III, Moya, P. S., Viñas, A. F., et al. (2016). A proton-cyclotron wave storm generated by unstable proton distribution functions in the solar wind. *The Astrophysical Journal*, *819*(1), 6. https://doi.org/10.3847/0004-637X/819/1/6

Wicks, R. T., Chapman, S. C., & Dendy, R. O. (2009). Spatial correlation of solar wind fluctuations and their solar cycle dependence. *The Astrophysical Journal*, *690*, 734–742. https://doi.org/10.1088/0004-637X/690/1/734

Wicks, R. T., Horbury, T. S., Chen, C. H. K., & Schekochihin, A. A. (2011). Anisotropy of imbalanced Alfvénic turbulence in fast solar wind. *Physical Review Letters*, *106*. 045001.https://doi.org/10.1103/PhysRevLett.106.045001

Wicks, R. T., Mallet, A., Horbury, T. S., Chen, C. H. K., Schekochihin, A. A., & Mitchell, J. J. (2013). Alignment and scaling of large-scale fluctuations in the solar wind. *Physical Review Letters*, *110*(2), 025003. https://doi.org/10.1103/PhysRevLett.110.025003

Wicks, R. T., Owens, M. J., & Horbury, T. S. (2010). The variation of solar wind correlation lengths over three solar cycles. *Solar Physics*, *262*, 191–198. https://doi.org/10.1007/s11207-010-9509-4

Wicks, R. T., Roberts, D. A., Mallet, A., Schekochihin, A. A., Horbury, T. S., & Chen, C. H. K. (2013). Correlations at large scales and the onset of turbulence in the fast solar wind. *The Astrophysical Journal*, *778*(2), 177. https://doi.org/10.1088/0004-637X/778/2/177

Wild, J. P., Smerd, S. F., & Weiss, A. A. (1963). Solar bursts.*Annual Review of Astronomy and Astrophysics*, *1*, 291–366. https://doi.org/10.1146/annurev.aa.01.090163.001451

Wilson, L. B., III (2010). *The microphysics of collisionless shocks (Unpublished Doctoral dissertation)*. University of Minnesota. https://ui.adsabs.harvard.edu/abs/2010PhDT.43W/abstract

Wilson, L. B., III (2016). Low frequency waves at and upstream of collisionless shocks. In A. Keiling, D.-H. Lee, & V. Nakariakov, (Eds.), Low frequency waves at and upstream of collisionless shocks. *Low-frequency waves in space plasmas*, Geophysical Monograph Series (Vol. 216, pp. 269–291). Washington, D.C. American Geophysical Union. https://doi.org/10.1002/9781119055006.ch16

Wilson, L. B., III (2020). Wind WAVES TDSF Dataset [Dataset], *Zenodo*. https://doi.org/10.5281/zenodo.3911205

Wilson, L. B., III. (2021). Space Plasma Missions IDL Software Library. *Zenodo*. Retrieved from https://doi.org/10.5281/zenodo.4451331

Wilson, L. B., III (2021). Wind lz calibration and decommutation software. *Zenodo*. https://doi.org/10.5281/zenodo.4451304

Wilson, L. B., III, Cattell, C. A., Kellogg, P. J., Goetz, K., Kersten, K., Kasper, J. C., et al. (2009). Low-frequency whistler waves and shocklets observed at quasi-perpendicular interplanetary shocks. *Journal of Geophysical Research*, *114*, A10106. https://doi.org/10.1029/2009JA014376

Wilson, L. B., III, Cattell, C. A., Kellogg, P. J., Goetz, K., Kersten, K., Kasper, J. C., et al. (2010). Large-amplitude electrostatic waves observed at a supercritical interplanetary shock. *Journal of Geophysical Research*, *115*(A12), A12104. https://doi.org/10.1029/2010JA015332

Wilson, L. B., III, Cattell, C., Kellogg, P. J., Goetz, K., Kersten, K., Hanson, L., et al. (2007). Waves in interplanetary shocks: A Wind/WAVES study. *Physical Review Letters*, *99*, 041101. https://doi.org/10.1103/PhysRevLett.99.041101

Wilson, L. B., III, Cattell, C. A., Kellogg, P. J., Wygant, J. R., Goetz, K., Breneman, A., & Kersten, K. (2011). The properties of large amplitude whistler mode waves in the magnetosphere: Propagation and relationship with geomagnetic activity. *Geophysical Research Letters*, *38*(17), 17107. https://doi.org/10.1029/2011GL048671

Wilson, L. B., III, Chen, L.-J., Wang, S., Schwartz, S. J., Turner, D. L., Stevens, M. L., et al. (2019a). Electron energy partition across interplanetary shocks. II. Statistics. *The Astrophysical Journal - Supplement Series*, *245*(2), 24. https://doi.org/10.3847/1538-4365/ab5445

Wilson, L. B., III, Chen, L.-J., Wang, S., Schwartz, S. J., Turner, D. L., Stevens, M. L., et al. (2019b). Electron energy partition across interplanetary shocks. I. Methodology and data product. *The Astrophysical Journal - Supplement Series*, *243*(1), 8. https://doi.org/10.3847/1538-4365/ab22bd

Wilson, L. B., III, Chen, L.-J., Wang, S., Schwartz, S. J., Turner, D. L., Stevens, M. L., et al. (2019c). Supplement to: Electron energy partition across interplanetary shocks. *Zenodo*. https://doi.org/10.5281/zenodo.2875806

Wilson, L. B., III, Chen, L.-J., Wang, S., Schwartz, S. J., Turner, D. L., Stevens, M. L., et al. (2020a). Electron energy partition across interplanetary shocks. III. Analysis. *The Astrophysical Journal*, *893*(22), 21. https://doi.org/10.3847/1538-4357/ab7d39

Wilson, L. B., III, Chen, L.-J., Wang, S., Schwartz, S. J., Turner, D. L., Stevens, M. L., et al. (2020b). Supplement to: Electron energy partition across interplanetary shocks: III. Analysis. *Zenodo*. https://doi.org/10.5281/zenodo.3627284

Wilson, L. B., III, Koval, A., Sibeck, D. G., Szabo, A., Cattell, C. A., Kasper, J. C., et al. (2013). Shocklets, SLAMS, and field-aligned ion beams in the terrestrial foreshock. *Journal of Geophysical Research: Space Physics*, *118*(3), 957–966. https://doi.org/10.1029/2012JA018186

Wilson, L. B., III, Koval, A., Szabo, A., Breneman, A., Cattell, C. A., Goetz, K., et al. (2012). Observations of electromagnetic whistler precursors at supercritical interplanetary shocks. *Geophysical Research Letters*, *39*(8), L8109. https://doi.org/10.1029/2012GL051581

Wilson, L. B., III, Koval, A., Szabo, A., Breneman, A., Cattell, C. A., Goetz, K., et al. (2013). Electromagnetic waves and electron anisotropies downstream of supercritical interplanetary shocks. *Journal of Geophysical Research: Space Physics*, *118*(1), 5–16. https://doi.org/10.1029/2012JA018167

Wilson, L. B., III, Koval, A., Szabo, A., Stevens, M. L., Kasper, J. C., Cattell, C. A., & Krasnoselskikh, V. V. (2017). Revisiting the structure of low Mach number, low beta, quasi-perpendicular shocks. *Journal of Geophysical Research: Space Physics*, *122*(9), 9115–9133. https://doi.org/10.1002/2017JA024352

Wilson, L. B., III, Sibeck, D. G., Turner, D. L., Osmane, A., Caprioli, D., & Angelopoulos, V. (2016).Relativistic electrons produced by foreshock disturbances observed upstream of the Earth's bow shock. *Physical Review Letters*, *117*(21), 215101. https://doi.org/10.1103/PhysRevLett.117.215101

Wilson, L. B., III, Stevens, M. L., Kasper, J. C., Klein, K. G., Maruca, B. A., Bale, S. D., et al. (2018). The statistical properties of solar wind temperature parameters near 1 au. *The Astrophysical Journal—Supplement Series*, *236*(2), 41. https://doi.org/10.3847/1538-4365/aab71c

Wilson, R. M., & Hildner, E. (1984). Are interplanetary magnetic clouds manifestations of coronal transients at 1 AU. *Solar Physics*, *91*, 169–180. https://doi.org/10.1007/BF00213622

Winslow, R. M., Lugaz, N., Schwadron, N. A., Farrugia, C. J., Yu, W., Raines, J. M., et al. (2016). Longitudinal conjunction between MESSENGER and STEREO A: Development of ICME complexity through stream interactions. *Journal of Geophysical Research: Space Physics*, *121*, 6092–6106. https://doi.org/10.1002/2015JA022307

Winter, L. M., & Ledbetter, K. (2015). Type II and Type III radio bursts and their correlation with solar energetic proton events. *The Astrophysical Journal*, *809*, 105. https://doi.org/10.1088/0004-637X/809/1/105

Wong, H. V. (1970). Electrostatic electron-ion streaming instability. *Physics of Fluids*, *13*, 757–760. https://doi.org/10.1063/1.1692983

Wood, B. E., Wu, C.-C., Lepping, R. P., Nieves-Chinchilla, T., Howard, R. A., Linton, M. G., & Socker, D. G. (2017). A STEREO survey of magnetic cloud coronal mass ejections observed at Earth in 2008–2012. *The Astrophysical Journal—Supplement Series*, *229*, 29. https://doi.org/10.3847/1538-4365/229/2/29

Wood, S. R., Malaspina, D. M., Andersson, L., & Horanyi, M. (2015). Hypervelocity dust impacts on the Wind spacecraft: Correlations between Ulysses and Wind interstellar dust detections. *Journal of Geophysical Research: Space Physics*, *120*, 7121–7129. https://doi.org/10.1002/2015JA021463

Woodham, L. D., Wicks, R. T., Verscharen, D., & Owen, C. J. (2018). The role of proton cyclotron resonance as a dissipation mechanism in solar wind turbulence: A statistical study at ion-kinetic scales. *The Astrophysical Journal*, *856*, 49. https://doi.org/10.3847/1538-4357/aab03d

Woodham, L. D., Wicks, R. T., Verscharen, D., Owen, C. J., Maruca, B. A., & Alterman, B. L. (2019). Parallel-propagating fluctuations at proton-kinetic scales in the solar wind are dominated by kinetic instabilities. *The Astrophysical Journal Letters*, *884*(2), L53. https://doi.org/10.3847/2041-8213/ab4adc

Wrenn, G. L., Rodgers, D. J., & Ryden, K. A. (2002). A solar cycle of spacecraft anomalies due to internal charging. *Annales Geophysicae*, *20*(7), 953–956. https://doi.org/10.5194/angeo-20-953-2002

Wu, C.-C., & Lepping, R. P. (2015). Comparisons of characteristics of magnetic clouds and cloud-like structures during 1995 - 2012. *Solar Physics*, *290*, 1243–1269. https://doi.org/10.1007/s11207-015-0656-5

Wu, C. S., Winske, D., Papadopoulos, K., Zhou, Y. M., Tsai, S. T., & Guo, S. C. (1983). A kinetic cross-field streaming instability. *Physics of Fluids*, *26*, 1259–1267. https://doi.org/10.1063/1.864285

Wu, C. S., Winske, D., Tanaka, M., Papadopoulos, K., Akimoto, K., Goodrich, C. C., et al. (1984). Microinstabilities associated with a high Mach number, perpendicular bow shock. *Space Science Reviews*, *37*, 63–109. https://doi.org/10.1007/BF00213958

Wygant, J. R., Bonnell, J. W., Goetz, K., Ergun, R. E., Mozer, F. S., Bale, S. D., et al. (2013). The electric field and waves instruments on the radiation belt storm probes mission. *Space Science Reviews*, *179*(1–4), 183–220. https://doi.org/10.1007/s11214-013-0013-7

Xystouris, G., Sigala, E., & Mavromichalaki, H. (2014). A complete catalogue of high-speed solar wind streams during solar cycle 23. *Solar Physics*, *289*, 995–1012. https://doi.org/10.1007/s11207-013-0355-z

Zesta, E., & Sibeck, D. G. (2004). A detailed description of the solar wind triggers of two dayside transients: Events of 25 July 1997. *Journal of Geophysical Research*, *109*, 1201. https://doi.org/10.1029/2003JA009864

Zhang, J., Richardson, I. G., Webb, D. F., Gopalswamy, N., Huttunen, E., Kasper, J. C., et al. (2007). Solar and interplanetary sources of major geomagnetic storms (Dst ≤ -100 nT) during 1996-2005. *Journal of Geophysical Research*, *112*, A10102. https://doi.org/10.1029/2007JA012321

Zhao, X., Liu, Y. D., Hu, H., & Wang, R. (2019). Quantifying the propagation of fast coronal mass ejections from the sun to interplanetary space by combining remote sensing and multi-point in situ observations. *The Astrophysical Journal*, *882*(2), 122. https://doi.org/10.3847/1538-4357/ab379b

Zhao, X. H., Feng, X. S., Feng, H. Q., & Li, Z. (2017). Correlation between angular widths of CMEs and characteristics of their source regions. *The Astrophysical Journal*, *849*, 79. https://doi.org/10.3847/1538-4357/aa8e49

Zhdankin, V., Boldyrev, S., & Mason, J. (2012). Distribution of magnetic discontinuities in the solar wind and in magnetohydrodynamic turbulence. *The Astrophysical Journal Letters*, *760*, L22. https://doi.org/10.1088/2041-8205/760/2/L22

Zurbuchen, T. H., & Richardson, I. G. (2006). In-situ solar wind and magnetic field signatures of interplanetary coronal mass ejections. *Space Science Reviews*, *123*(1–3), 31–43. https://doi.org/10.1007/s11214-006-9010-4